Creation and Modification of Solid-State Quantum Emitters via Charged Particle Beams

by

Angus J. Gale

Under the supervision of

Professor Milos Toth

A dissertation submitted in fulfillment
of the requirements for the degree of

Doctor of Philosophy

University of Technology Sydney
School of Mathematical and Physical Sciences
New South Wales
Australia

August, 2024

CERTIFICATE OF ORIGINAL AUTHORSHIP

I, Angus J. Gale, declare that this thesis is submitted in fulfilment of the requirements for the award of Doctor of Philosophy, in the School of Mathematical and Physical Sciences at the University of Technology Sydney.

This thesis is wholly my own work unless otherwise referenced or acknowledged. In addition, I certify that all information sources and literature used are indicated in the thesis.

This document has not been submitted for qualifications at any other academic institution.

This research is supported by the Australian Government Research Training Program.

August 3, 2024

Acknowledgments

THIS THESIS WOULD BE nothing without the assistance of so many people. I would like to thank the following for all their help:

My supervisors Profs Milos Toth and Igor Aharonovich, for the opportunities and guidance you have given me during my time at UTS. Your knowledge and expertise in these fields has been invaluable and I feel fortunate to have been able to join the group under your supervision.

Johannes Fröch for your overall mentorship, showing me so much about the work we do and of course for the extreme patience required to deal with my constant questions. Similarly, to Chi, Dom, Yongliang, James, John, Mehran, Noah, Simon, Minh, Daniel, Mika, Zaiquan, Toan, Carlo, Garrett, Milad, Vanya, Lesley, Thinh, Karin, Blake and the rest of the group. I have learnt so much from you all and have truly enjoyed our time spent together. I cannot thank you all enough for all the help you have given me.

A special thanks must go to FEI (Thermo Fisher Scientific) and Delmic for the microscopes and instruments without which none of this work would be possible. Similarly the equipment is worthless without proper upkeep and training. Thanks to Mark Lockrey, Herbert Yuan, Katie McBean, Geoff McCredie and Dr Linda Xiao for the training and assistance with the instrumentation in the labs.

Finally to my family, Mum and Dad for continually pushing me in the right direction. It took a while but thank you for all the opportunities you have given me. To Matilda and Edie :) You

are always beacons of hope when things are tough and have helped me more than you could ever know. To Alex, thank you for your constant love and support. I know how difficult this has been at times and can't thank you enough for everything you have done to help me. XO

Thesis Outline

This thesis is structured in the following manner: Chapter 1 introduces many of the topics and concepts covered in the thesis. Firstly an introduction of photonic quantum technologies is presented. Next an overview is given on current charged particle technologies available, focusing on modern scanning electron microscopy (SEM) and focused ion beam (FIB) systems. Finally there is a discussion of solid state colour centres, including examples of specific colour centres and their hosts, as well as currently utilised methods to engineer these colour centres.

Chapter 2 gives an overview of the techniques used in the experimental work undertaken in the following chapters, with some background theory and information on typical setups utilised. This chapter specifically focuses on the luminescence techniques, cathodoluminescence (CL) and photoluminescence (PL) and their use in characterising solid state quantum emitters.

The remaining chapters cover the published experimental work and end with a conclusion. In Chapter 3 a novel use of a commercially available FIB system to deterministically engineer nitrogen vacancies in diamond is outlined. This chapter follows on work using recoil implantation with solid state precursors and uses gas-phase precursors to simplify the overall procedure. [1] This chapter is based on my own work and includes text and figures copied verbatim from the peer-reviewed journal article; Gale, A. et al, *Recoil implantation using gas-phase precursor molecules*, Nanoscale, 2021. [2]

The remaining chapters focus on quantum defects in hexagonal boron nitride (hBN). In Chapter 4 I have further explored a new class of colour centres in hBN denoted ”blue emitters”

in this thesis. Creation of these blue emitters had been demonstrated in earlier works but the work in this chapter clarifies some anomalies seen in the literature as well as outlines techniques to engineer these emitters with a level of determinism not seen in prior literature. This chapter is based on my own work and includes text and figures copied verbatim from the peer-reviewed journal article; Gale, A. et al, *Site-specific fabrication of blue quantum emitters in hexagonal boron nitride*, ACS Photonics, 2022.[3]

In Chapter 5 another class of colour centre in hBN is explored and manipulated. The boron vacancy (V_B) is another promising emitters with optically addressable spin. At the time of writing no work had explored the modification of charge state on these specific emitters. In order to undertake this work an existing correlated electron and optical microscopy was modified to allow for a scanning confocal microscopy setup to be integrated into the SEM and allow for manipulation of the (V_B) during in situ optical measurements. This chapter is based on my own work and includes text and figures copied verbatim from the peer-reviewed journal article; Gale, A. et al, *Manipulating the charge state of spin defects in hexagonal boron nitride*, Nano Letters, 2023.[4]

Finally, a concluding chapter will summarise the work presented in this thesis with references to the original motivations behind them. The thesis will finish with a brief overview of possible future works and directions that may be explored.

Publications

Thesis Works

1. Gale, A., Fröch, J., Kianinia, M., Bishop, J., Aharonovich, I. and Toth, M. 2021. Recoil implantation using gas-phase precursor molecules. Nanoscale, 13(20), pp.9322-9327.[2]

2. Gale, A., Li, C., Chen, Y., Watanabe, K., Taniguchi, T., Aharonovich, I. and Toth, M. 2022. Site-specific fabrication of blue quantum emitters in hexagonal boron nitride. ACS Photonics, 9(6), pp.2170-2177.[3]

3. Gale, A., Scognamiglio, D., Zhigulin, I., Whitefield, B., Kianinia, M., Aharonovich, I. and Toth, M. 2023. Manipulating the charge state of spin defects in hexagonal boron nitride. Nano Letters, 23(13), pp.6141-6147.[4]

Non-thesis and Contributed Works

4. Horder, J., White. S.J.U., Gale. A., Li, C., Watanabe, K., Taniguchi, T., Kianinia, M., Aharonovic, I. and Toth, M. 2022. Coherence properties of electron-beam-activated emitters in hexagonal boron nitride under resonant excitation. Physical Review Applied, 18(6), pp.064021[5]

5. Zhigulin, I., Horder, J., Ivady, V.,White, S.J.U., Gale, A., Li, C., Lobo, C.J., Toth, M., Aharonovich, I. and Kianinia, M., 2023. Stark effect of quantum blue emitters in hBN. Physical Review Applied, 19(4), pp.044011[6]

6. Chen, Y., Gale. A., Yamamura, K., Horder, J., Condos, A., Watanabe, K., Taniguchi, T., Toth, M. and Aharonovich, I. 2023. Annealing of blue quantum emitters in carbon-doped hexagonal boron nitride. Applied Physics Letters, 123(4).[7]

7. Zhigulin, I., Yamamura, K., Ivady, V., Gale, A., Horder, J., Lobo, C.J., Kianinia, M., Toth, M. and Aharonovich, I. 2023. Photophysics of blue quantum emitters in hexagonal boron nitride. Materials for Quantum Technology, 3(1), pp.015002[8]

8. Nonahal, M., Horder, J., Gale, A., Ding, L., Li, C., Hennessey, M., Ha, S.T., Toth, M. and Aharonovich, I. 2023. Deterministic fabrication of a coupled cavity-emitter system in hexagonal boron nitride. Nano Letters. 23(15), pp.6645-6650[9]

9. Tran, T.N., Gale, A., Whitefield, B., Dyakonov, V., Toth, M., Aharonovich, I. and Kianinia, M. 2023. Coupling spin defects in hexagonal boron nitride to a microwave cavity. Applied Physics Letters, 123(3)[10]

10. Sortino, L., Gale, A., Kühner, L., Li, C., Biechteler, J., Wendisch, F.J., Kianinia, M., Ren, H., Toth, M., Maier, S.A., Aharonovich, I. and Tittl, A. 2024. Optically addressable spin defects coupled to bound states in the continuum metasurfaces. Nature Communications, 15(1), pp.2008[11]

Conference Proceedings

1. Gale, A., Li, C., Chen, Y., Watanabe, K., Taniguchi, T., Aharonovich, I. and Toth, M. 2022, December. Controllable fabrication of blue quantum emitters in hexagonal boron nitride. Conference on Optoelectronic and Microelectronic Materials and Devices. Australian Institude of Physics.

List of Abbreviations

2D - two dimensional

AE - Auger electron

AFM - atomic force microscope

APD - avalanche photodiode

BSE - backscattered electron

CL - cathodoluminescence

CVD - chemical vapour deposition

CW - continuous wave

E(I)BID/E - electron (ion) beam induced deposition/etching

EDS/X - energy dispersive X-ray spectroscopy

FE(I)BIP - focused electron(ion) beam induced processing

FIB - focused ion beam

FLG - few layer graphene

GFIS - gas field ion source

hBN - hexagonal boron nitride

HBT - Hanbury Brown and Twiss

HIM - helium ion microscope

IR - infra-red

IRF - instrument response function

NP - non-polynomial complexity class

NIR - near infra-red

NMR - nuclear magnetic resonance

NV - nitrogen vacancy

PE - primary electron

PFIB - plasma focused ion beam

PL - photoluminescence

PSB - phonon sideband

ODMR - optically detected magnetic resonance

QD - quantum dot

QKD - quantum key distribution

SE - secondary electron

SEM - scanning electron microscope

SPE - single photon emitter

SRIM - stopping and range of ions in matter

TEM - transmission electron microscope

TMDC - transition metal dichalcogenide

UV - ultraviolet

ZPL - zero phonon line

Contents

List of Figures

List of Tables

Abstract

Solid state quantum emitters are building blocks for emerging photonic based quantum technologies. These emitters take the form of atomic scale defects that can be used as sources to generate single photons. Many materials have been identified to host quantum emitters; in particular, diamond and hexagonal boron nitride (hBN) are two promising platforms hosting a number of different defect types. There are many creation methods available but in order to realise real world applications they must be efficient, deterministic and scalable. Charged particle microscopy systems are widespread in research and industry settings and can be utilised to engineer, modify and characterise quantum emitters. This thesis outlines three procedures to create, modify and characterise solid state quantum emitters using charged particle microscopy systems.

Firstly, creation of nitrogen vacancy (NV) centres in diamond via recoil implantation of gaseous precursors is presented. The method uses a commercially available focused ion beam (FIB) system to expand and simplify documented methods utilising solid-thin films. Creation of NV centres is demonstrated with three nitrogen containing precursor gases exhibiting the robustness of the method.

The next works focus on two defects in hBN; the blue emitter and boron vacancy (VB). Using electron irradiation in a scanning electron microscope (SEM), a technique for site-specific fabrication of single defects is shown. The fabricated emitters demonstrate a single emission energy of 2.8 eV (436 nm), site selectivity and controllable defect density. The ability to fabricate emitters is linked to another existing defect type with emission at 305 nm (4.1 eV). Blue

emitter generation is attributed to the fragmentation of carbon clusters by electron impact. The robustness and universality of the emitter fabrication technique is enhanced by a pre-irradiation annealing treatment. These results provide important insights into photophysical properties and structure of defects in hBN, outlining a framework for site-specific fabrication of quantum emitters in hBN.

Finally, charge state control of the VB defect is shown using a customised SEM setup with in-situ scanning confocal photoluminescence (PL) microscopy. Charge state switching between the 0 and -1 states is demonstrated under concurrent electron and laser excitation. The switching is shown to be deterministic and reversible. Further control over the charge states is shown using a heterostructure device to adjust the rates of electrons and holes injected into the hBN, stabilising the system to the spin-active -1 charge state.

1

Introduction

1.1 Preface

The role of science in the advancement of modern society cannot be understated. Research and development of semiconductor based technologies are one of the leading drivers in this progress. Integrated circuits have enabled the miniaturisation of electronics such that a modern smartphone has many billions of transistors. However, with current systems based on classical mechanics hitting the miniaturisation limits, new methods and technologies are required.[12] One of the most radical ideas of the early 20th century was that of quantum mechanics. Now, in the 21st century, quantum mechanics is ubiquitous and research on quantum based technologies ever increasing. Such technologies were once only the realm of theory, offering glimpses of

technologies possessing exceptional speed, efficiency and sensitivity when compared to their classical counterparts. Quantum technologies have now moved beyond the world of theory and are being realised as functional systems. While currently many of the technologies are in their infancy and/or still in early development phases, the market for quantum computing alone is forecast to grow to a size of 4.4 billion USD by 2028 with the market for all quantum technologies possibly reaching a size of 50 billion by 2033.[13]

In order to realise these quantum technologies, many different platforms have been explored. These include superconducting systems, trapped ions, cold atoms and silicon based technologies. The use of isolated solid state defects and systems based on photons are another promising avenue in order to realise such technologies. The applications are broad and whether sources of single photons, or defects with optically addressable spin are utilised, this research space is vast and will require even more focus in the coming years.

1.2 Motivations

In order to realise practical and scalable photonic based quantum technologies, there is a requirement for integrated components like sources, circuits and detectors.[14] The basis of these technologies is the source itself. Solid state quantum emitters are one emerging source type, offering on-demand single photon generation and convenience and scalability compared to alternative sources. Host materials like diamond and hBN are well studied and have shown the ability to be integrated into devices for use in such applications.

While quantum emitters possess many positive attributes, deterministic creation is still a great hurdle that must be overcome if such devices are to become a reality. With these solid state systems in their relative infancy, much work is still undergoing on efficient creation and characterisation methods. Charged particle microscopy is a field that is particularly well suited to the creation and modification of these colour centres. With modern dual-beam instruments capable of focusing electron and ion beams with nanometre resolutions and a plethora of characterisation techniques available, they can be used to engineer, characterise and modify solid state emitters. Dual-beam instruments are also widespread across both universities and industry

settings, and the combination of tools in a single unit allows for a highly versatile instrument.

In order to achieve such lofty ideals promised by quantum technologies, the methods and mechanisms behind the creation and modification of solid state SPEs must first be studied and understood so that they may be integrated into next generation devices. Charged particle microscopy is highly suited to this task and it is at this point that the motivations behind the work undertaken in this thesis are clear. Utilising charged particle microscopy systems to create, modify and characterise solid state quantum emitters.

1.3 Photonic Quantum Technologies

Novel technologies based on the fundamentals of quantum mechanics are a highly researched topic, with many different platforms are being developed at the present time. This section focuses on one particular platform utilising photons to realise computing, sensing and encrypted communication.

Photons are the quanta of the electromagnetic field and are well suited to carry information due to their weak environmental coupling and lack of decoherence that have proved challenging for other types of solid-state quantum systems.[15] It is especially fitting that the history of quantum mechanics was sparked around the idea of quantised light particles, with work by Max Plank describing the theory of black body radiation[16] and Albert Einstein's revolutionary work in 1905 on the photoelectric effect.[17] A translated excerpt from Einstein's work succinctly summarises the idea of the photon.

> *According to the assumption to be contemplated here, when a light ray is spreading from a point, the energy is not distributed continuously over ever-increasing spaces, but consists of a finite number of "energy quanta" that are localized in points in space, move without dividing, and can be absorbed or generated only as a whole.*

A photon is a massless particle without charge and moves at the speed of light c in vacuum. The energy E of a photon is one of the fundamental attributes that can dictate the use cases.

It can be described by the frequency, v or wavelength, λ as seen in Equation 1.1 where h is Planck's constant.

$$E = hv = \frac{hc}{\lambda} \tag{1.1}$$

Two underlying principles that are key to enabling quantum technologies are superposition and entanglement. For any quantum system a particle can be encoded with information and for photonic quantum technologies this entails encoding information onto a photon. Classical technologies such as computing, use a classical bit which is binary and can be fully represented as one or another state (usually designated as 0 or 1). For quantum technologies, a single bit of information is referred to as a quantum bit, or qubit and utilises the principle of superposition. For photons, information can be encoded by controlling polarisation, spatial and temporal modes among others.[14] The state of a qubit $|\psi\rangle$ however, can be represented as a superposition of the two states $|0\rangle$ and $|1\rangle$ as seen in Equation 1.2.

$$|\psi\rangle = \alpha|0\rangle + \beta|1\rangle \tag{1.2}$$

The coefficients α and β give the probability amplitudes of each state. They are complex numbers constrained by the fact that the state of the qubit $|\psi\rangle$ must be normalised as seen in Equation 1.3.

$$|\alpha|^2 + |\beta|^2 = 1 \tag{1.3}$$

The states of a classical bit and qubit can be visualised as seen in Figure 1.1. The qubit can be represented on the Bloch sphere with the poles corresponding to the classical 0 and 1 states. The rest of the sphere's surface can describe any combination of states possible, fully describing the qubit $|\psi\rangle$.

In terms of photonic quantum technologies, the basis states of $|0\rangle$ and $|1\rangle$ can be represented by the horizontal $|H\rangle$ and vertical $|V\rangle$ polarisation of a photon. Linear combinations of these polarisations lead to the well defined polarisation states of diagonal $|D\rangle$, antidiagonal $|A\rangle$, left circular $|L\rangle$ and right circular $|R\rangle$. In optics this is commonly known as the Poincaré sphere.

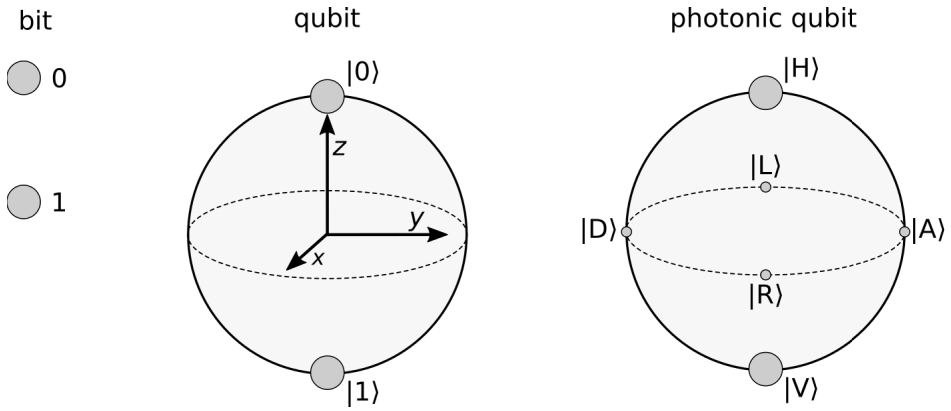

Figure 1.1: *Representations of a classical bit with only 0 and 1 states, a quantum bit (qbit) with all possible states represented by the surface of the Bloch sphere. An example of a photonic qubit is also shown on the Poincaré sphere in terms of linear combinations of the horizontal $|H\rangle$ and vertical $|V\rangle$ polarisation states. The positions of some well defined combinations of polarisation states, diagonal $|D\rangle$, antidiagonal $|A\rangle$, left circular $|L\rangle$ and right circular $|R\rangle$ are also labelled.*

At the present time, the most advanced quantum technology is quantum cryptography and more specifically, quantum key distribution (QKD). This technology uses single photon states to communicate and is fundamentally secure.[18,19] There are a currently number of QKD protocols that can be used to achieve secure communication between two parties.[20] The original protocol known as BB84, uses photons with 4 polarisation basis states as presented in Figure 1.1.[21] These photons are then used to generate and share a key that can be used for encryption. In this protocol, security is achieved due to the Heisenberg Uncertainty principle, where the quantum state of the system cannot be measured without altering the initial state.[22] If there is any attempt by an additional party to interfere or eavesdrop, this can be detected by a change in the error rate. Some protocols utilise quantum entanglement properties whereby a pair of entangled photons can be generated and distributed to two parties.[23] Due to their entanglement any polarisation component is correlated between each photon, which gives certainty that the

measured polarisation component is identical for both parties. For all QKD protocols, photons are especially suitable as they only have a weak environmental interaction, with experimental demonstrations now spanning hundreds of kilometres.[24]

Of all the present technologies currently discussed and researched, quantum computing is at the forefront, promising huge technological leaps in terms of computing power and efficiencies. Quantum computing was originally proposed by Richard Feynman in 1982 and then outlined in by David Deutsch in the theoretical paper introducing a "Universal Quantum Computer".[25] These ideas were groundbreaking and aimed to solve non-polynomial complexity class (NP) computational problems that are difficult with classical computing. While quantum computing has extremely lofty goals, the realisation of quantum computers that can outperform their classical counterparts are still many years away.[26] Regarding photonic based quantum computers, there have only been early demonstrations but the concepts behind computing with photons are viable.[14,15]

For solid state photonic systems, another promising avenue concerns the use of spin based defects like the nitrogen vacancy (NV) centre in diamond. These qubits are based on the electronic spin state of the defect, with photons used for control and readout.[27,28] Spin active defects have also been used for quantum sensing purposes. Their electronic spin states are highly sensitive to changes in the surrounding environment and as such these defects can also be used as nanoscale sensors.[29,30] In all cases, to achieve efficient photonic based computers, a number of components must be optimised including detectors, photon sources, manipulation tools and integrated photonic waveguides.[31]

1.4 Charged Particle Microscopy

1.4.1 Overview

Technologies involving charged particle beams and more specifically charged particle microscopy have enabled scientists to uncover the remarkable world of the nanoscale. Both electron and ion microscopes are incredibly versatile tools used for a wide range of applications

in research and industry settings. Primarily used as tools for high resolution imaging and nanoscale milling, the scanning electron microscope (SEM) and focused ion beam (FIB) systems also allows for a host of characterisation and material modification opportunities. Generally SEM and FIB instruments are combined in a dual-beam unit, however Helium Ion Microscope (HIM) systems are offered as standalone FIB only systems. Many other charged particle beam systems exist, including transmission electron microscopes (TEM) or ion implanters but these have many differences to the typical dual-beam units discussed in this thesis. Typically they use either much higher energies, broad beams or a combination of both. As they can be used for defect generation, there is some mention of their use in this thesis, focusing on creation and modification of solid state quantum emitters. However, all experimental work was undertaken using SEM and FIB instruments with focused beams and energies $\leq$ 30 keV and as such the majority of this thesis concerns the use of these particular systems.

As in their namesake, the underlying operation of these microscopes utilises the charged nature of these particles themselves. An electric field can be used to accelerate the particles towards a sample and magnetic or electric fields can then be used to converge the accelerated particles into a focused beam which can be positioned and scanned across a sample. The Lorentz force seen in Equation 1.4 describes the force $\vec{F}$ on a particle with charge q moving with velocity v in an electromagnetic field with electrical force component $\vec{E}$ and magnetic force component $\vec{B}$.

$$\vec{F} = q(\vec{E} + v \times \vec{B}) \tag{1.4}$$

Through years of development from the first electron microscopes developed in the 1920s and 30s to modern instruments capable of sub nanometre imaging today the underlying mechanism relies on the forces seen in Equation 1.4.[32] From the acceleration of the charged particles, convergence into a beam, positioning, scanning, detection and imaging, the underlying operation of these systems can be described by these forces. Of course the behaviour of electrons and ions in the solid are still governed by the forces described by Equation 1.4. The following sections will outline both SEMs and FIB systems. Both in the operating mechanisms behind their use as

well as the electron/ion interactions with matter.

1.4.2 Scanning Electron Microscopy

Scanning electron microscopes have been fundamental tools for material imaging and characterisation since their inception. From high resolution imaging, material characterisation to nanofabrication, SEMs are highly versatile and useful tools for a range of industry and research applications. As in the namesake, a focused beam of accelerated electrons, usually up to 30 keV, scans the sample as defined by the user for imaging, lithography or characterisation purposes. A brief overview of the operation and some electron - matter interactions will be discussed.

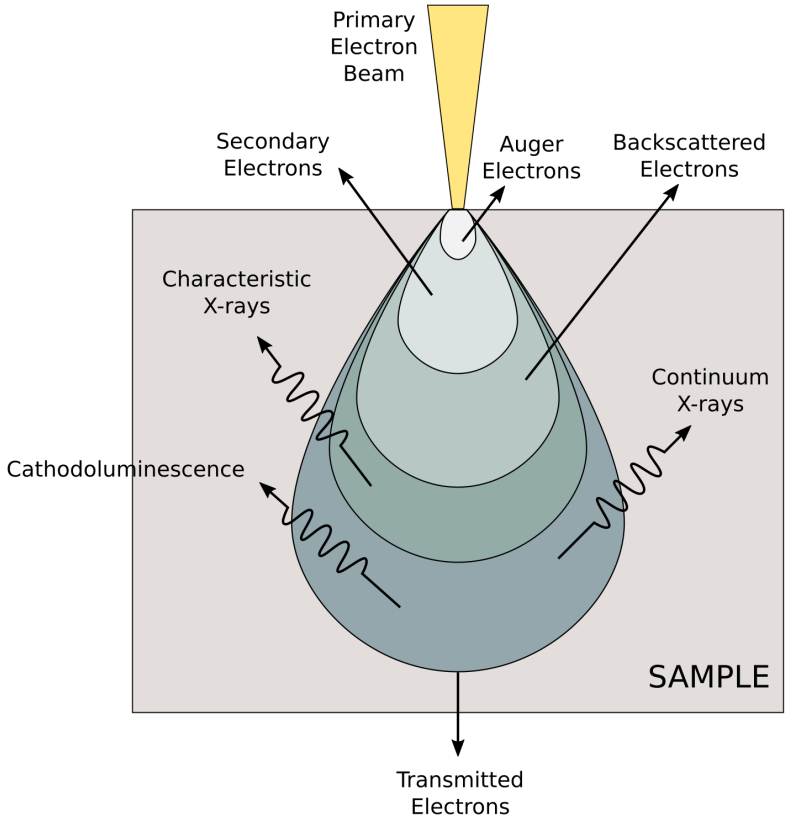

Figure 1.2: *A schematic of the interactions between primary electrons and solid sample outlining the different scattering and radiation processes. The filled teardrop regions are simplified and indicate relative volume (2D section) of the different emission types. Resultant electrons are displayed with solid arrows and electromagnetic radiation is displayed using waved arrows.*

At the sample, the primary electrons (PE) from the SEM column interact in a number of ways, through elastic and inelastic collisions with the sample matter. A schematic of these mechanisms and resultant emission types can be seen in Figure 1.2. These scattering events result in the creation of Auger electrons (AE), secondary electrons (SE) and back-scattered electrons (BSE). The resultant depth of the PEs in a sample depend primarily on the energy of the incoming electrons and the sample material. A semi-empirical equation was developed by Kanaya and Okayama to calculate the range of an electron impinging on a sample which agreed well with experiments using electrons in energies typically used in SEM and TEM instruments.[33] However the scattering induces lateral deflections to the PE and as such results in a teardrop volume of possible electron locations as is apparent in Figure 1.2. If the range of PEs exceeds the sample thickness, electrons can be transmitted and detected from both sides of a sample, leading to an increase in apparent brightness.[34] It is important to always consider the interaction volume when undertaking any experiments, as although a focused beam can be on the order of a few nanometres or less, the total volume can have a significant effect on resolution and the information collected.

Image formation in a general case, is due to AEs, SEs and BSEs escaping the sample and being detected by a biased detector in the chamber or column. As the focused beam is rastered across the sample, a monochrome image can be composed, based on the intensity or number of electrons detected at each position.[35] For ultra-thin samples transmitted electrons can be utilised via detectors below the sample. A recent technique referred to as 4D STEM-in-SEM (four-dimensional scanning transmission electron microscopy in the scanning electron microscope) records diffraction patterns of scattered electrons as the beam is scanned across the sample, allowing for measurements such as lattice orientation in graphene.[36] Electromagnetic radiation of different energies are also emitted and utilised for imaging and characterisation purposes. X-rays can be generated via several mechanisms and are typically referred to as characteristic, continuum (bremsstrahlung) and fluorescent X-rays (Fig. 1.2). Of these, characteristic X-rays are the most widely utilised, containing elemental information that can be used for the purpose of energy dispersive X-ray spectroscopy (EDS/X).[37,38] Radiation

at wavelengths in the UV to IR can also be emitted in the form of cathodoluminescence (CL), fluorescence generated by electrons exciting transitions in semiconductors and insulator materials. As CL is used significantly in Chapters 4 and 5, more detail on specific mechanisms and experimental setups is covered in Chapter 2.

Now to focus in more detail on these electron matter interactions, firstly with elastic collisions. Elastic scattering is mainly due to electrostatic interaction between electrons and nuclei of sample atoms. As PEs diffuse through a material, elastic sattering events result in a trajectory change and lead to the characteristic teardrop shaped interaction volume. BSEs are PEs scattered beyond 90° that have had sufficient energy to escape the sample. With accelerating voltages used in typical SEMs ($\leq$ 30 keV), any energy transfer can be neglected. A 30 keV electron when elastically scattered 180° by a copper nucleus is only $\sim$ 1 eV.[37] In order to induce knock-on effects seen in TEMs where an electron can displace an atom from the material lattice energies >80 keV are required, far above those found in SEMs.[39,40]

Electron-electron interactions are generally behind inelastic scattering mechanisms and are the basis for a many of the important phenomena seen in SEMs. The energies utilised are sufficient to induce ionisation events in the sample. Ionised electrons from such scattering can be from outer shell electrons, resulting in SE generation, as well as inner shell electron ejection. Inner shell ionisation energies are significantly higher than SE and range from 0.1 - 80 keV. Inelastic scattering can also induce plasmons of 5-50 eV in which collective oscillations of a sample's electron cloud can be excited.[37]

While SEMs are generally known to be non destructive, these interactions can result in a number of phenomena that can in some cases, radically modify materials. Sample charging, heating and radiolysis must all be considered as possible damage mechanisms in SEMs. Charging arises from both elastic and inelastic scattering processes and can result in very large electric fields in insulating materials.[41] These fields can be sufficient to induce electromigration or diffusion of ions in the bulk.[42] Phonon generation can also be a significant issue in thin insulating samples such as polymers and organics. Most processes mentioned so far can lead to phonon generation and sample heating.[43] Radiolysis can also occur in some organic and

inorganic samples. Ionisation events can lead to broken bonds and altered electronic states under electron irradiation, leading to amorphisation of the material.[44]

1.4.3 Focused Ion Beam Microscopy

FIB instruments are analogous to SEMs, where instead of focused electrons, a beam of focused ions is employed. As with SEMs, a FIB can also be used for imaging, however they are primarily utilised for their nanofabrication capabilities.[45,35,46,47] These instruments allow for high resolution maskless milling with nanoscale resolution. Due to the destructive nature of the ion beam microscopes an SEM is often used alongside the FIB in a dual-beam configuration, allowing for non-destructive imaging and sample positioning.

Ion generation occurs via a number of methods, with several sources used in modern dual-beam FIB instruments. The two most commonly utilised are the liquid metal ion source (LMIS) and plasma source (denoted as PFIB instruments). For completeness, another instrument known as the helium ion microscope (HIM) uses a type of source sharing some similarities with the LMIS, differing in the use of a gas field ion source (GFIS) with helium or neon ions.[48]

As with electrons, there are multiple ion-material interactions possible. These can be grouped into elastic and inelastic collisions, but given that primary ions have both an electron cloud and nucleus there are several possible interactions. Electronic energy loss processes can be considered but in the ion energy ranges used in dual-beam instruments ($\leq$30 keV), the dominant energy loss mechanism is an elastic collision between the nuclei of the primary ion and sample.[49] It is this process that results in sputtered atoms and gives the FIB the maskless nanofabrication ability.

A schematic of the possible ion-solid interactions can be seen in Figure 1.3. As a primary ion enters a sample, it can generate a number of secondary particles including secondary electrons. In fact, an ion incident on a material will result in a significantly higher secondary electron yield than an equivalent electron.[35] Elastic collisions will result in a collision cascade below the sample and result in a number of displaced atoms and/or vacancy generation.[50] If a collision

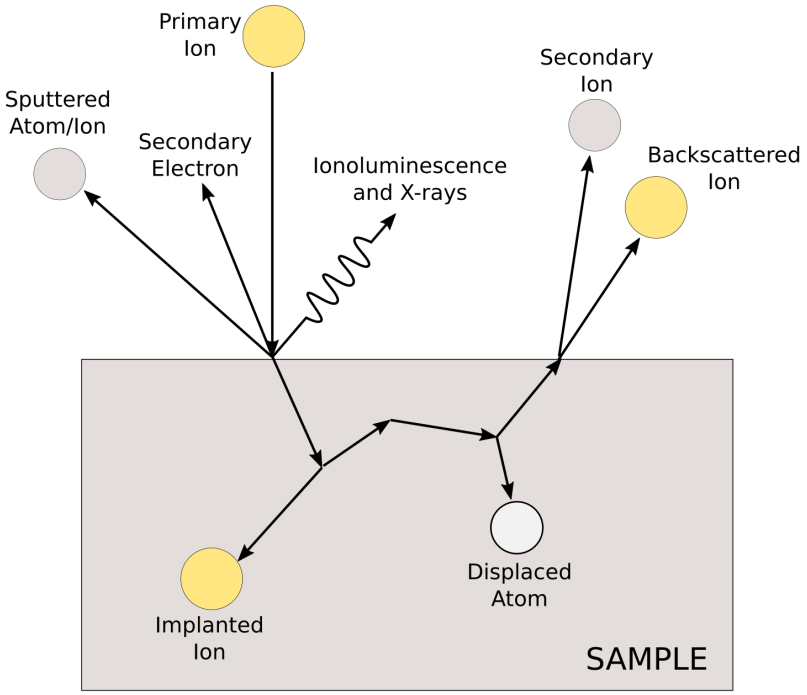

Figure 1.3: *A schematic of the interactions between primary ions and solid sample outlining the different scattering emitted particle processes. The arrows indicate the trajectory of the particles with electromagnetic radiation displayed using waved arrows.*

occurs near enough to the surface this can result in a sputtered atom. Once a primary ion has lost sufficient energy it will result in implantation. The range of ions is much lower than electrons and differs based on the mass of the ion. Ga and Xe ions will only penetrate to around 30 nm at 30 keV in Si, compared to the several micron depth range of a 30 keV electron.[51,37] Similar to electron irradiation, electronic transitions can also be excited leading to the emission of photons (ionoluminescence) and characteristic X-rays.[47]

As FIB instruments are inherently destructive it is of no surprise that materials can be drastically modified, or even completely sputtered. Sputter yields are highly dependent on the ion species and incident material, but for heavy ions like Xe incident on Si, measured sputter rates of around 0.37 $\mu m^3/nC$ can result in rapid material losses even at modest fluences.[52]

Collision cascades can quickly result in amorphised layers even before significant sputtering occurs. For some applications, materials doping is the primary objective but where implantation is not the primary aim of FIB irradiations, this can similarly effect material quality. A typical example is seen with Ga staining when preparing lamella samples for TEM investigations.[53,54] FIB irradiations can also induce phase changes in some materials including steel, with even low fluences causing significant material changes.[55,56] Finally, many of the same damage processes that can occur under electron irradiation can also be considered. The generation of secondary electrons as a consequence of the collision cascade can induce ionisation events resulting in similar damage mechanisms seen under electron irradiation.[57]

1.4.4 Focused Electron/Ion Beam Induced Processing

Given the content of the experimental chapters some more detail will be given on a particular processing technique seen in charged particle microscopy, at times overlooked in literature. The previous sections mostly focused on sub-surface process but this section outlines mechanisms seen at material interfaces. Focused electron/ion beam processing uses the kinetic energy of accelerated electrons and ions, to drive chemical reactions, which result in deposited or etched material. Although not always apparent, most users of SEM and FIB systems will have had inadvertent exposure to these techniques in the form of carbon deposition, often seen from regions of dark contrast surrounding imaged regions at higher magnification. FIB systems also regularly use metal deposits during lamella preparation in order to preserve the quality of the sample.[49]

As has already been discussed, charged particle microscopy can be utilised for nanofabrication purposes. For FIB systems this can be quite trivial due to the sputtering ability, however in an SEM, electron energies are generally below the knock on thresholds required to sputter atoms.[39,40] Another mechanism exists described under the moniker focused electron(ion) beam induced processing (FE(I)BIP). In each case interactions between the charged particles can drive reactions between adsorbates on the surface and the underlying material.

One commonly occurring issue in these systems can be ascribed to residual hydrocarbons

from lubricants, out-gassing components and unclean materials.[58] These residual hydrocarbons can act as a precursor which leads to deposition of amorphous carbon based materials. The deposited materials are seen as dark regions in SEM images and can also be lead to bright regions in photoluminescence (PL) measurements.[59] Measures can be taken to minimise unwanted deposition, including both chamber cleaning via plasma or gas purging methods and suitable sample cleaning methods.

The mechanism behind this phenomenon will be described below. Residual gas species can adsorb to the surface of a material via physisorption. Incoming electrons can then induce dissociation of these precursors through electron-electron interactions with the molecules. The different dissociation mechanisms are listed below in Equations 1.5 - 1.8.[46]

$$e^- + AB \rightarrow A^* + B^- \qquad \text{(Dissociative electron attachment)} \tag{1.5}$$

$$e^- + AB \rightarrow A^* + B^* + e^- \qquad \text{(Neutral dissociation)} \tag{1.6}$$

$$e^- + AB \rightarrow A^* + B^+ + 2e^- \qquad \text{(Dissociative ionisation)} \tag{1.7}$$

$$e^- + AB \rightarrow A^- + B^+ + e^- \qquad \text{(Bipolar dissociation)} \tag{1.8}$$

The dissociation of the hydrocarbon molecules leads to the formation of volatile species which can readily desorb, leaving any remaining material to react and crosslink, resulting in carbon based deposits on the surface of the material.[60] While it may be intuitive to assume that these dissociation mechanisms are driven by the higher energy PEs in the beam, it is generally accepted that the lower energy SEs are the driving force behind these FEBIP mechanisms, with electrons of $\sim$100 eV having the highest probability to induced the molecular dissociation.[61] At a fixed beam current, rates of FEBIP accordingly increase as the beam energies decrease, due to the increased ratio of SEs leaving the sample to the total number of PEs.[62]

These processes are not limited to deposition of carbon based materials and depending on the precursor a number of materials can be deposited. More specifically this process is known as Electron (Ion) Beam Induced Deposition (E(I)BID). Most often organometallic precursors are utilised with a metal centre surrounded by carbonaceous ligands. Common metal deposition precursors include relatively simple structures with a CO_6 ligand and a metal centre eg. Cr, Fe, MO and W or more complex molecules including $MeCpPt(Me)_3$ with cyclopentadiene ligands to deposit platinum.[59,63,46]

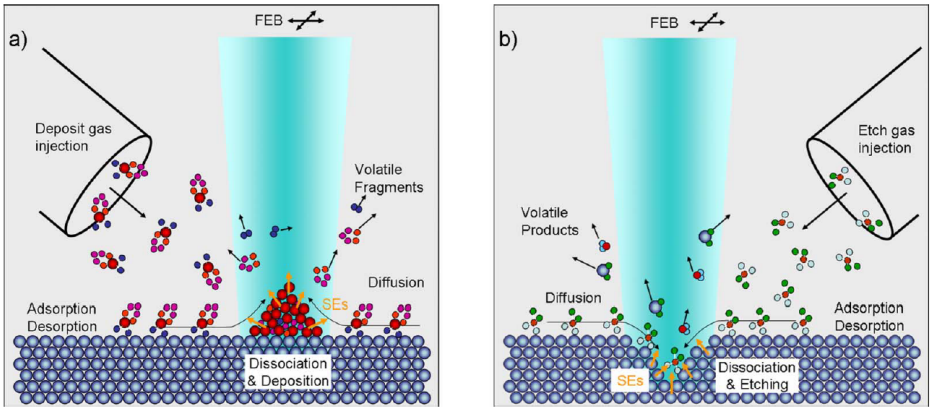

Figure 1.4: *Schematic of electron beam induced deposition and etching processes with a focused electron beam. a) Electron beam induced deposition using a gas injection capillary to inject an organometallic precursor with metal centres denoted as large red balls. b) Electron beam induced etching using a gas injection capillary to inject an etch precursor. Figures sourced from ([59]).*

An analogous procedure involves the use of alternative precursors intended to etch away materials. This process is referred to as Electron (Ion) Beam Induced Etching (E(I)BIE). EBIE can occur via a similar mechanism to that of etching, with electrons driving the dissociative mechanisms from Equations 1.5 - 1.8. Unlike deposition, the precursors are chosen such that they can form volatile compounds with the material to be etched, resulting in the new molecule being desorbed.[64] Typical precursors include water, a common etchant for carbonaceous material including graphene[65] and diamond[66] as well as XeF_2 which is suitable for etching Si_3N_4 and SiO_2.[67] Figure 1.4 shows a stylised view of the EBID 1.4(a) and EBIE 1.4(b) processes.

1.5 Solid State Quantum Emitters

This section will give an overview of solid state quantum emitters, often termed single photon emitters (SPE) or even colour centres. Some background is given as well as some more detail on specific solid state defects in both diamond and hBN. A final section will consider the methods utilised to create solid state quantum emitters and focus on the use of charged particle microscopy for this purpose.

If real world photonic quantum technologies are to be realised a suitable source is required. The generation and emission from an ideal source must fulfill some or all of the following requirements: Generation of single photons must be controlled or deterministic (often described as ”on demand” generation), the source must emit a single photon 100% of the time, the individual photons must be indistinguishable and the emission rate must be sufficiently fast.[68]

A number of single photon sources exist including trapped atoms[69,70], trapped ions[71,72], quantum dots (QD)[73,74], attenuated lasers[75,76], spontaneous parametric down conversion (SPDC)[77] and solid state defects.[27,78] A defect, including vacancies and intrinsic defects or extrinsic dopants in a material can be treated as an isolated atom or molecule. The host materials are generally wide band-gap semiconductors with the defect acting as a two-level system within the band-gap.

Current examples of solid state SPEs include the NV centre and group IV defects in diamond[79], intrinsic defects in silicon carbide (SiC)[80], carbon based defects in hBN[81], doped yttrium aluminium garnet (YAG)[82], vacancies in transition metal dichalcogenides (TMDC)[83] and defects in zinc oxide(ZnO).[84] Schematics of a number of these defects can be seen in Figure 1.5. QDs can be considered as solid state SPEs, however, they are not based on atomic defects, as with those pictured in 1.5. It is worth noting that the performance of QDs is high, with excellent photon purity[85] and important experimental demonstrations such as two photon interference demonstrated with QD based systems.[86]

Solid state SPEs may be favourable over other single photon sources for a number of reasons.

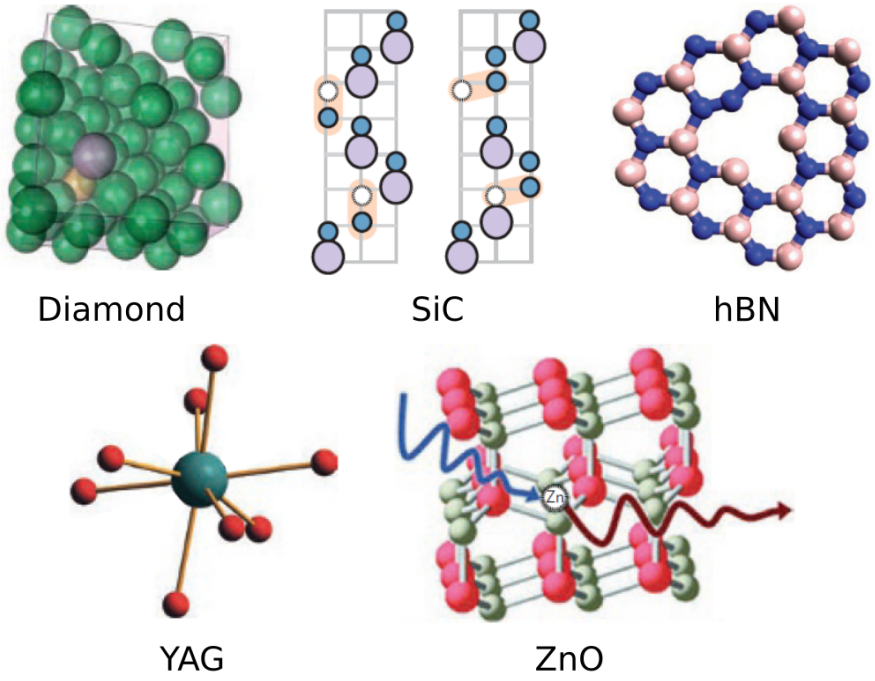

Figure 1.5: *Various light emitting defects in solid state systems, including extrinsic dopants, intrinsic defects and vacancies in bulk materials diamond, silicon carbide (SiC), yttrium aluminium garnet (YAG) and zinc oxide (ZnO). Layered 2D materials such as hexagonal boron nitride (hBN) pictured can also host light emitting defects. Figures sourced from ([78]).*

Unlike with trapped atom or ion sources, basic setups can be utilised, moving away from the bulky and often complicated apparatus required for these schemes. While efforts have been made to reduce the scale of these traps[87], solid state SPEs offer the potential for chip-scale sources which can be readily integrated into device structures.[88] Solid state SPEs also offer deterministic single photon generation unlike SPDCs and are also typically bright with count rates exceeding 1 x 10^6 counts/s.[89,90]

Of course solid state SPEs have certain limitations. Solid state materials are limited by many issues that can directly effect the generated photons. Homogeneous broadening due to the emission of phonons with short lifetimes, as well as inhomogenous broadening mechanisms due to non-uniformity of the host material, can be issues that reduce indistinguishability of photons.[91,78] High refractive index material hosts can also hinder the extraction of photons,

requiring additional means such as solid immersion lenses to enhance collection efficiencies.[92] Photobleaching is another issue faced for some solid state quantum emitters where high pump laser powers can lead to instability of an SPE.[93]

1.5.1 Diamond NV Centre

Diamond is an allotrope of carbon with tetrahedral sp^3 hybridised bonds. It is an insulating material with a bandgap of 5.5 eV.[94] It is also a host to a large number of colour centres with emissions from the UV to NIR.[95] The diamond NV centre is one of the most well studied and understood quantum emitters. The defect consists of a substitutional nitrogen atom at a carbon site alongside a vacancy marked (V) in Figure 1.6(a). Notably, NV centres were one of the earliest solid state defects to show true single photon emission.[96] The defect is also unique in that it possesses optically addressable electronic spin with long spin coherence times nearing second timescales.[97] These properties have enabled the demonstration of many groundbreaking experiments for solid state defects, including two photon interference[98,99], quantum memory demonstrations[100] and single defect nuclear magnetic resonance (NMR).[101,102]

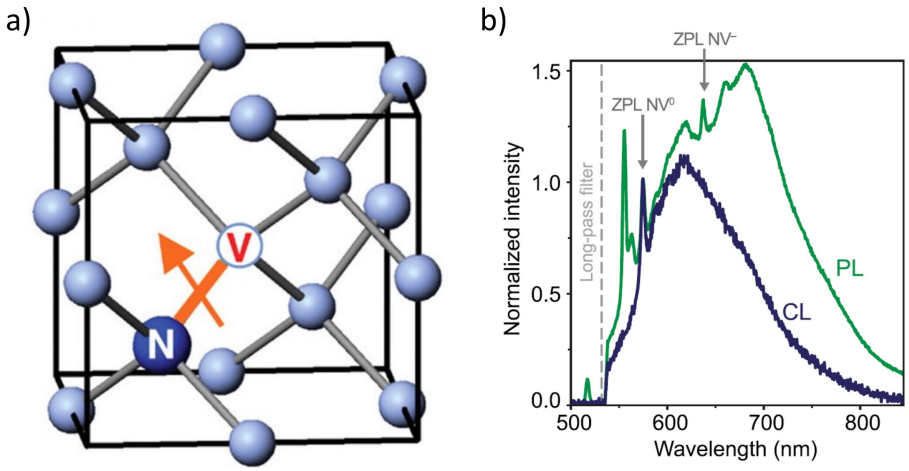

Figure 1.6: *The NV centre in diamond. a) A ball and stick model of the NV centre in diamond lattice. b) PL and CL spectra of the NV defect showing the emission from negative and neutral charge states. Figure (a) sourced from ([103]), Reprinted with permission from AAAS, and b) from ([104]).*

The defect has two charge configurations, the neutral (NV^0) and negative (NV^-) charge states respectively. Each state has a unique zero phonon line (ZPL) as seen in Figure 1.6(b). Given the favourable NV^- charge state there has been a significant proportion of work aimed at controlling the charge state of the centres so that the electronic spin remains addressable.[105,106]

The NV centres can be found natively, however many methods exist to create them with control and efficiency, including the use of ion implantation[107,108], FIB[109], SEM[110], TEM[111,112] and MeV electron irradiation.[113] While there are many favourable aspects of the NV centre it is not without some drawbacks. Single NV centres have a broad PSB and relatively dim ZPL emission only consisting of 3% of the total emission.[114]

1.5.2 Single Emitters in hBN

hBN is a layered van-der Waals material. Within each sheet boron and nitrogen atoms are arranged in a planar hexagonal lattice. Each sheet is weakly bonded by van der Waals forces which allow for bulk crystals to be exfoliated down to the monolayer level. The material has a wide band gap of ~ 6 eV.[115,116,117] As with other two-dimensional materials like graphene[118,119] and transition metal dichalcogenides (TMDC)[120,121], hBN is favourable in that it can be readily exfoliated down to the monolayer level.[122] The weakly bonded layers also allow for integration into heterostructure devices via accessible transfer and stacking methods.[123,124]

Like diamond, hBN can host colour centres which are discussed in more detail below. These emitters span the spectral range from ultraviolet (UV) to the near infrared (NIR), are bright, can be isolated as single defects and have optically addressable spin.[78,125] While these emitters have many favourable properties, at this stage no single emitter type can fulfill all of the requirements for an ideal single photon emitter source.[68] As a significant portion of the experimental work in the this thesis is focused on these colour centres, each emitter type or class will be discussed in their own section.

Emitter Class	Controllable Creation Methods	Single Defects	ZPL Position	Spin Control	Notes
4.1 eV Defect	No*	Yes◇	305 nm	No	Generally seen in lower crystal quality hBN or regions of higher carbon concentration.
Blue Emitter	Yes	Yes	436 nm	No	Electron irradiation is requisite to activate emitters.
Visible Emitters	No*	Yes	450-750 nm	Yes†	The ZPL position ranges from the blue to NIR for this class of emitter.
Boron Vacancy	Yes	No	800 nm	Yes	Fully elucidated atomic structure. Dim emission intensity.

Table 1.1: *Overview of the different emitter classes seen in hBN. * Some level of control over the creation of these emitter types is possible, however there is a lack of spatial and or spectral control in most cases. ◇ Single defects have only been seen under CL excitation in a TEM. As of yet a single defect has not been measured using optical excitation schemes. † Some visible defects have shown optically addressable spin, however these are limited to select few defects.*

Visible Emitters

In 2016 single defects were discovered in hBN emitting with ZPL wavelengths of 550-750 nm.[89,126] Since this discovery, a majority of the literature in the field has been devoted to the study of this class of "visible" emitters as they have shown many favourable properties including high brightness, stability[127,128], narrow linewidth[129] and more recently optically addressable spin.[130,125]

A notable feature of this class of emitters is the inconsistent emission wavelengths and spectral features, including different coupling strength to the phonon modes of the hBN.[131] An example of the emission from a single emitter can be seen in Figure 1.7(a). Although many defect configurations have been proposed, there is no confirmation of the true defect structure for this

class of defects. A strong link to carbon as a requirement for these defects has been demonstrated but as of yet no clear structure has been shown.[81]

Controllable engineering of these emitters has also been lacking and while many possible methods have been demonstrated, there is as of yet only one consistent method that has achieved both emitter localisation and consistent emission wavelength. Recent works from Kumar et al. have demonstrated the use of localised SEM irradiation to engineer a particular class of emitters with a consistent spectral peak at 575 nm.[132,133,134] Other typical engineering methods include incorporation of dopants during growth[135,81], high temperature annealing[126,136], growth on pillars[47], plasma treatments[137], MeV electrons[138], Ion irradiation[139,140], strain[128] and AFM nanoindentation.[141]

Boron Vacancy

In recent years another defect in hBN has had a significant proportion of research effort dedicated to it, due to its optically addressable spin properties. The so called boron vacancy (V_B) emits in the near-infrared (NIR) with a broad emission centred around 800 nm.[142,143] At present it is notable that it is the only emitter in hBN with a fully elucidated atomic structure, as well as deterministic creation methods, including neutron Irradiation[142], ion irradiation[143,144], femtosecond laser ablation[145] and electron irradiation.[146]

The negative charge state ($V_B{}^-$) has a level structure analogous to the NV^- centre in diamond. It has a ground state triplet configuration, with a zero field splitting of 3.47 GHz (Figure 1.7(c,d)).[125] Utilising enhancement from a gold film optically detected magnetic resonance (ODMR) contrasts of 46% have been experimentally observed.[144] However the emission of the $V_B{}^-$ defect is relatively weak. Attempts to increase the emission intensity via plasmonic nanogap cavities have resulted in modest emission enhancement and reduction in lifetime.[147]

While this emitter has favourable spin and the creation is deterministic, the broad, dim emission means that at this stage there has yet been no sign of single emission from these defects. The ZPL position is also not clear from the broad spectra, however methods using cavity enhanced emission has speculated that the ZPL emits at 773 nm.[148] At the present

time a significant body of the current literature is exploring sensing applications for these emitters.[149,150,151] Unlike the NV centre in diamond, there has been no observation of CL with the typical NIR spectra absent under electron excitation. The experimental work in chapter 5 explores the behaviour of the V_B under simultaneous photo and electron excitation.

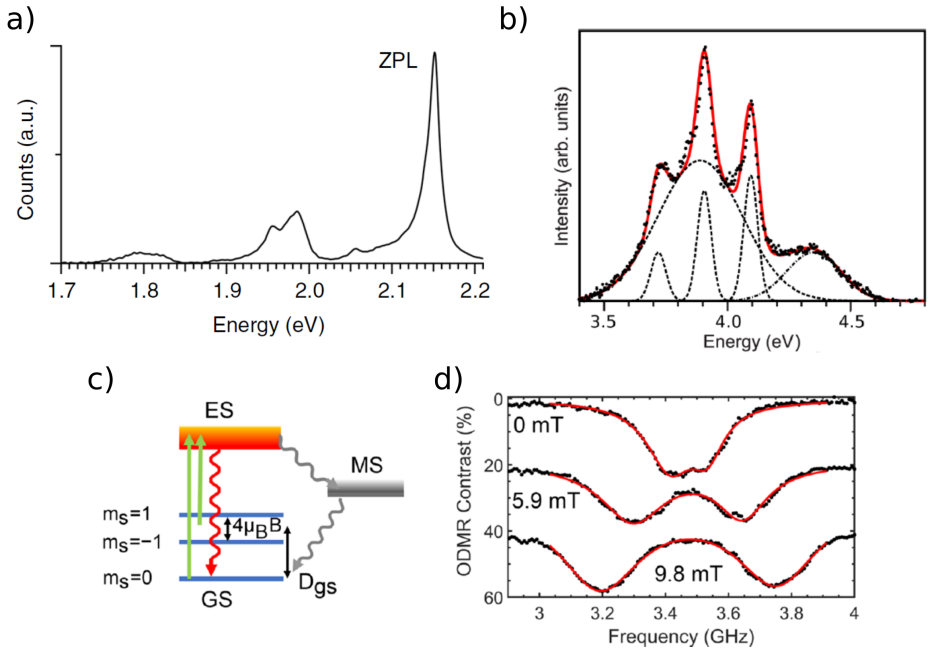

Figure 1.7: *Overview of quantum emitters in hBN. a) PL spectra of a typical visible class of emitter with ZPL position labelled b) CL spectra of the 4.1 eV emitter with deconvolved curve fits. c) Energy level structure of the V_B^- defect in hBN d) Three ODMR spectra from an ensemble of V_B^- defects showing the effect of magnetic field on the resonance of m_s=+1 and m_s-1 states. Figure (a) sourced from ([152]), (b) from ([153]) and (c,d) from ([144]).*

4.1 eV Emitter

One of the earliest known defects in hBN emits in the UV with a ZPL at 300 nm and has been referred to as the 4.1 eV emitter. The emitter has a very distinct emission spectra with two strong PSBs emitting at 330 and 360 nm as seen in Figure 1.7(b).[154] The emitters are both CL and PL active with no notable effects on the emission spectra under different excitation methods.

So far no consensus has been reached on the structure of this emitter but there is evidence to link the inclusion of carbon into the hBN lattice as a necessity to form these emitters. Secondary

ion mass spectrometry (SIMS) monitoring of hBN crystals with the 4.1 eV defects showed increased levels of carbon and oxygen.[154] Furthermore isolated carbon-rich domains were shown to exhibit this emission on isolated regions of exfoliated hBN crystals.[155] Post-growth annealing in carbon rich conditions can also induce this emission in highly crystalline hBN that otherwise only showed the excitonic band gap emission prior to any treatments.[156] Notably, several works using DFT simulations have proposed a defect structure of a substitutional carbon dimer at neighbouring boron and nitrogen sites (C_BC_N).[157,158] Longer substitutional carbon chains have also been proposed including a substitutional hexagonal carbon ring.[159]

Regardless of the true origin of such emission, it has proven to be a useful indicator of an ability to create another class of emitters outlined below. The work undertaken in chapter 4 describes this correlation in more detail.

Blue Emitter

Most recently a new class of defects has been studied and will be referred to as the blue emitter in this thesis. Originally seen only in CL measurements these emitters were first thought to be based on residual barium precursor remaining from the hBN growth.[160] The emitters had a consistent spectral emission with a ZPL at 436 nm and were seen to be activated by electron beam irradiation in an SEM (Figure 1.8(a)) A dependence upon the density of the emitters activated and the overall electron fluence was observed, as seen in Figure 1.8(b). Attempts to see PL spectra from the emitters was unsuccessful and it was proposed that electron irradiation was shifting the emitters into an emissive charge state.

More recently Fournier et al[161] were successful in measuring single defects with the same emitter in PL. The ZPL was consistent with the prior CL study[160] at 436 nm, with photon counting statistics showing that isolated single emitters could be located (Figure 1.8(c,d)). Rather than scanning the electron beam to create emitters, a defocused beam was used to irradiate a series of spots along the flake with a large electron beam current of 10 nA and long overall time. Isolated emitters were located in regions surrounding these high fluence spots and as such the fabrication of these single emitters was deemed to have a higher level of control than those

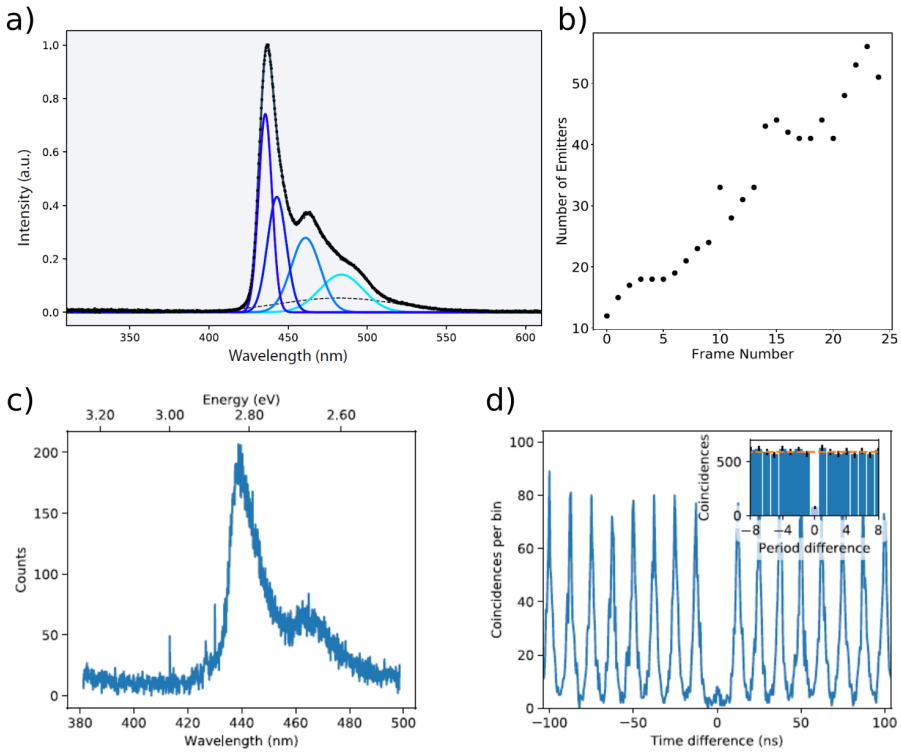

Figure 1.8: *Overview of blue emitters in hBN. a) CL spectra of the blue emitter with multi-Gaussian fits shown in blue. b) Dependence on the number of number of emitters created in an area after against the number of passes. c) PL spectra of a single blue emitter. d) Photon correlations using a pulsed 405 nm laser with raw data shown inset. Figures (a,b) sourced from ([160]) and (c,d) from ([161]).*

seen previously in hBN.

Notably, in both works the emitters were only seen in one type of hBN synthesised under high temperature and high pressure (HPHT) conditions.[161,160,154] Chapter 4 in this thesis presents work undertaken on these emitters using both CL and PL techniques to further understand the nature of these emitters, as the consistent ZPL and the deterministic nature are highly desirable for integration into devices.

1.5.3 Creation of Solid State Quantum Emitters

There are a large number of methods utilised to incorporate solid state quantum emitters into host materials. In some cases, native defects can be found either as a byproduct of the growth or manufacturing processes, without any intentional attempts to engineer quantum emitters. Many of these defects can act as single photon sources but suffer from a lack of determinism with defects will be distributed randomly.[162]

To enable integration of solid state quantum emitters into real world devices, ideally there should be some level of determinism about the creation methods used to generate or activate these defects. Three significant factors of note when attempting to use any method must be taken into account. The density of defects required in the host material, whether exact spatial position is required and specificity of the emitter type to be incorporated. Many examples only partially fulfill these criteria. A summary of the methods used for solid state emitters in diamond and hBN has been included in Table 1.2

All the methods listed have suitable applications and are highly material dependent with some specific notes and examples discussed here. In terms of fulfilling the criteria of deterministic quantum emitter creation, charged particle microscopy offers an efficient and cost effective means to achieve these outcomes. Both spatial and density control can be achieved using the focused beam and calculated dose or fluence. In many situations like diamond NV and group IV defects, dopant ions can be used directly from the ion source.[109,164] Simple vacancies can also be created directly with charged particle microscopy. FIB systems have been used for vacancy generation to make the VB defect in hBN as well as sulfur vacancies in TMDCs.[143,83,165] While the energies used in SEMs generally fall below the knock on threshold required to create vacancies, EBIE type methods have shown an ability to create single photon emitters. Nitrogen precursors were used to activate NV centres in diamond and aqueous precursors have also shown an ability to create single photon emitters in hBN.[110,126]

As previously mentioned, damage or unwanted material modifications must always be taken into account, especially when irradiating with high energy charged particles. For example,

Method	Density Control	Spatial Control	Examples	Notes
Growth Modifiers	Yes	No	- Diamond group IV defects [163] - Carbon based defects in hBN [81]	- Quality of the material lattice may be affected.
Ion Implanter	Yes	Yes*	- Diamond NV centres [107,108]	- Unlimited range of ion types including isotopic control.
FIB	Yes	Yes	- Diamond NV centres [109] - Diamond group IV defects [164] - TMDC S Vacancies [83,165]	- Energies up to 30 keV. - Limited choice of ions based on source type.
SEM	Yes	Yes	- Diamond NV centres [110] - Blue emitters in hBN [161] - Yellow emitters in hBN [132,133,134]	- Energies up to 30 keV.
TEM	Yes	Yes	- Diamond NV centres [111,112]	- Energies up to 300 keV.
MeV Electron Irradiation	Yes	Yes*	- Diamond NV centres [113] - Visible emitters in hBN [138]	- Energies used $\sim$ 2 MeV but up to 155 MeV. [166]
Laser Ablation	Yes	Yes	- Boron vacancies in hBN [145] - Visible emitters in hBN [167]	- Femtosecond laser pulse irradiations.
Plasma Methods	Yes	No	- Visible emitters in hBN [168,137] - Emitters in ZnO [169]	- Generally material specific and/or limited to choice of suitable plasma source - Quality of material lattice generally affected.
Annealing Methods	Yes	No	- Visible emitters in hBN [137]	- Often used in addition to other methods.

Table 1.2: *Overview of methods used to incorporate or produce luminescent defects in materials.*
**Spatial control is only possible utilising masking techniques*

with any form of electron irradiation a large number of factors must be taken into account with effects including heating, electrostatic charging, ionisation damage, displacement damage,

sputtering and electron beam induced effects.[41] Similarly ion beam irradiations can result in sputtering, vacancy generation, amorphisation and implantation which can negatively impact the host materials.[50]

2

Methods

2.1 Preamble

Utilisation of a single photon source in any application requires knowledge of the source that can only be gained through characterisation. Proper analysis must undertaken so that the properties such as emission wavelength, brightness, stability and purity among others can be documented. When working with single photon emitters, photoluminescence (PL) and cathodoluminescence (CL) are two commonly used characterisation techniques. Multiple different variants of each are used in research and industry settings, however this chapter will give an overview of each technique with a particular focus on their use in characterising solid state quantum emitters. These techniques are used extensively in the experimental Chapters 3,

4 and 5 and so it also serves to explain the methods used in some additional detail not always covered in the published research works. Specifics of the experimental setups used for each work will also be outlined in their respective chapter.

2.2 Photoluminescence

Probably the most important property of any solid state colour centre is the characteristic of the light emitted during the relaxation of an excited electron back to the ground state. PL spectroscopy is used extensively for this purpose and with proper characterisation of the fluorescence, a range of information can be gathered about the system. PL measurements are generally undertaken using confocal microscopes which are used across a range of scientific disciplines, not just photonics.[170,171] The term confocality refers to the uniform image plane from which the luminescence information is recorded.

Each particular setup will have differences but most require some basic components in order to function. Firstly a light source is required in order to excite the defect such that fluorescence is emitted, usually in the form of monochromatic laser. A series of mirrors are used to align the beam and an objective or lens used to focus the excitation light onto the sample and collect the emission. Fluorescence can distinguished from scattered laser light using appropriate filters and additional optics or fibres can be used to send light to photon counting detectors or spectrometers. To achieve proper confocality, a pinhole in the form of a physical aperture must be used in order to restrict lateral diameter and depth of the collected light. Some further discussion on confocality requirements is available in Appendix A. A simple PL setup can be seen in Figure 2.1(a) with a piezo-controlled scanning stage used for nanometer scale movement of the sample, thus enabling mapping functionality. As an alternative to sample scanning, a $4f$ telescope system may be utilised. This requires two additional lenses before the objective and a scanning mirror. While slightly more complex to set up, benefits include a larger scanning range not limited only by a scanning stage and an ability to decouple excitation and collection spots if used in conjunction with a scanning stage. Also of note in this particular setup schematic, rather than a separate physical pinhole aperture, the diameter of the fibre core is used to achieve confocality.

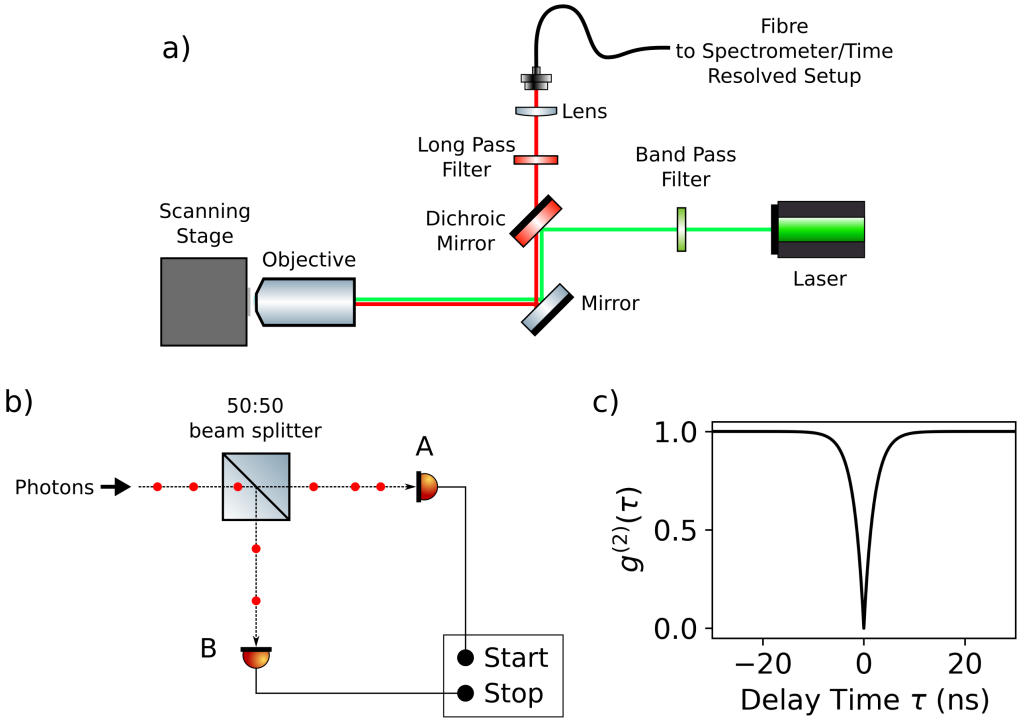

Figure 2.1: *Schematic of a simplified photoluminescence setup and Hanbury Brown-Twiss experiment. a) Schematic of a photoluminescence setup with components labelled. Sample positioning and mapping can be achieved using the scanning stage. Green and red lines indicate the excitation and emission paths respectively. Confocality is achieved using the core size of the fibre. b) Schematic of the Hanbury Brown-Twiss experimental setup with two detectors A and B connected to a time-correlating start/stop unit. Individual photons are depicted as red circles. c) An example of the correlation function $g^{(2)}(\tau)$ using continuous wave (CW) excitation for an ideal single photon source with $g^{(2)}(0) = 0$.*

With a suitable confocal microscope the PL emission from a sample can be measured. Emission from a solid state defect can be varied, with many spectral features present. The emission wavelength of the zero phonon line (ZPL) gives information as to the energy difference between the ground and excited states of the defects. Other spectral features such as the phonon sideband (PSB) can also give other information on ZPL broadening as well as how strongly coupled the defect is to vibrational lattice modes.[172] In many cases when measured at room temperature the PSB signals can be more intense than the ZPL. Both the NV centre in diamond

and 4.1 eV defect in hBN are clear examples of this.[173,153] Generally most PL spectroscopy is undertaken using excitation energies higher than the emission energy, (Stokes fluorescence); or by using resonant excitation whereby the excitation energy is exactly matched to the energy gap of the emitter. In some cases excitation energies below the ZPL are utilised (anti-Stokes fluorescence) for specific purposes including charge state manipulation[174], laser cooling[175] and suppression of linewidth broadening mechanisms.[176]

2.2.1 Single Photon Measurements

Isolated single defects are a requisite component for a number of applications. In these instances PL maps and fluorescence spectra alone are unable to determine whether an emitter is an isolated or single defect. In order to correctly identify and characterise that a defect is an isolated single photon emitter, the Hanbury Brown-Twiss (HBT) experiment can be undertaken.[177] A standard confocal microscope setup as utilised in Figure 2.1(a) can be setup so that the emission from a defect can be sent to the HBT setup present in the schematic in Figure 2.1(b). The emission passes a 50:50 beamsplitter, directing light to two single photon detectors, often avalanche photodiodes (APDs) for visible wavelengths, which are connected to a time-tagging unit. The unit can register detection events at each individual detector and record the delay times between successive events. Although not included here, a delay is introduced to one line either via software or by extending the length of physical connection cable from one detector to the time-tagging unit.

This setup can be used to identify single emitters by analysing the second-order correlation function.[91] The classical form of this function is shown in Equation 2.1 below.

$$g^{(2)}(\tau) = \frac{\langle \mathcal{E}^*(t)\mathcal{E}^*(t+\tau)\mathcal{E}(t+\tau)\mathcal{E}(t)\rangle}{\langle \mathcal{E}^*(t)\mathcal{E}(t)\rangle\langle \mathcal{E}^*(t+\tau)\mathcal{E}(t+\tau)\rangle} = \frac{\langle I(t)I(t+\tau)\rangle}{\langle I(t)\rangle\langle I(t+\tau)\rangle} \tag{2.1}$$

Where $\mathcal{E}(t)$ and $I(t)$ are electric field and intensity of the light at time t respectively. τ is the delay time and $\langle ... \rangle$ symbols are indicative of the average time integrated over a long time period. For coherent light of constant intensity $g^{(2)}(0) = 1$ as the value of $\langle I(t)\rangle = \langle I(t+\tau)\rangle$ for any value of τ. However, when considering an isolated single photon emitter these electric

fields can be quantised and considered as particles (photons). The equation for $g^{(2)}(\tau)$ can then be written in the quantised form as seen in Equation 2.2.

$$g^{(2)}(\tau) = \frac{\langle n_1(t) n_2(t+\tau) \rangle}{\langle n_1(t) \rangle \langle n_2(t+\tau) \rangle} \tag{2.2}$$

Where $n_i(t)$ is the number of counts registered by detector i at time t. From the HBT setup in Figure 2.1(a) it can be seen that the value of $g^{(2)}(\tau)$ is dependent upon the counts registered by detector A at time t and time $t + \tau$ at detector B. When light is considered to be comprised of individual photons it is also notable that it should be possible to see $g^{(2)}(0)$ having a value < 1. As each photon hits the beamsplitter there is a 50% chance that it will be transmitted and continue to detector A or reflected toward detector B. In fact, for a perfect single photon emitter this value should be 0, given that it is not possible to have two simultaneous correlation events at $t = 0$ when the photons are generated from a source with clearly defined emission events. If the photons are coming from an ideal single mode source, they can be represented in terms of a photon number state or Fock state $|n\rangle$, a quantised monochromatic field with n photons. At $\tau = 0$ Equation 2.2 can be simplified to Equation 2.3 where n can be considered to be the number of ideal single photon sources.

$$g^{(2)}(0) = 1 - \frac{1}{n} \tag{2.3}$$

In reality these conditions are difficult to realise. In a solid state system the signal from a background source or some fluorescence from the material itself can add to the emission of photons and increase the value of $g^{(2)}(0)$. Slow response times on the detectors and time correlating unit can also increase the the value of $g^{(2)}(0)$ especially when measuring single photon emitters with nanosecond scale lifetimes. For an HBT measurement of an ensemble of two single photon emitters $n = 2$, from 2.3, the theoretical value of the value of $g^{(2)}(0) = 0.5$ and as such the arbitrary value of the value of $g^{(2)}(0) < 0.5$ has been chosen as an indicator of single photon sources in peer-reviewed literature. In some cases two emitters spatially located under the excitation spot can also result in a $g^{(2)}(0) < 0.5$ if there is a substantial difference in brightness between emitters.

Experimental data can also be fit with the three-level model, accounting for any bunching effects as follows:

$$g^{(2)}(\tau) = 1 - e^{\frac{-\tau}{\tau_1}} + ae^{\frac{-\tau}{\tau_2}} \tag{2.4}$$

The lifetimes τ_1 and τ_2 refer to a fast and slow component, namely the emitter lifetime and bunching component.

2.2.2 Fluorescence Lifetime Measurements

Another time resolved measurement that is critical when characterising quantum emitters is the fluorescence lifetime τ_R of an emitter. For an ideal emitter acting as a two level system with ground and excited states $|1\rangle$ and $|2\rangle$ respectively, the lifetime is given by:

$$\tau_R = \frac{3\pi\epsilon_0\hbar c^3}{\mu_{12}^2\omega^3} \tag{2.5}$$

with vacuum permittivity ϵ_0, Planck's constant $\hbar$, the speed of light c, transition dipole moment between $|1\rangle$ and $|2\rangle$ $\mu_1^2 2$ and angular frequency ω. Lifetime can be considered as the average time for an electron in the excited state to relax and emit a photon.

Experimentally, lifetime measurements require a pulsed excitation source and one APD connected to a time tagging unit triggered by the source. To extract the lifetime τ_R, data can be normalised and fit with exponential curves of the form:

$$I = \alpha e^{\frac{-\tau}{\tau_R}} \tag{2.6}$$

with intensity I, amplitude coefficient α and time τ. Especially for systems with short lifetimes the incidence response function (IRF) must be measured so as to ensure that the laser pulse is shorter than the lifetime of the fluorescence signal. This can be achieved by measuring the scattering of the attenuated excitation source on a material with no fluorescence in the detection region. For lasers emitting in the visible spectral region, silicon may be used as it only exhibits fluorescence in the IR range.

2.2.3 Optically Detected Magnetic Resonance

For many solid state systems with addressable electronic spin configurations, a means to measure and control the spin state of system is necessary. Optically detected magnetic resonance (ODMR) is a particular technique used to polarise and read out the electronic spin state of a solid state quantum emitter. As Chapters 3 and 5 focus on the NV^- and $V_B{}^-$ defects respectively, focus will only be on spin-1 systems such as these.

These systems have a ground and excited state each with subsystems based on the magnetic spin $M_s = -1, 0, 1$. Notably there is also the addition of a singlet state. For the NV^- and $V_B{}^-$ the energy difference D_g between the spin sub-levels is in the microwave region.[178,142]

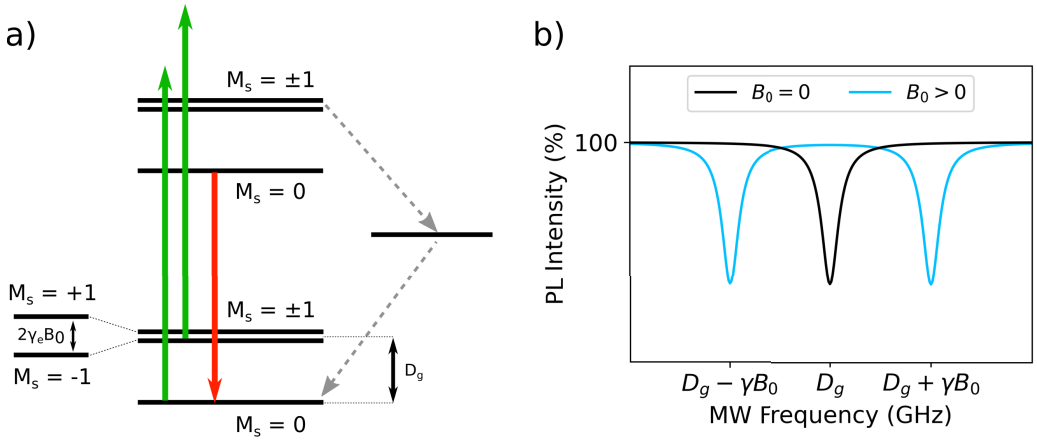

Figure 2.2: *Electronic level structure and ODMR of a spin-1 system a) The electronic level structure for a general spin-1 system. Excitation from the* $M_s = 0$ *and* $M_s = \pm1$ *ground states is represented by the green arrows. Relaxation from the* $M_s = 0$ *excited state is represented with a red arrow, indicative of a radiative transition. The grey dotted arrows represent non-radiative transitions from the* $M_s = \pm1$ *to ground state via a singlet state. (b) Simulated ODMR spectra under zero magnetic field (*$B_0 = 0$*) with fluorescence contrast at the resonance microwave frequency* D_g *plotted in black. Blue ODMR spectra shows the same system in the presence of a magnetic field with typical Zeeman splitting.*

Figure 2.2(a) shows the electronic structure for a spin-1 system such as NV^- and $V_B{}^-$. Typically a laser (green arrow) can be used to excite transitions into an excited state which can relax radiatively (red arrow). If a magnetic field is introduced on resonance with D_g the electron

spin can be driven to the $M_s \pm 1$ state. In this state, under laser excitation, spin preserving transitions allow for the electron to be excited into the corresponding $M_s \pm 1$ state. From this state another non-radiative transition can occur to the metastable state (grey dashed arrow). This transition is spin selective and more likely from the $M_s \pm 1$ excited state. This non-radiative transition results in a loss of fluorescence and as such a minima will appear as a microwave is scanned across the resonance D_g as seen in Figure 2.2(b). If an additional magnetic field B_0 is introduced the $M_s = \pm 1$ states can be split in a process known as Zeeman splitting. This results in two distinct resonances corresponding to each of the $M_s = +1$ and $M_s = -1$ states.

In a standard experimental setup utilised for the work in Chapters 3 and 5 a microwave antenna in the form of a copper wire is placed in close proximity to the sample in order to drive the transition between $M_s = 0$ and $M_s = \pm 1$ states. PL intensity is recorded across the sweep range with microwave on and off. The difference in intensities can then be extracted to get the raw ODMR contrast.

2.3 Cathodoluminescence

CL as implied by the name, is light generated from the inelastic scattering of primary electrons (cathode rays) impinging on a sample. Due to the relatively high energy of primary electrons used for CL characterisation, a very broad range of transitions from the UV to IR can be analysed. It is a powerful tool which can probe band-gap transitions[116], material defects[179,180,181] and plasmonic systems[182] among others. CL analysis can be undertaken in a range of systems including SEM, TEM and optical microscopes with CL stage.[183,184,185] Later work in Chapters 4 and 5 utilise SEM based CL techniques for analysis and so more detail will be presented in this section. Most commonly light is collected via a parabolic mirror located above or below (in the case of TEM CL) the sample to collimate the emitted light and direct it toward the detection optics. In some cases lenses or objectives can be placed above or below the sample for collection.

There are two types of CL that can be differentiated based on the phase relationship between excitation and emission. If there is no phase relationship between and emitted photon and the

incoming electron the emission is described as incoherent. On the other hand, coherent CL describes emission with a fixed phase relationship between excitation and emission. Generally incoherent CL is the dominant form of excitation in most materials. Incoherent emission can be seen from band-gap and defect transitions and as such is well suited to both host material and quantum emitter characterisation.

The CL seen from luminescent defect centers is mostly from incoherent emissions. CL is well suited to characterising these systems and has the benefit of uncovering information about the host material as well as the defect.[116] Many CL studies have looked into properties of hBN emitters including the 4.1 eV defect[153,186], blue[160] and visible emitters.[131] Often the emission seen in PL measurements are not always spectrally equivalent or even visible in CL. In the case of the V_B defect the typical broad emission has not been seen under electron excitation.[187] Similarly, for the Nitrogen Vacancy NV centre in diamond under electron irradiation, only emission from the neutral charge state is visible, indicative of a charge switching mechanism.[104]

Time resolved measurements are not only restricted to PL experiments. A unique effect when undertaking CL measurements is possible when emission is sent to an HBT setup (see Figure 2.1(b)). SPEs under electron excitation can also emit single isolated photons and as such the measured photon statistics are identical to those seen in PL experiments with anti-bunching and a $g^{(2)}(0)$ value trending toward 0.[188,153] Interestingly for ensembles of emitters, the behaviour can deviate from the expected $g^{(2)}(0) = 1$ seen in PL when using low beam currents. Significant bunching at zero time delay or more specifically $g^{(2)}(0) >> 1$ can occur under electron excitation.[189,190,191] Given a low enough beam current, the time delay between subsequent excitation events is relatively long when compared to the timescale of the emission lifetime. As each electron interacts with the substrate material it has sufficient energy to excite bulk plasmons within the material. These bulk plasmons can decay and excite multiple electron-hole pairs on picosecond timescales. Based on the lifetime of the emitter these electron-hole pairs can recombine a the colour centre based on the lifetime of the emitter type. The relatively short timescales of the electron-hole pair generation as compared to the lifetime means that

the excitation events can be considered simultaneous. As beam currents increase this effect is reduced, as seen in the schematic representation in Figure 2.3.

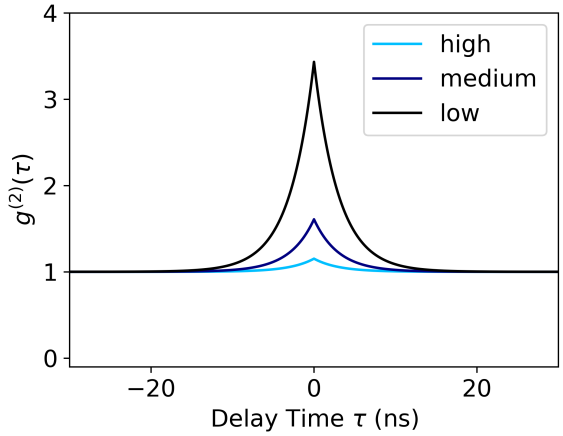

Figure 2.3: *Schematic representation of photon bunching under three electron beam currents (low - high). With decreasing current there is an increase in the bunching at zero delay such that* $g^{(2)}(0) >> 1$.

3

Recoil Implantation of Gas Phase Precursors

3.1 Preamble

Ion beam implantation is a commonly used technique to implant or create emitters in a range of materials. Although the methodology is well established, typical implantation systems suffer from some drawbacks. This chapter explores and builds upon an alternate technique utilising recoil implantation with a commercially available dual beam microscope with a FIB system.

The updated method substitutes the metal thin film utilised in earlier work to implant NV centres in diamond with nitrogen containing gaseous precursors species, simplifying and expanding the use cases for this technique.[1] This chapter includes text and figures from the peer-reviewed journal article; Gale, A. et al, *Recoil implantation using gas-phase precursor molecules*, Nanoscale, 2021.[2]

3.2 Introduction

Ion implantation techniques are commonly used to alter material properties for a wide range of applications. For instance, it has critically underpinned the advancement of semiconductor industries towards our technology standard today,[192] and research in fields such as solid state chemical engineering, optoelectronics, and quantum science have benefited from the development of reliable implantation technologies.[193,194] Due to their importance, there remains intense interest in improving implantation methods, particularly advances in mask-free, direct-write implantation at precisely-located sites, and fabrication of dopant gradients. For example, in the field of nano and quantum photonics, precise placement of optical dopants in photonic and optoelectronic devices is required, and deterministic ion implantation techniques are therefore highly sought after.

While conventional ion implanters offer a wide range of possible implantation energies and source ions, they are unable to achieve localized implantation on sub-micron scales without the need for masking procedures.[195,107] Therefore, several methods are commonly used in material science, based on equipment beyond standard broad-beam ion implanters. This equipment includes FIB systems, which produce highly-focused, nanoscale beams. However, the ion species are limited by the ion source, which is typically a liquid metal ion source[196,197,164], a plasma source[109], or a gas field ionization source.[51] A recent demonstration has expanded this to a Paul trap, where ions are captured in an electrostatic trap and then accelerated towards a target,[198,199] and techniques such as implantation through a pierced AFM tip have been used to achieve precise spatial localization.[200,201] In addition, a more specialized technique was demonstrated recently using a scanning electron microscope and gas-phase precursor

molecules.[110]

Further to the above, the use of recoil implantation[202,203,204] in combination with a standard FIB system was recently demonstrated.[1] In that work, momentum transfer from inert ions in a nano-scale beam to a thin film was used for implantation of the film constituents. This was shown by implanting group IV elements into a bulk diamond substrate, which resulted in the creation of group IV color centers. These centers have characteristic PL emissions,[79] which were distinctly identified by confocal PL measurements. The recoil implantation technique provides control over dopant density using the ion beam irradiation and scanning parameters, and enables ultra-shallow implantation, with the majority of dopants located within the first 2 nm of the surface.[1] Hence, this technique allows for a wide range of implant species using a single ion source, as well as beam-directed control over the location and density of the dopants. However, it is limited to the use of solid-state precursors that can be deposited in the form of a removable film. Here this limitation is eliminated by replacing solid thin films with gases that are injected into the system during FIB irradiation. This approach enabled the creation of NV centers[205] in a diamond substrate by using N_2, NH_3 and NF_3 as the implantation precursor species.

It is noted that whilst undesired recoil implantation of gas-phase oxygen impurities by broad ion beams has been observed previously[206], this process has not been used to engineer functional material properties such as the generation of NV spin defects in diamond demonstrated in the present work. These results expand the technique of FIB-directed recoil implantation to encompass the vast majority of the periodic table, demonstrates the use of both inert and reactive precursor molecules, and negates the need for thin film deposition and removal steps that may be difficult depending on the properties of the substrate.

3.3 Methods

3.3.1 Preparation of diamond

The substrate used in this work is electronic-grade diamond (N < 5 ppb) purchased from Element Six, cleaned prior to experiments by ultrasonication in acetone, isopropanol and piranha solution

(H_2SO_4:H_2O_2 (30%) 2:1 at 150 °C, 2 hours). This sample was then placed without any further modification in the dual beam microscope.

After irradiation, the sample was annealed at 850 °C for 2 hours in high vacuum ($< 2 \times 10^{-6}$ mBar) and cleaned in piranha solution as described above.

3.3.2 Ion Implantation

A standard dual beam microscope (DBM - Thermo Fisher Scientific Helios G4) was used for the ion implantations. A 30 kV, 4.7 ± 0.3 pA, Ar^+ ion beam was chosen for all ion irradiations. By using the included scanning software and precise timing control capabilities of the FIB system, a variation of the irradiation fluence was achieved by altering the number of passes per unit area scanned by the beam. In each pass, the beam is scanned in a serpentine pattern with a Dwell Time of 200 ns, a Point Pitch of 200 nm, and a defocus of 50 µm, which yields a fluence of 1.7×10^{10} ions/cm^2 for a single pass.

3.3.3 Gas Injection

The system was equipped with a gas injection system(GIS), with a capillary placed within 500 µm of the substrate to locally deliver precursor molecules. A schematic of the experimental setup can be seen in Figure 3.1 including the gas lines and equipment utilised. For the gas supply (either N_2, NF_3, or NH_3), the GIS was connected to an external gas line, through a connector at the capillary. The gas was then delivered to the capillary through a gas line, where a liquid nitrogen cold trap was used to minimize residual water content in the gas stream delivered to the sample.[66] During all gas injection experiments the flow was controlled by a needle valve, which was placed in the gas delivery system. The valve was adjusted until the background chamber pressure increased from 1.3×10^{-6} mBar to 9.0×10^{-5} mBar. For experiments with NF_3 and NH_3 an enclosed gas box was utilised with a gas sensor. The gas box was connected to an exhaust line so that negative pressure was always maintained within the enclosure. Pneumatic valves were utilised with a bypass pathway at the needle valves allowing for the lines to be pumped out to the regulator to increase gas purity.

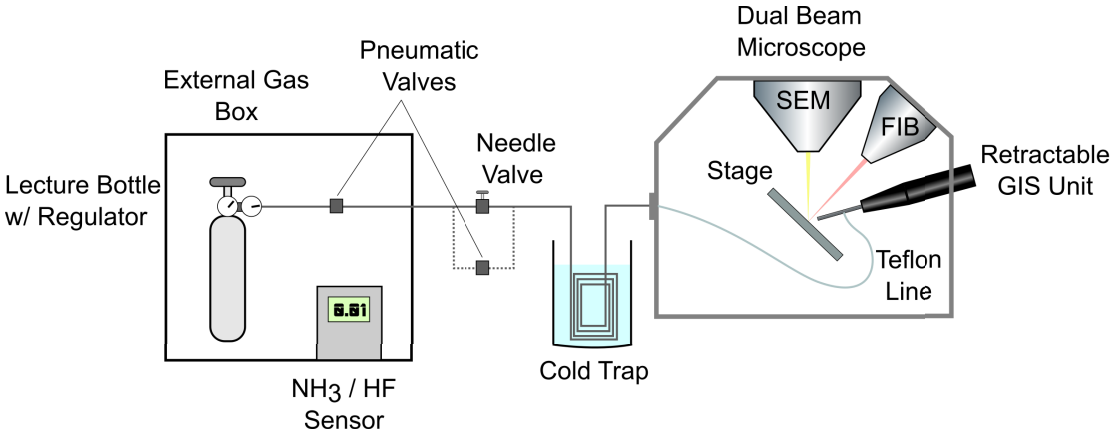

Figure 3.1: *Schematic of the precursor and GIS setup used for recoil implantation experiments. The Lecture bottle could be replaced with the desired precursor and similarly for experiments using NF_3 and NH_3 a gas sensor was utilised.*

3.3.4 Photoluminescence Measurements

A lab-built confocal PL setup with a 532 nm CW excitation laser was used to investigate the irradiated regions at room temperature. The setup utilised a 532 nm dichroic beamsplitter with a scanning mirror (Newport FSM-300) and 4f system for scanning. Mapping data was collected using an avalanche photodiode (Excelitas SPCM-AQRH) or fibre coupled spectrometer (Princeton Instruments, Inc.) for spectra. ODMR measurements utilised a copper wire with a diameter of 30 μm placed near the sample. Microwave signal from a generator (Anapico aspin) was amplified (minicircuits, ZHL-16W-43-S+) and directed through the wire. The microwave frequency was swept between 2.75 and 2.95 GHz and the PL emission was recorded using the avalanche photodiode with the microwave on and off.

The method uses a standard dual beam microscope (Thermo Fisher Scientific Helios G4), a tool that is commonly available in microscopy and material science laboratories for purposes of cross sectioning, lamella preparation for transmission electron microscopy, and for nanofabrication.[50,47] The same system is typically equipped with a gas injection system (GIS), where a capillary is placed within 500 µm of the substrate and used to locally deliver precursor molecules for gas-assisted nanofabrication, e.g. chemical vapor deposition or chemically-enhanced etching of the surface. Here, the same system is utilized for sub-surface implantation of gas molecule constituents, achieved by injecting and delivering nitrogen-based precursor gases to a local area of a substrate during FIB irradiation, as is schematically shown in Figure 3.2(a). As the gas molecules are injected and directed towards the sample, a proportion will adsorb on the surface. These gaseous molecules will either diffuse on the surface or undergo thermal or FIB-induced desorption, characterized by the diffusion path length and the mean desorption time, respectively.[59,207] Within this timeframe, high energy primary ions can interact with the adsorbates, transfer momentum to the molecules, and thus implant their constituents into the substrate.

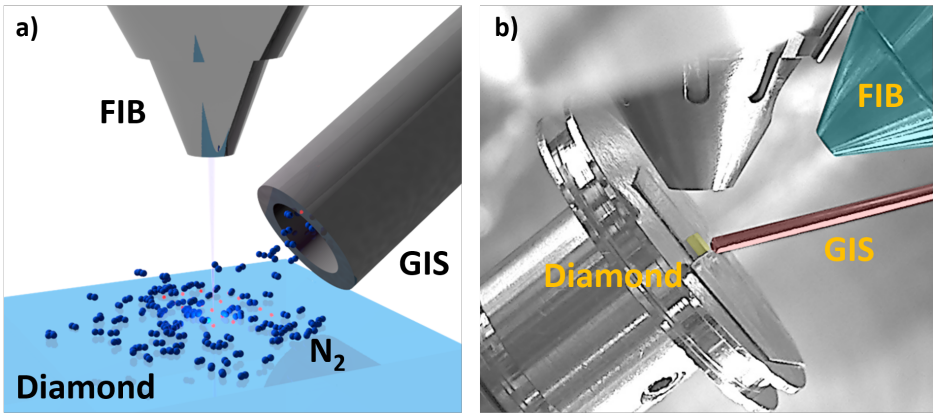

Figure 3.2: *Experimental Setup. (a) Schematic illustration of the setup used in the experiments with stylised N_2 molecules and a focused ion beam. (b) Chamber scope image of the experimental setup used for all implantations with false colouring applied to labelled components*

Figure 3.2(b) shows a charge coupled device (CCD) image of the setup during the experiment, where the GIS needle was placed within 500 µm of the sample surface for optimal gas flux at the surface. Note that the pressure increase is measured at a peripheral point relative to the substrate – however, the local pressure increase in the vicinity of the processing area is known to be substantially higher, as typically used for applications in electron/ion beam induced deposition (IBID).[59] Also note that Ar^+ is used instead of Xe^+, because the momentum transfer is maximized when the atoms are similar in mass, and thus can achieve better implantation conditions.[202] Furthermore, Ar is lighter than Xe, causing less collateral damage to the host crystal. Unlike Xe, Ar is not known to produce any luminescent color center in diamond, hence it should act as a truly inert primary ion in this system. Other ion species commonly found on FIB units could also be used for this purpose. Commercially available Ne based FIB systems would further reduce both the mass difference and additional damage to the host crystal. An energy of 30 keV was chosen for all ion irradiations to maximise the depth of the implanted nitrogen.

By using the scanning and precise timing control capabilities of the FIB system, a straightforward variation of the irradiation fluence was achieved by altering the number of passes per unit area scanned by the beam. Due to the volatile nature of the adsorbates, a refresh time was also applied, which was set to 10 ms between passes in order to facilitate sufficient time for the precursor molecules to replenish around the processing site.[208] Specifically, as the ion beam irradiates the sample, the precursor gas may either be implanted by recoil, auto-desorb or undergo stimulated desorption caused by the ions and secondary electrons emitted from the substrate.[209] Hence, during FIB radiation, adsorbates at the implantation site are depleted and their concentration has to be replenished continuously.[210] It should be emphasized here that for this version of recoil implantation, no deposition of a thin film in any form is required, which also removes the need for post-implantation sample treatments that are needed to remove such films.

After ion irradiations the resulting PL map of an area irradiated with the precursor NF_3 can be seen in Figure 3.3(a). An ion fluence of 7.0×10^{13} ions/cm^2 is required to clearly see the

patterned $4 \times 4\,\mu m^2$ squares in the confocal PL map. This is higher than but comparable to previous work using solid metallic precursors, where a fluence of less than 1.0×10^{12} ions/cm^2 was needed to observe patterned regions of the same size.[1] The direct comparison for creation of different types of color centers is valid under the implantation and annealing conditions as the NV was reported to have a creation yield of $\sim$1 % for low energy ion implantation, similar to the yield of the SiV and the GeV.[196,164] The values obtained in this study are higher because of the lower concentration of adsorbates on the surface compared to a solid thin film and the ability for the gaseous precursors to desorb or diffuse unlike the solid metallic precursor. This naturally results in a lower probability of the recoil process, and therefore requires higher total fluence values. Moreover, these values are also significantly higher than using direct nitrogen ion implantation which often require fluences of $\sim 1.0 \times 10^{10}$ ions/cm^2 as there is an added requirement for momentum transfer between the primary ion and precursor.[195,107] As is common for all forms of ion implantation and observed here, the PL intensity increases up to a maximum and then saturates or declines as ion fluence is increased. The maximum PL intensity is obtained at a fluence of 7.0×10^{14} ions/cm^2 at which point it begins to decrease in the center of the irradiated region. This is related to the increased amount of collisions within the sample, which leads to irreparable damage in the crystal and therefore quenching of the emission. The threshold of decreasing luminescence for ions in related studies on the NV and the SiV were observed to be on the order of $10^{13} - 10^{14}$ ions/cm^2, consistent with the observation of a decreased luminescence at this fluence.[196,211] The likely explanation for the observation of a slightly higher value of this critical fluence is that most of the damage, as introduced by the primary Ar ions, is generated in a depth below the region of the recoil implanted nitrogen.[1]

Figure 3.3(b) shows individual PL spectra from the square centers, clearly showing the increased intensity of NV^- emission with a pronounced broad phonon sideband (PSB) and a characteristic zero phonon line (ZPL) at ~638 nm. Furthermore, in the spectrum a distinct Raman line at 573 nm is observed, corresponding to the F_{2g} mode (1332 cm^{-1}) of the sp^3 bond, characteristic for the crystal structure of diamond. A further peak is observed at 582 nm, assigned partially to the G band, indicating some degree of damage in the material, as well as the NV^0 emission, which is typically present at 575 nm. The presence of the G band in the spectra of all fluences indicates a damage that is higher than with standard FIB implantation, as much higher ion beam fluences are required and the G band is typically absent.

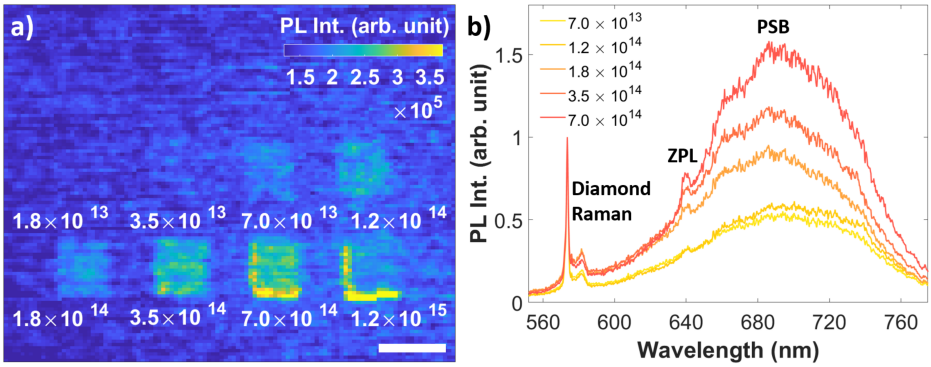

Figure 3.3: *PL map and spectra of implanted arrays of NV centers. (a) A room temperature confocal PL map of square NV arrays implanted using NF_3 precursor. The scale bar corresponds to 5 µm. (b) Spectra taken from irradiated areas in (a) corresponding to ion fluences in the range of* $7.0 \times 10^{13} - 7.0 \times 10^{14}$ ions/cm^2. *The NV^- zero phonon line (ZPL), phonon side band (PSB) and diamond Raman line are labelled for clarity. The spectra have been normalized to the Raman peak at 573 nm.*

Now to a brief discussion on the non-trivial kinetics arising from the interplay of momentum transfer processes and gas diffusion above and on the surface. Firstly, the choice of a diamond substrate and PL analysis of NV centers prove conclusively that the nitrogen is implanted below the surface and embedded in a diamond crystal – i.e., the ion irradiation did not merely generate a thin film of nitride that can form on some materials as a result of beam-stimulated chemical reactions between adsorbates and a surface. Next, the appearance of distinct box

shapes in Figure 3.3(a) with clear edges blurred only by the resolution of the confocal PL imaging system is a direct indicator that the implantation is initiated by momentum transfer to adsorbed gas molecules rather than the less-probable process of momentum transfer to gas-phase molecules above the sample. If the latter was the case, the angular distribution resulting from non-head-on collisions between primary ions and gas molecules would inevitably result in blurred, overlapping implantation sites. Finally, it is highlighted that the employed FIB irradiation conditions do in fact lead to net nitrogen implantation, which is not negated by the net competing effect of sputtering and desorption stimulated by the ions and emitted secondary electrons.

Now turning to a comparison of implantation from different gas species and characterization of the ODMR signal.[205] First, Figure 3.4 (a) shows spectra obtained using different nitrogen-based precursors, namely N_2, NF_3 and NH_3, each of which was irradiated using an ion beam fluence of 3.5×10^{14} ions/cm^2, at a chamber pressure of 9.0×10^{-5} mBar. Within the different regions, NF_3 showed the brightest PL, followed by N_2 and NH_3 respectively. These variations in efficacy are likely a result of the complex interplay between residence times of the precursor molecules, ion-adsorbate interaction cross-sections, adsorbate dissociation mechanisms and chemical effects of reactive H and F species. As an example, NF_3 and NH_3 molecules have longer surface residence times than N_2. In turn, it can be expected that NH_3 would more likely lead to H-mediated chemical etching of diamond, as it has been shown that hydrogen containing precursors can etch carbon. This may directly explain the order of the PL intensity, with NF_3, the highest due to long residence times, while for NH_3 the additional etching mechanism leads to slow beam-induced volatilisation of the surface.[212,213] Moreover, due to co-implantation of hydrogen, the NV^- center can be depleted and become optically inactive.[214]

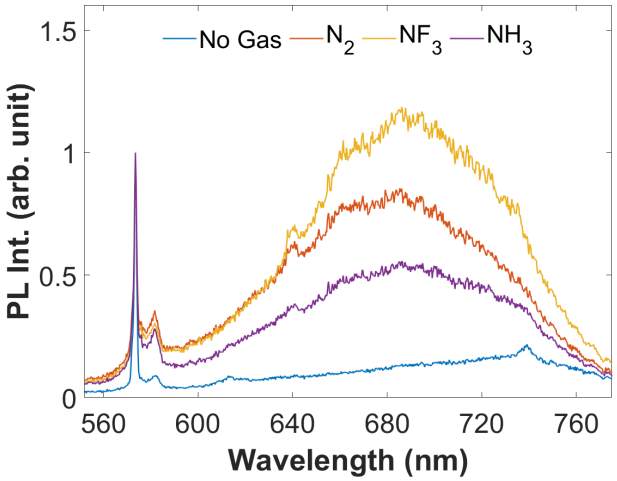

Figure 3.4: *Comparison of PL spectra using different nitrogen-based precursors showing room temperature PL spectra of the implanted regions using a fluence of* 3.5×10^{14} ions/cm^2. *A reference spectrum of a region irradiated in the absence of a precursor gas is shown for comparison. The* NV^- *zero phonon line (ZPL), phonon side band (PSB) and diamond Raman line are labelled for clarity. The spectra are normalized to the diamond Raman line at 573 nm.*

Besides the characteristic PL emission, a clear PL contrast was observed when applying a microwave field, a signature of the NV^- ODMR. Specifically, a microwire was placed in the vicinity (∼20 µm) of an irradiated square region (7.0×10^{14} ions/cm^2 fluence, N_2 precursor) and the PL contrast was recorded as the microwave frequency was sweeped across the range 2.75 – 2.96 GHz. As shown in the inset of Figure 3.5(a) a PL contrast of ∼1.5 % was observed at 2.87 GHz, corresponding to the zero-field splitting of the system, separating the electron spin $|0\rangle$ and $|\pm 1\rangle$ sublevels of the ground state (Fig. 3.5(b)). Note that the ODMR peak is relatively broad, indicative of strain in the sample and the maximum contrast is well below the state of the art systems reaching 19%.[215] Nevertheless, the ODMR measurement shows the capability of this technique to generate spin defects in diamond.

A comparison of the effect on gas flux was also undertaken. The same irradiations were undertaken with varying precursor gas flux controlled by the flow through the needle valve. The flow rate was controlled via the needle valve and the SEM chamber pressure was used to monitor the pressures. Figure 3.6 shows PL spectra for an ion fluence range of 1.2×10^{14} –

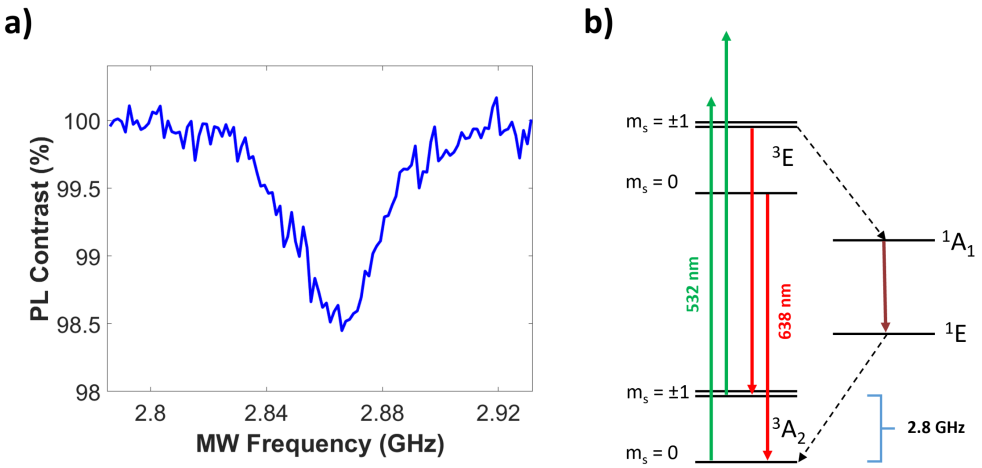

Figure 3.5: *ODMR spectrum and energy level diagram of the NV⁻. (a) ODMR contrast measurement of an area irradiated with nitrogen gas precursor. (b) Simplified energy level diagram of the NV⁻ system showing spin ground and excited, spin sub-levels and metastable state. Green arrows refer to the 532 nm excitation laser, red arrows correspond to the ZPL emission from excited to ground states and the brown arrow shows the non-radiative transition between the metastable levels.*

1.2×10^{15} ions/cm^2 at two gas flux rates, 5.8×10^{-5} and 9.0×10^{-5} mBar. For a given fluence, the higher gas flux results in higher intensity of ZPL and PSB emissions. In the present system the adsorption of the precursor gas can be described in terms of a Langmuir adsorption model. This assumes there is no dissociation of the nitrogen precursor molecules upon adsorption to the diamond surface and no interaction between the precursor molecules. For a given temperature with a gas flux J the precursor coverage θ is given by Equation 3.1[46]:

$$\theta = \frac{sJ/N_0}{sJ/N_0 + 1/\tau} \tag{3.1}$$

With sticking probability s, density for a monolayer of precursor molecules N_0 and precursor molecule residence time τ. It is apparent that under this model the precursor flux J has a significant effect on the density of adsorbed precursors. Given that the rates of diffusion, desorption and dissociation are unaffected by gas flux it is clear that the increased precursor

coverage leads to a higher probability that momentum transfer between a primary ion and precursor molecule will be initiated, resulting in the increased intensity of NV^- emission for a given ion fluence.

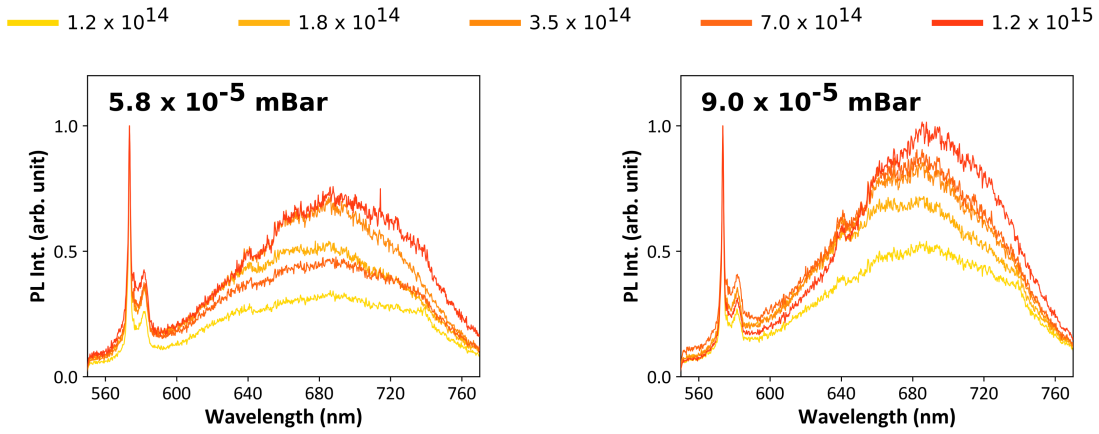

Figure 3.6: *Comparison of PL spectra with differing nitrogen gas flux. Room temperature PL spectra of the implanted regions with ion fluences listed above in units of* ions/cm^2. *The spectra are normalized to the diamond Raman line at 573 nm. The measured chamber pressure for each panel is listed in bold text.*

Finally, to exclude the possibility that the NV^- centers were generated by ion beam processing of native nitrogen impurities in the diamond substrate (N < 5 ppb), or from nitrogen impurities in the Ar^+ beam, implanted regions were compared to areas that were irradiated by the beam in the absence of a precursor gas. As is shown by the blue spectrum in Figure 3.4(a), the characteristic NV^- emission was absent from such regions, irradiated using the same ion fluence, confirming that the observed NV centers were generated through recoil implantation.

Bright square arrays were observed in panchromatic PL maps of the areas irradiated in the absence of a precursor gas (Fig. 3.7). However, these emissions were unstable – focusing the laser spot onto such an irradiated area and taking a further PL map results in a dim spot (Fig. 3.7. Therefore, the bright square is attributed to carbon deposition via an IBID process stemming from residual hydrocarbon species on the sample surface.[59] The laser dwelling removes the contamination, which leads to PL quenching in that spot. This illustrates that the low ion

flux used for the irradiation resulted in a favorable regime between the competing processes of sputtering, implantation and desorption/replenishment.

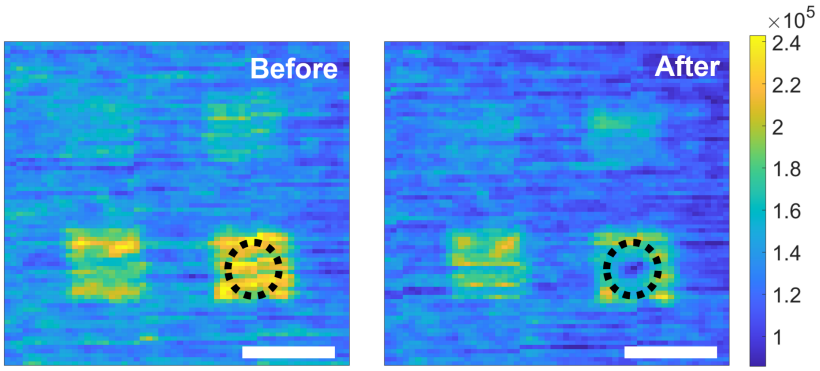

Figure 3.7: *Confocal PL maps of regions generated by ion beam irradiation in the absence of a precursor gas. Maps are shown before and after the laser spot was dwelled over the circled area for 2 min. Scale bars correspond to 5 µm.*

In this work a succinct set of experiments were undertaken – namely, site-selective fabrication of NV^- centers in diamond using three precursor gases to show that:

- Optically-active defects can be fabricated in the substrate lattice below the sample surface.
- The implantation proceeds through momentum transfer to surface-adsorbed gas molecules.
- The irradiation conditions lead to implantation at a rate that overcomes the competing processes of autodesorption, stimulated desorption and sputtering.
- The ion beam scanning can be used to control both the location and the local dose of the implanted species.
- Both inert and reactive gases can be used as implantation precursors.

3.5 Conclusion

The range and suitability of the recoil implantation technique has been extended and demonstrated its applicability to elements which are available from a gaseous molecular state. By delivering gas-phase molecules to the substrate surface by means of a GIS capillary a region of locally high adsorbate concentrations was produced, which acts as a source of target atoms that can be implanted through momentum transfer from an energetic ion beam. The principle of this extension was proven by patterning regions of optically-active NV^- centers in bulk diamond, by flowing a nitrogen containing gas over the surface during ion beam patterning. After annealing, the characteristic signature of the NV^- color center, including the spectrum and ODMR signal with zero-field splitting at 2.87 GHz were observed. Beyond the expansion of recoil implantation to a wider range of the periodic table, material preparation steps have been simplified by utilizing a gas phase precursor, where no chemical removal of the target film after implantation is required. Such a process is therefore more appealing to materials that are chemically unstable or would be affected by the wet chemical removal process after ion irradiation.

4

Site-Specific Fabrication of Blue Quantum Emitters in Hexagonal Boron Nitride

4.1 Preamble

HBN is gaining considerable attention as a solid-state host of quantum emitters from the ultraviolet to the near-infrared spectral ranges. However, the atomic structures of most of the emitters are speculative or unknown, and emitter fabrication methods typically suffer from poor reproducibility, spatial accuracy, or spectral specificity. In this chapter a robust, electron beam technique for site-specific fabrication of blue quantum emitters with a zero-phonon line at 436 nm (2.8 eV) is presented. It is shown that the emission intensity is proportional to electron dose and that the efficacy of the fabrication method correlates with a defect emission at 305 nm (4.1

eV). Blue emitter generation is attributed to the fragmentation of carbon clusters by electron impact. The robustness and universality of the emitter fabrication technique is enhanced by a pre-irradiation annealing treatment. These results provide important insights into photophysical properties and structure of defects in hBN and a framework for site-specific fabrication of quantum emitters in hBN. This chapter includes text and figures from the peer-reviewed journal article; Gale, A. et al, *Site-specific fabrication of blue quantum emitters in hexagonal boron nitride*, ACS Photonics, 2022.[3]

4.2 Introduction

hBN is an attractive Van der Waals material due to its wide bandgap and chemical stability. It has been used widely as a thin dielectric layer in electronic devices and a protective cap for sensitive materials such as transition metal dichalcogenides. Recently, its quantum photonic properties have gained considerable attention as hBN has been found to host a variety of single photon emitters (SPEs) that span the ultraviolet (UV) to the near-infrared (IR) spectral range.[131,126,153,161,216,141,217,218,139]

hBN SPEs operate at room temperature and some have outstanding optical properties including high brightness, linear polarisation and access to the spin states of some of the defects.[89,152,142] The emitters are associated with intrinsic structural defects and extrinsic impurities in the lattice, and are found in many varieties of hBN samples, including those grown by the high pressure high temperature method, chemical vapor deposition and MOVPE.[154,135,81,219] Numerous distinct defect-related quantum emitters have been identified in hBN. The various SPEs display a wide range of photophysical properties – including the emission wavelength, brightness, stability and spin properties. As a result, it is broadly accepted that numerous defect species are likely responsible for the emissions, but the atomic structures of most of these are speculative or unknown.

Consequently, numerous experiments have been conducted with the aim to engineer the emitters deterministically with reproducible emission properties.[161,143,145] These have met some success – for example, ensembles of the negatively charged boron vacancy (V_B^-) defect can

be fabricated, but these emitters are dim and have so far not been isolated at a single defect level.[143,145,220] Conversely, emitters in the visible spectral range can be engineered at a single defect level, but fabrication methods that are deterministic both spatially and spectrally remain elusive. This limits not only studies of defect structure but also efforts at scalable integration of hBN emitters in photonic circuits and devices. As a result, there is a need for improved emitter fabrication methods and detailed fundamental studies of specific fluorescent defects that can be engineered on demand in a wide range of hBN samples.

Here, a robust electron beam technique for site-specific engineering of defects emitting at 436 nm (2.8 eV), referred to as blue emitters throughout the chapter is presented. For the first time, highly controlled, dose-dependent engineering of emitters is demonstrated. The efficacy of the method is correlated with a spectral signature of hBN flakes. Employing nanoscale CL spectroscopy, it is shown that the effectiveness of the blue emitter generation process correlates with a well-studied carbon-related UV center at 305 nm (4.1 eV).[153,154,221,222,157,158,223,224,225] Blue emitter formation is attributed to decomposition of carbon clusters in hBN by electron impact, and show that the efficacy of the emitter fabrication method can be improved by an annealing treatment. The findings provide a facile approach for deterministic fabrication of quantum emitters in hBN with nanoscale resolution.

4.3 Methods

4.3.1 Sample Preparation

Si/SiO_2 (285 nm oxide) substrates were first solvent-cleaned and ultrasonicated in acetone then isopropyl alcohol before being dried in nitrogen. The substrates were further cleaned for 30 mins in a commercial ozone cleaner before exfoliating hBN using PDMS. Two different hBN bulk crystals were used: HPHT hBN from the National Institute for Materials Science (NIMS) and commercially available hBN from HQ Graphene. To remove unwanted residue after exfoliation the samples were annealed at 500 °C in air for 12 hours before being ozone cleaned for 30 minutes. A tube furnace was used to anneal samples at 1000 °C for 1 hour in a nitrogen atmosphere (1 Torr, 50 SCCM).

4.3.2 Emitter Creation

Blue emitters were created using an FEI DB235 Dual Beam FIB/SEM microscope. Beam energies of 5-10 keV and currents ranging from 8.0 pA to 4.5 nA were used for all experiments. The spectra and time-resolved data in Figure 4.2 were collected from irradiated spots on annealed HQ Graphene hBN. CL spectra were monitored during emitter creation and used to determine the irradiation time. The arrays in Figure 4.4 were patterned on annealed NIMS hBN using a 10 keV, 1.0 nA beam on squares of area 20 x 20 nm. The dose was controlled by modulating the total irradiation time from 1 - 256 seconds. For the 4 x 3 spot array in Figure 4.5, a total irradiation time of 2 seconds was used for each area. Irradiations in Figure 4.6 were performed using a 10 keV, 1.0 nA stationary beam (240 seconds for a total dose of 1.50 x 10^{12} electrons). The UTS Logo in Figure 4.1(b) was patterned on annealed HQ Graphene hBN using a Thermo Fisher Scientific Helios G4 Dual Beam microscope using a beam energy of 5.0 keV and a beam current of 0.8 nA. The area was patterned for a total of 20 minutes.

4.3.3 Cathodoluminescence Measurements

CL mapping, spectra and time correlated measurements were collected using a Delmic SPARC system with a 13 mm parabolic mirror. Data was collected using a beam energy of 10 keV and a beam current in the range of 0.28 to 1.0 nA. CL was directed to a spectrometer (Andor Kymera 193i) using a slit width of 150 µm. The spectrometer was equipped with a 300 lines/mm grating for CL mapping and spectroscopy. A pixel size of 200 nm and a dwell time of 10 ms were used for the map in Figure 4.4(a). For single spectra of the SPEs in Figure 4.2(a), a 430 nm long-pass filter was placed in the optical path to remove second order features from high energy CL emission. For time-resolved measurements in Figure 4.2(c), the CL emission was directed to a Delmic LAB Cube. This encompases a Hanbury Brown and Twiss setup consisting of a 50/50 beam splitter and two photomultiplier tube detectors (Hamamatsu R943-02). The emission was filtered using a 460$\pm$30 nm band-pass filter. The electron beam was scanned across an area of 150 $\times$ 130 nm containing an existing SPE ensemble for 1 hour using a beam energy of 5.0 keV and a beam current of 8.0 pA. Spectra presented in Figure 4.6 were collected at the beginning

and end of the irradiations outlined above. Integration times of 1 second for non-annealed hBN and 10 ms and 100 ms were used for annealed NIMS and HQ Graphene samples respectively. Delmic Odemis software was used for all data collection.

4.3.4 Photoluminescence Measurements

The room temperature PL measurements in Figures 4.1, 4.2 and 4.4, were conducted using a lab-built confocal microscope. Briefly, a 405 nm continuous-wave (CW) laser (PiL040X, A.L.S. GmbH) excites the sample via a 100× objective (NA 0.9; Nikon). The reflection/fluorescence was filtered with a dichroic mirror (long-pass 405 nm) and collected either by avalanche photodiode single photon detectors (APDs, Excelitas Technologies) or a spectrometer (Princeton Instruments, Inc.). For single photon emitter characterization, scanning was done using an XYZ piezo stage (NanoCube P-611.3), and an antireflection coating lens (350-1100 nm range) was used for collection.

The cryogenic PL measurements in Figure 4.2 were performed with a lab-built confocal setup equipped with an open-loop cryostat (a ST500 cryostat, Janis) containing flowing liquid Nitrogen. A three-dimensional piezostage (ANPx series, attocube Inc.) is located inside the cryostat to adjust the position of the samples. A cryogenic temperature controller (335, Lakeshore) was used to adjust the temperature of the samples. A thin quartz window enables optical access to the samples. A 405-nm CW laser was used to excite the samples through a 100× objective (NA 0.9; TU Plan Fluor, Nikon). Back-collected fluorescence was filtered and directed either to an APD or a spectrometer (SR303I, Andor).

For time-resolved PL spectroscopy in Figure 4.2, a pulsed 405 nm laser (pulse width of 45 ps) with a 20 MHz repetition rate was used as the excitation source. A correlator (PicoHarp300, PicoQuant) was used to synchronize PL emission.

To engineer emitters using electron beams, two sources of hBN were studied: flakes were exfoliated from hBN grown using the high-pressure and high-temperature (HPHT) method ("Type I"), and from hBN that was purchased from a commercial supplier ("Type II"). The flakes were exfoliated onto Si/SiO_2 substrates and annealed in N_2 at 1000 °C. The function of this pre-irradiation annealing treatment is discussed below. Importantly, no additional annealing was done after electron irradiation. Optical characterisation was performed using a CL system installed on the SEM used to fabricate emitters, and an ex-situ custom-built PL setup. CL analysis was performed both during electron beam processing, as well as before/after processing using a low current density electron beam that modifies samples minimally during analysis. See the Methods section for additional details.

A schematic of the CL setup is shown in Figure 4.1(a). CL is excited by high energy (keV) electrons that can excite both defects as well as inter-band transitions and is therefore complementary to PL performed using a sub-bandgap excitation source. A parabolic mirror reflects and collimates CL into a setup that enables spectroscopic and correlation measurements.

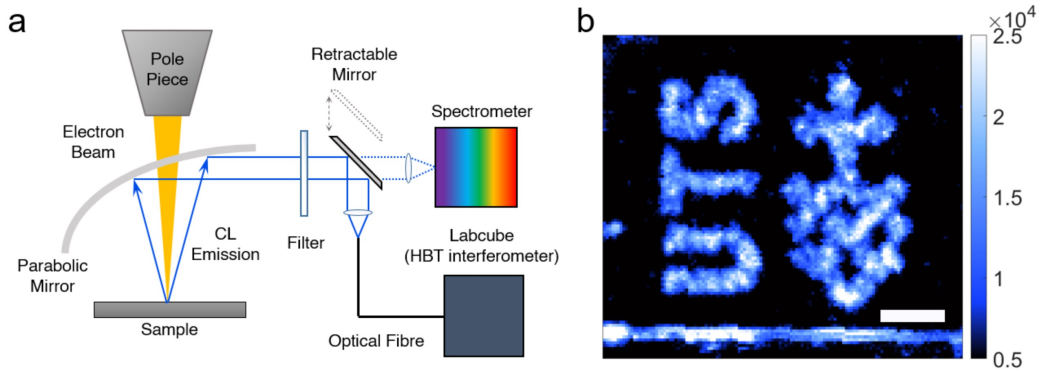

Figure 4.1: *Direct-write electron beam fabrication of blue emitters in hBN. (a) Schematic illustration of the electron beam setup used to process hBN and perform CL analysis. (b) Confocal PL map of the UTS emblem patterned by electron beam irradiation of hBN. The map was collected using a 60 nm bandpass filter centred on 460 nm. The scale bar represents 5 µm.*

As a demonstration of the spatial control and consistency of the emitter fabrication method the University of Technology Sydney emblem was written into a Type II hBN flake using a 5 keV electron beam (0.8 nA). Figure 4.1(b) shows a confocal PL map of the emblem acquired using the blue emission generated using the electron beam. The emission was collected using a 60 nm bandpass filter centered on 460 nm. The fabrication resolution is limited by the diameter of the electron beam which is on the order of only a few nanometres and electron scattering in the sample. Electron scattering is a function of the energy used and for hBN flakes up to a few 100 nm and energies of 10 keV as used here, this is up to 1 µm. Given the ability for SEMs to control acceleration voltage up to 30 keV this could be tuned as required.

Normalised, room temperature CL and PL spectra of the blue emission generated by the electron beam are shown in Figure 4.2(a). The spectra consist of a dominant peak at 436 nm and two satellite peaks at 462 nm and 491 nm. These are attributed to a ZPL and a PSB comprised of two phonon replicas, consistent with prior reports.[161,160,172,226] Differences between the CL and PL spectra are caused by a lower resolution of the CL spectrometer (see Appendix A.1, Figure A.1). A low temperature PL spectrum is shown in Figure 4.2(b). It shows expected reductions in peak widths and in the relative intensity of the PSB, and the spectrum is consistent with prior studies of emitters in hBN[227,228] – the apparent asymmetry in the ZPL is attributed to a ZA (out-of-plane acoustic) phonon replica detuned from the ZPL by 10 meV, and the longer wavelength emissions are consistent with the phonon modes of hBN.[172,229]

Photon emission statistics were analysed using both CL and PL. The blue curve in Figure 4.2(c) is a second-order CL autocorrelation function, $g^{(2)}(\tau)$, measured using a 5 keV (8 pA) electron beam, from an ensemble of the blue emitters. It shows significant bunching, with a $g^{(2)}(0)$ value of 4.53 $\pm$ 0.03. Photon bunching is typical of CL emissions from quantum emitter ensembles excited using a low current electron beam, and has previously been ascribed to simultaneous excitation of an ensemble by bulk plasmon decay.[189] A mean emitter lifetime of 2.11 $\pm$ 0.03 ns was extracted from a single exponential fit of the CL $g^{(2)}$ function. This value is consistent with and typical of the excited state lifetimes of emitters in hBN.[230] A second-order PL autocorrelation measurement from a single blue emitter generated by an

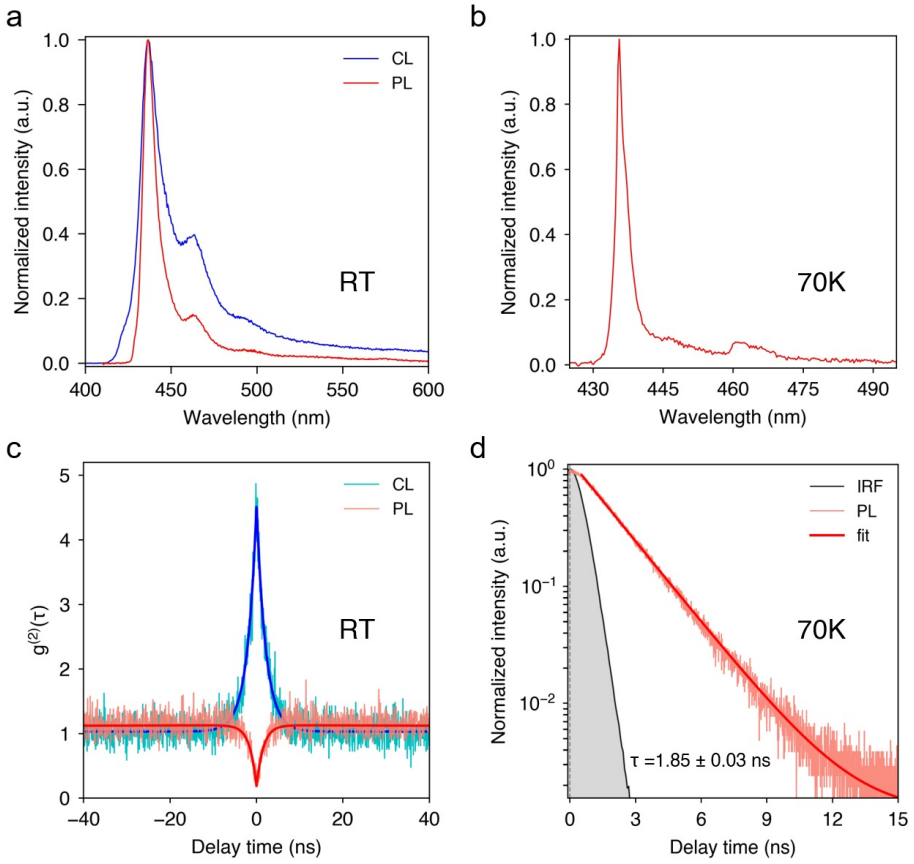

Figure 4.2: *Optical properties of blue emitters fabricated by electron irradiation of hBN. (a) CL (blue) and PL (red) spectra collected at room temperature. (b) Cryogenic PL spectrum collected at 70 K. (c) Second-order CL autocorrelation function (blue) of an ensemble, and a PL autocorrelation function (red) from a single emitter, measured at room temperature. The intensity at zero delay time is 4.53±0.03 and 0.19±0.08, respectively. Background correction was not employed in either case. A lifetime of 2.11±0.03 ns was deduced from a single exponential fit of the CL $g^{(2)}$ curve. (d) PL decay curve obtained using a 405 nm pulsed laser, yielding an excited state lifetime of 1.85±0.03 ns. The excitation pulse width and repetition rate were 45 ps and 20 MHz, respectively. A 430 nm longpass filter was used for the PL measurement in (a), and a 60 nm bandpass filter centered on 460 nm was used in (b-d).*

electron beam is shown in red in Figure 4.2(c). It shows antibunching with a $g^{(2)}(\tau)$ value of 0.19 $\pm$ 0.08. A PL decay measurement that was obtained at 70 K and fitted with a single exponential function, yielding an excited state lifetime of 1.85 ns, consistent with the mean

value of $\sim$ 2.1 ns obtained from the CL autocorrelation function of an ensemble of these emitters. The optical measurements in Figure 4.2 summarise the basic properties of the blue emitters generated by electron irradiation of hBN, and illustrate the non-classical nature of photon emission from ensembles and individual emitters excited by electrons and photons, respectively. For completeness the effect of the electron beam current on the $g^{(2)}(0)$ value was also verified to follow the typical trend of decreasing bunching with increasing electron beam current. These results are illustrated in the Figure 4.3 which follow the expected behaviour. The low currents used in these measurements ensure that the incoming electrons are spaced such that the CL emission is detected in distinct photon packets. Increased currents reduce this spacing between excitation and emission and as such increase the possibility of non distinct photon packets at 0 delay time ($g^{(2)}(0)$), ultimately reducing the bunching curves. Characterisation of quantum emitters by both CL and PL is important for future applications of hBN quantum emitters in nanophotonics and nanoplasmonics, where CL and electron beam techniques play an increasingly important role.[231]

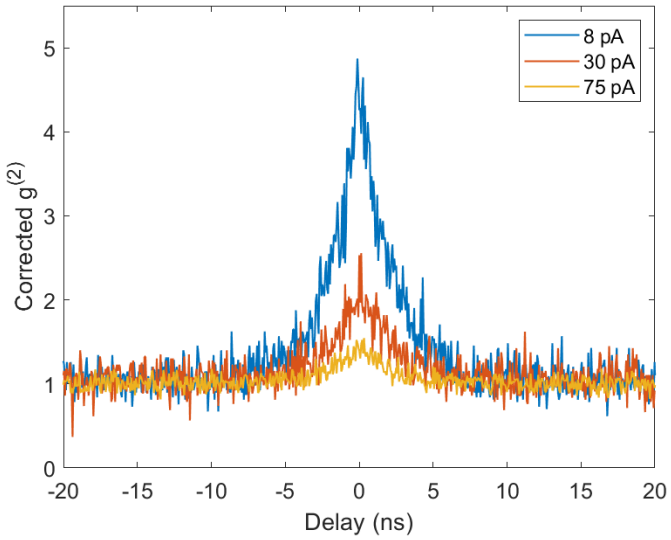

Figure 4.3: *Second-order CL autocorrelation data of an SPE ensemble measured with varying beam currents. A 5 keV beam was scanned over an area of 150 x 130 nm containing an SPE ensemble with currents of 8.0 pA, 30 pA and 75 pA. The emission was filtered using a 460±60 nm band-pass filter.*

Now turning to dynamics of the blue emitter fabrication process. Figure 4.4(a) and (b) shows CL and PL maps of a 3x3 spot array fabricated in an annealed Type II hBN flake as a function of electron beam exposure time. The electron dose was varied from 6.2×10^9 to 1.6×10^{12}, as is shown in the legend of Figure 4.4(c). The CL map was generated by integrating the CL intensity between 430 and 480 nm, and the PL map was acquired from the same region using a 460±30 nm bandpass filter. Both maps show enhanced fluorescence intensity at each spot irradiated by the electron beam. Figure 4.4(c) shows PL spectra recorded from the nine spots, and the integrated PL intensity is plotted as a function of electron dose in Figure 4.4(d). The PL intensity scales linearly with electron dose, over the range used in the experiment. Notably, such controlled, dose-dependent generation has not been demonstrated previously for quantum emitters in hBN.

The analysis in Figure 4.4(d) was performed using PL spectra produced using a sub-bandgap excitation source, and that the CL signal is not appropriate for this analysis. In CL, carriers are excited across the bandgap, recombination of electron-hole pairs is a competitive process and CL intensity therefore does not, in general, scale linearly with defect concentration.[232] It is emphasized that the data in Figure 4.4 were acquired from hBN that was annealed at 1000 °C before electron beam processing, and that no additional annealing, or other processing was performed after electron irradiation. The linear dependence on electron dose seen in Figure 4.4(d) suggests that the blue emitter generation rate is not rate-limited by diffusive mass transport through the hBN lattice, as is discussed below. The dose dependence and general reproducibility of the method within a flake also suggest that the defects are abundant and distributed relatively uniformly throughout the hBN lattice.

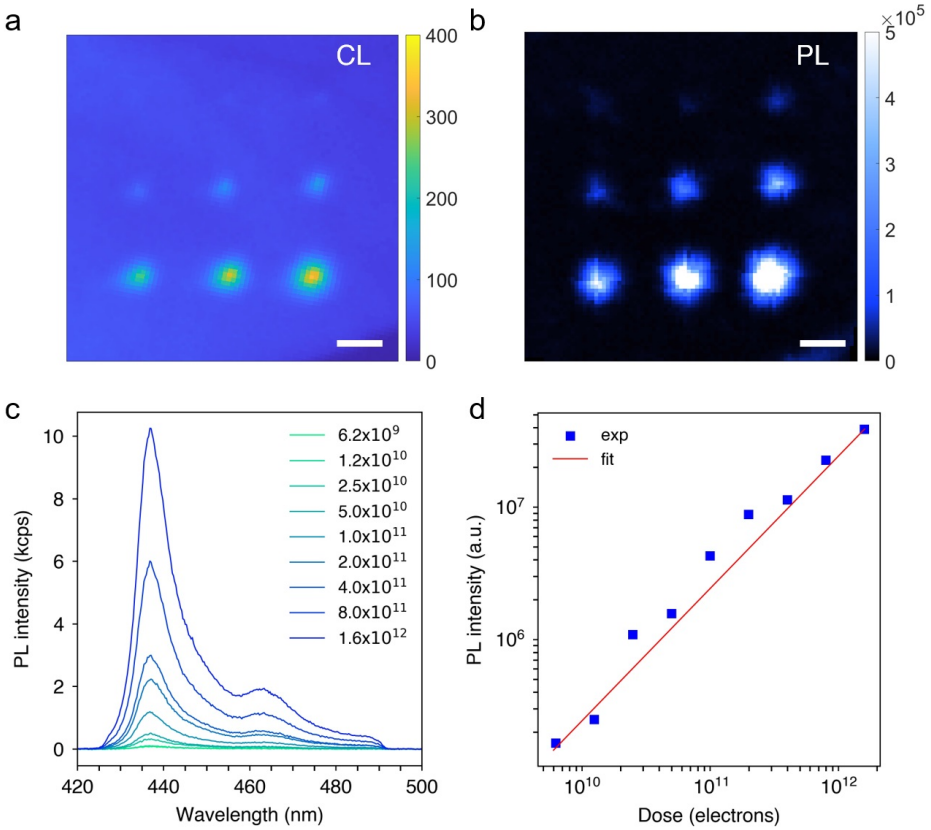

Figure 4.4: *Dynamics of the emitter fabrication process – emission intensity versus electron dose. (a,b) CL and PL maps of a 3x3 emitter array generated using a 1 nA stationary electron beam as a function of exposure time. From top left to bottom right, the irradiation times are 1, 2, 4, 8, 16, 32, 64, 128 and 256 s. The CL map was extracted from a hyperspectral map by integrating the CL intensity in the spectral range 430 - 480 nm. Intensities are plotted as photon counts per second. The scale bars represent 2 µm. (c) PL spectra obtained from the nine spots seen in the maps. The legend specifies the electron dose used to generate each spot. (d) PL intensity versus electron dose obtained by integrating the spectra in (c).*

To further demonstrate the deterministic nature of the emitter fabrication process, a 4×3 array of blue emitters was patterned on an annealed Type I flake using a relatively low electron beam dose of 1.2×10^{10} electrons per spot. A PL map of the array is shown in Figure 4.5(a) with the electron irradiated spots highlighted. Brighter PL spots can be seen at these locations with figure 4.5(b) showing the $g^{(2)}(0)$ for each numbered spot. Of these, 4 have a $g^{(2)}(0)$ value below 0.5, resulting in an SPE fabrication yield of 33 % before background correction. Although the

remaining spots cannot be deemed as single emitters, all 12 spots show antibunching. Second order autocorrelation functions of the 12 spots can be seen in Figure A.2. The saturation behavior of a representative SPE is shown in Figure 4.5(c), demonstrating a saturation emission rate of 400 kHz at the detector at an excitation power of 2.6 mW.

Note that the emitter generation process is stochastic and spatial resolution is limited by the electron beam diameter and electron straggle in hBN flakes and the underlying substrate. It is also clear to see other bright spots corresponding to emitters likely created due to SEM imaging during sample positioning and possible effects from back-scattered electrons.

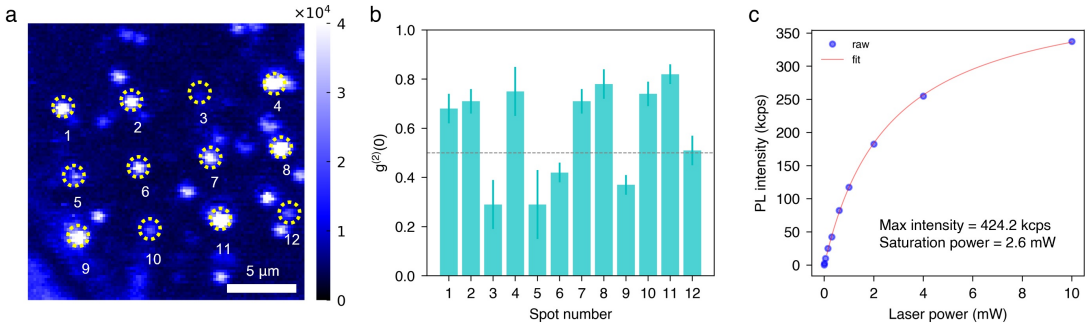

Figure 4.5: *Confocal maps of a patterned array of blue emitters with $g^{(2)}(0)$ and saturation data. (a) Confocal PL map of the patterned array with irradiation positions circled and numbered. (b) Chart of $g^{(2)}(0)$ values for each emitter in (a). The dotted line signifies a $g^{(2)}(0) = 0.5$ indicative of isolated single emitters. (c) Saturation data from a single blue emitter in (a).*

To elucidate the blue emitter generation process further, the processes are studied using hBN samples that were grown by two methods, and optionally annealed before electron irradiation. The function of the pre-annealing treatment is demonstrated in Figure 4.6 by CL spectra from Type I, and Type II hBN that were irradiated in either their as-grown state (black lines) or after annealing (red curves). The high energy peak at 216 nm is the near-bandgap emission of hBN,[115] and the starred peak at 432 nm is the corresponding second order peak. The next prominent feature in the spectra is a strong, narrow mid-near UV emission at 305 nm (4.1 eV) – the ZPL of a well-documented defect[153,154,223,224] that has been ascribed to carbon dimers in the literature,[221,222,157,158] and associated TO phonon replicas at 320 nm (3.9 eV) and 334 nm

(3.7 eV). A third, less intense phonon replica is seen as a shoulder at 351 nm (3.5 eV). The last peak of interest in the spectra is the blue emission generated by electron irradiation with a ZPL at 436 nm (2.8 eV),[161,160] which is enlarged in the panels on the right-hand side of Figure 4.6.

Flakes exfoliated from Type I hBN (grown by the HPHT method) were found to exhibit a strong near band edge emission, and to fall into two general categories, designated Type Ia and Type Ib in Figure 4.6(a,b). Type Ia flakes do not show the 305 nm UV emission (and the associated phonon sideband), but instead show broad emissions centered on 259, 299 and 350 nm. Type Ib, flakes are characterised by the 305 nm UV emission (and the associated phonon sideband). Such differences between fluorescence spectra of Type I hBN have been observed previously and attributed tentatively to intrinsic defects,[116] and variations in carbon and oxygen content.[154]

A strong correlation is observed, illustrated by the CL spectra in Figure 4.6, between the 305 nm UV emission ($\sim$ 4.1 eV) and the efficacy of electron beam irradiation at generating the 436 nm blue emitters. Specifically, the irradiation technique is ineffective in flakes exfoliated from Type Ia hBN which do not show the 305 nm UV emission, and highly effective in Type Ib flakes which do show the UV emission. In Type Ia flakes, the electron beam changes the intensities of broad emissions centered on $\sim$ 259, 299 and 350 nm, but it is very ineffective at generating the 436 nm blue emission (Figure 4.6(a)). Conversely, in Type Ib flakes, the electron beam does consistently generate the 436 nm emission, as is illustrated by Figure 4.6(b). This correlation provides a strong indication that the 436 nm blue emitters are also associated with carbon, consistent with recent modelling studies.[221,158]

The variability between Type Ia and Ib samples (which were exfoliated from a single crystal of hBN), can be suppressed by the 1000 °C annealing treatment performed in N_2 prior to electron exposure. The vast majority of annealed Type I flakes are characterised by CL spectra dominated by the 305 nm UV emission. Electron irradiation generated the 436 nm emission consistently and reliably in these flakes, as is illustrated in Figure 4.6(c). Note that the 216 nm near-bandgap CL emission is very weak in annealed Type I flakes.

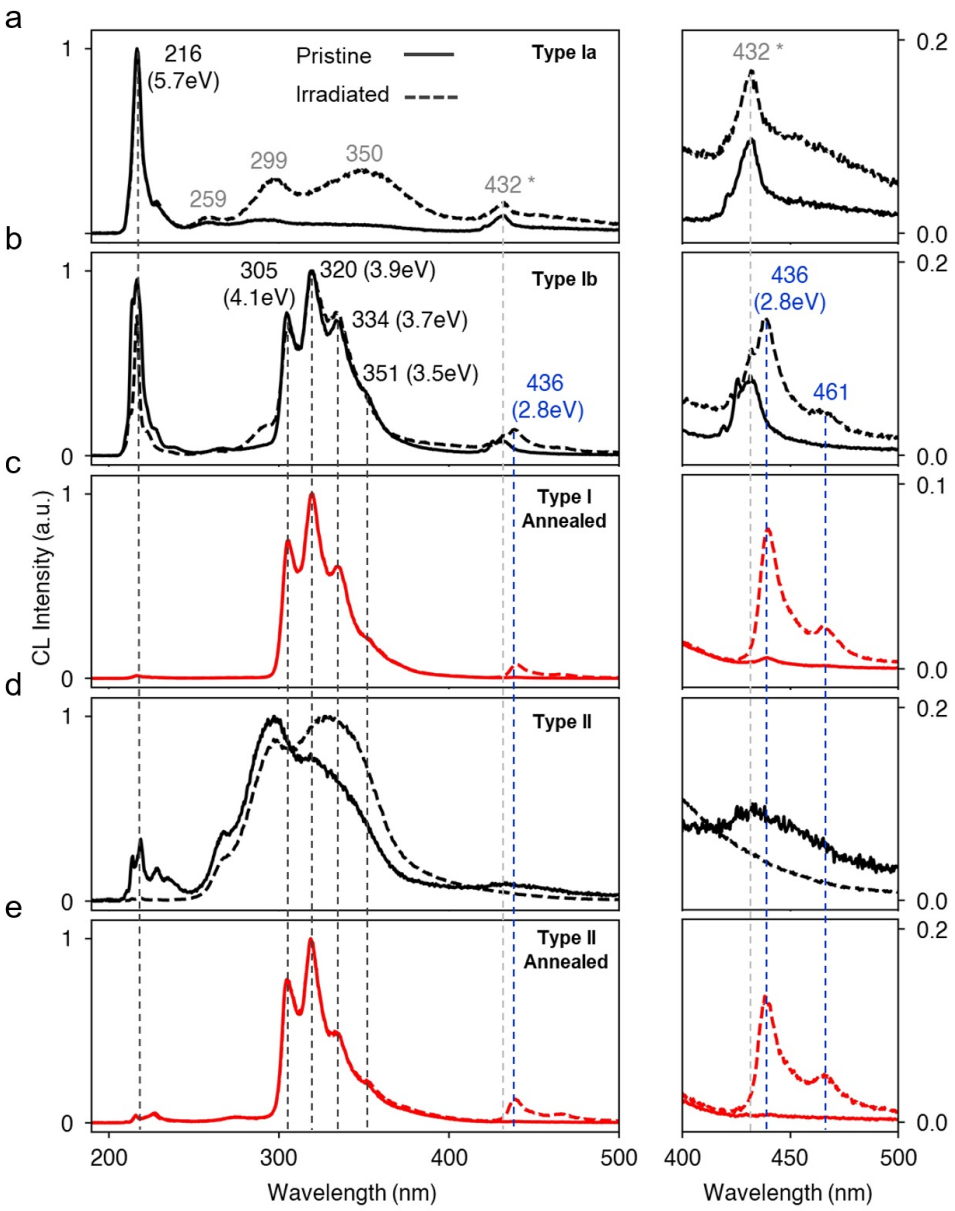

Figure 4.6: *CL characterisation of hBN before and after processing by an electron beam. (a - e) Normalised CL spectra of five hBN samples before (solid lines) and after (dashed lines) electron beam processing. Black and red curves indicate samples that were as-grown and annealed at 1000 °C, respectively. Peak positions are indicated on the plots in nanometres and electronvolts (eV). The asterisk indicates a second order peak at 432 nm. The right panel is a close-up of the spectral range containing the 436 nm blue emission (and a phonon replica at 461 nm) generated by electron irradiation of hBN samples that show a sharp UV emission at 305 nm (and associated phonon replicas at 320, 334 and 351 nm).*

Similar behaviour was observed in commercially-sourced Type II hBN. Typical CL spectra obtained from flakes of this material before and after electron irradiation are shown in Figure 4.6(d). In as-grown samples, the spectra do not show the sharp 305 nm UV emission, and the electron irradiation treatment is consistently ineffective at generating the 436 nm blue emission. However, as is illustrated by Figure 4.6(e), the 1000 °C annealing treatment is again highly effective at producing the 305 nm emission, and it greatly enhances the efficacy of electron irradiation at generating the 436 nm blue emitters.

Now moving to a discussion on potential mechanisms behind the annealing and electron irradiation treatments. In general, annealing can create new defects, cause the diffusion and restructuring of existing defects, introduce impurities/dopants, and shift the Fermi level which can alter the charge states of existing defects. Note that the annealing treatment was ineffective at generating the 305 nm UV emission in a small subset of Type I hBN flakes (and electron beam irradiation was ineffective at generating the 436 nm blue emitters in this small subset of flakes both before and after annealing). These flakes are characterised by CL spectra dominated by an intense near-bandgap emission both before and after annealing, which is an indicator of highly pristine, high quality hBN.[115,116,233] Therefore it can be concluded that the primary function of the annealing treatment is not to introduce new defects/impurities, but rather to restructure and activate existing defects, which likely involve impurity atoms that were distributed unevenly in the as-grown hBN crystal used for exfoliation.

Returning to flakes that were annealed "successfully", yielding CL spectra dominated by the 305 nm UV emission (Figure 4.6 (c) and (e)). The annealing increased not only the flake sensitivity to the electron beam emitter fabrication process, but also uniformity within the flakes – meaning that annealing increased the consistency of a linear relationship between electron dose and intensity of the 436 nm blue emission (illustrated by Figure 4.4 (d)). This implies that annealing homogenised the concentrations of defects responsible for the 305 nm (4.1 eV) UV emission. In the literature, this UV emission has been associated with carbon impurities in hBN,[154,225] and recent modelling studies suggest the C_BC_N carbon dimer as the underlying atomic structure.[221,222,157,158] Hence, based on this picture, the results indicate that the annealing

treatment gives rise to the formation of C_BC_N dimers in carbon-containing hBN flakes.

Next, focusing on electron irradiation. Energetic electrons can generate new defects and restructure existing defects. At the electron energies employed here, the primary mechanism is not the displacement of nuclei via momentum transfer (i.e., knock-on)[39,234] but instead bond-breaking caused by electron-electron collisions, and transport assisted by drift of ionised atoms in the presence of electric fields generated in a dielectric by an electron beam.[42,179] Bearing this in mind, with a focus on the observation that electron irradiation is effective at generating the 436 nm blue emitters only in hBN flakes with CL spectra characterised by the 305 nm UV emission. Specifically, the possibility that the blue emitters are generated purely because new defects are created by the electron beam is excluded. Whilst defect creation can occur, a clear prerequisite for blue emitter generation is presence of the UV defects, and it is reasonable to suggest that these defects are modified by the electron beam. Note also that the PL intensity of the 436 nm emission scales linearly with electron dose, over at least two orders of magnitude (10^{10} to 10^{12} electrons, see Figure 4.4(d), indicating that atomic drift/diffusion through the hBN lattice is not the rate-limiting process in annealed hBN flakes. Instead, two possibilities are considered – electron irradiation may modify the defect charge state or atomic structure. The former can proceed directly by electron-induced charge transitions in hBN, or indirectly via band bending[235] caused by electron beam modification of the surface. The latter is the more likely in the light of modelling studies which indicate that the C_BC_N dimer is the source of the 305 nm UV emission, and that calculated PL spectra of isolated and closely-spaced substitutional carbon atoms resemble the 436 nm blue emission.[221,158] Hence, the blue emitters likely form via restructuring of the carbon dimers through a bond breaking-restructuring process initiated by electron impact.

4.4.1 Conclusion

In this chapter, a robust approach for site-specific engineering of blue quantum emitters in hBN was developed. This involves a high temperature anneal, pre-characterisation by CL spectroscopy and an electron irradiation treatment. The fabricated defects emit at 436 nm (2.8

eV) and the ability to generate these blue emitters by an electron beam correlates with the pre-existence of carbon-related defects that emit at 305 nm (4.1 eV). The results improve present understanding of the photophysical properties of hBN, and on the effects of electron irradiation on defects in hBN. The blue emitter fabrication method is appealing for both fundamental studies of quantum emitters in hBN and for their integration in photonic nanostructures – it has high spatial resolution, generates a specific defect species characterised by an emission wavelength of 436 nm, and the emission intensity scales linearly with electron dose.

5

Manipulating the Charge State of Spin Defects in Hexagonal Boron Nitride

5.1 Preamble

Negatively charged boron vacancies (V_B^-) in hBN have recently gained interest as spin defects for quantum information processing and quantum sensing by a layered material. However, the boron vacancy can exist in a number of charge states in the hBN lattice, but only the -1 state has spin-dependent PL and acts as a spin-photon interface. In this chapter the charge state switching of V_B defects under laser and electron beam excitation is investigated. A deterministic, reversible switching between the -1 and 0 states ($V_B^- \rightleftharpoons V_B^0 + e^-$) is demonstrated, occurring at rates controlled by excess electrons or holes injected into hBN by a layered heterostructure

device. This work provides a means to monitor and manipulate the V_B charge state, and to stabilise the -1 state which is a prerequisite for optical spin manipulation and readout of the defect. This chapter includes text and figures from the peer-reviewed journal article; Gale, A. et al, *Manipulating the charge state of spin defects in hexagonal boron nitride*, Nano Letters, 2023.[4]

5.2 Introduction

Optically-active spin defects in wide bandgap materials hold promise as qubits for quantum information processing, and quantum sensing with nano-scale spatial resolution. Examples include the nitrogen-vacancy (NV^-) and silicon-vacancy (SiV^-) centers in diamond, which have been used to achieve coherent control and manipulation of spin states .[193,236,237,238]

hBN has recently emerged as a compelling wide bandgap van der Waals host of optically-active spin defects.[142,239,240,130,241,150,149] The most-studied spin defect in hBN is $V_B{}^-$, a negatively-charged boron monovacancy with a ground state electron spin of 1.[142,220,144] The ground state electron spin can be initialised optically, manipulated by a microwave field, and read out using a spin-dependent PL emission at $\sim$ 800 nm (i.e., using the ODMR technique). However, like other spin defects in wide bandgap materials[27,242,243], the V_B defect can exist in a number of charge states.[244] It is therefore important to understand V_B charge state dynamics and stability during optical excitation, and in environments encountered in devices and sensing applications. In mature systems such as the NV center in diamond, charge state control has been achieved by various methods that include chemical surface termination[245], optical manipulation[246,174] and the use of electrical devices.[247] In the case of V_B centers such studies are, however, challenging because, only the -1 state of V_B has a known characteristic PL emission that can be monitored experimentally.

This work utilises optical excitation and concurrent electron beam irradiation to demonstrate switching as well as reversible, deterministic manipulation of the charge states of V_B defects in hBN. Moreover, a layered heterostructure device is utilised to show that the switching is between the -1 and 0 states (i.e., $V_B^- \rightleftharpoons V_B^0 + e^-$), and provide a means to stabilize the -1 state which

is a pre-requisite for the defect to act as a spin-photon interface. These results provide insights into V_B charge state dynamics during optical excitation, and in external environments such as electric fields and ionizing radiation that are encountered in devices and in real-world sensing applications.

5.3 Methods

5.3.1 Sample Preparation

hBN flakes were mechanically exfoliated with scotch tape onto coverslips coated with ITO to minimise charging effects in the SEM. Prior to exfoliation, substrates were sonicated in acetone and isopropanol (30 min each), dried under flowing nitrogen, and cleaned for 10 min using a commercial UV ozone unit (ProCleaner Plus, Bioforce Nanosciences Inc.). Post exfoliation, substrates with hBN flakes were annealed on a hotplate at 500 °C for 1 hour.

5.3.2 Ion Irradiation

To generate boron vacancies, exfoliated hBN flakes were irradiated by 30 keV nitrogen ions using a ThermoFisher Helios G4 dual-beam. For the hBN flake in Figure 5.2, an area of 25 $\times$ 25µm was irradiated using a beam current of 1.5 pA, yielding a fluence of 1.5×10^{14} ions/cm^2. For the device in Fig 5.3, the entire hBN flake was irradiated using a beam current of 59.5 pA to a a fluence of 1.5×10^{14} ions/cm^2.

5.3.3 Scanning Electron Microscope and Integrated Photoluminescence Setup

The integrated optical and electron microscopy setup shown in Figure 5.1 utilises the electron column of an FEI DB235 dual-beam FIB/SEM instrument, and a modified Delmic SECOM CL system with additional scanning PL capabilities.[248,249] The Delmic system incorporates an oil objective (Nikon 60 $\times$ Plan APO 1.4 NA) with vacuum-compatible oil on a piezo-controlled 3-axis stage to align and focus the laser spot. A coverslip used to support the sample is mounted on an independently controlled 2-axis piezo stage to allow for sample positioning. An optically-transparent quartz window maintains vacuum in the chamber. The customised optical

setup includes a 45 ° silver mirror below the window to direct the optical pathway from vertical to horizontal. The custom-built laser scanning PL setup includes a fibre-coupled continuous wave 532 nm excitation laser (CNI MLL-U-532) for excitation and a 532 nm dichroic beamsplitter. A scanning mirror (Newport FSM-300) and 4f system provides full scanning capabilities. A 568 nm long pass filter is used before a multimode fiber and either an avalanche photodiode (Excelitas SPCM-AQRH) is used for PL mapping or a spectrometer (Andor Kymera 328i) with a 500 lines/mm grating for spectral measurements. Individual spectra were taken using a laser power of 400 µW and a 10 s integration time. As this system has been modified in our own laboratory for such purposes, some further description and analysis of the system is shown in the Appendix, Section A.4.

Electron irradiation was performed using a 5 keV electron beam. In order to achieve a coincident laser and electron beam spot, PL maps were taken and compared to the SEM image of the same area, with spatial features utilised for alignment. For the experiments in Figure 5.2, the electron beam spot was defocused to ensure the electron flux was constant across the area excited by the laser. The electron flux was calculated from the beam current, and the electron beam area which was measured from carbon deposits made on an unused section of the ITO substrate.

5.3.4 Optically Detected Magnetic Resonance

For ODMR measurements an ex-situ setup on an optical table was utilized. A 532 nm CW laser was used for excitation and a copper wire with a diameter of 30 μm was placed near the sample. Microwave signal from a generator (Anapico aspin) was amplified (minicircuits, ZHL-16W-43-S+) and directed through the wire. The microwave frequency was swept between 3 and 4 GHz and the PL emission was recorded using an avalanche photodiode (Excelitas SPCM-AQRH) with the microwave on and off.

5.4 Results and Discussion

A schematic of the experimental setup is shown in Figure 5.1(a) – a laser scanning PL system incorporated in an SEM. The setup enables coincident irradiation of a sample by an electron beam (yellow) and a laser (green), during PL (red) analysis. Samples used in this work are hBN flakes that had been irradiated by 30 keV nitrogen ions to fabricate V_B defects. A schematic illustration of a V_B defect in a single sheet of hBN is shown in Figure 5.1(b). In the -1 charge state, $V_B{}^-$ defects are characterized by a broad PL emission at $\sim$ 800 nm (blue spectrum in Figure 5.1(c)) and a zero-field ground state splitting of $\sim$ 3.5 GHz between the $m_s = 0$ and $m_s = \pm 1$ spin states (Fig. 5.1(d)).[142]

To begin, the effects of a 5 keV electron beam on PL from an ensemble of $V_B{}^-$ defects excited by a 532 nm laser is investigated. Firstly, it is clear that in the absence of the laser, electron irradiation did not generate any detectable $V_B{}^-$ CL, as is shown by the red spectrum in Figure 5.1(c). The electrons do, however, cause quenching of the $V_B{}^-$ PL signal, as is illustrated in Figure 5.2(a) by six PL spectra acquired versus the flux ($e^-/cm^2/s$) of the electron beam. The spectra are normalised to the PL spectrum measured at zero flux (i.e., in the absence of the electron beam). The $V_B{}^-$ PL intensity decreases with electron flux, whilst the spectral shape remains unchanged. Moreover, the quenching is reversible, as is demonstrated in Figure 5.2(b) by the following two plots. The first, in red, is the $V_B{}^-$ PL intensity plotted versus electron flux, normalised to the PL intensity at zero flux. The plot shows that the quenching is relatively weak ($\sim 10\%$) when the electron flux is low ($\sim 10^{15}$ $e^-/cm^2/s$), and that it increases to over 30% as the electron flux is increased to $\sim 3 \times 10^{16}$ $e^-/cm^2/s$. The second plot in Figure 5.2(b) is the ratio of PL intensity measured before and after irradiation by the electron beam, at each electron flux (blue). It is constant at ~ 1, showing that the quenching is not permanent – i.e., the PL intensity recovers when the electron beam is turned off, at all values of electron flux used in the experiment.

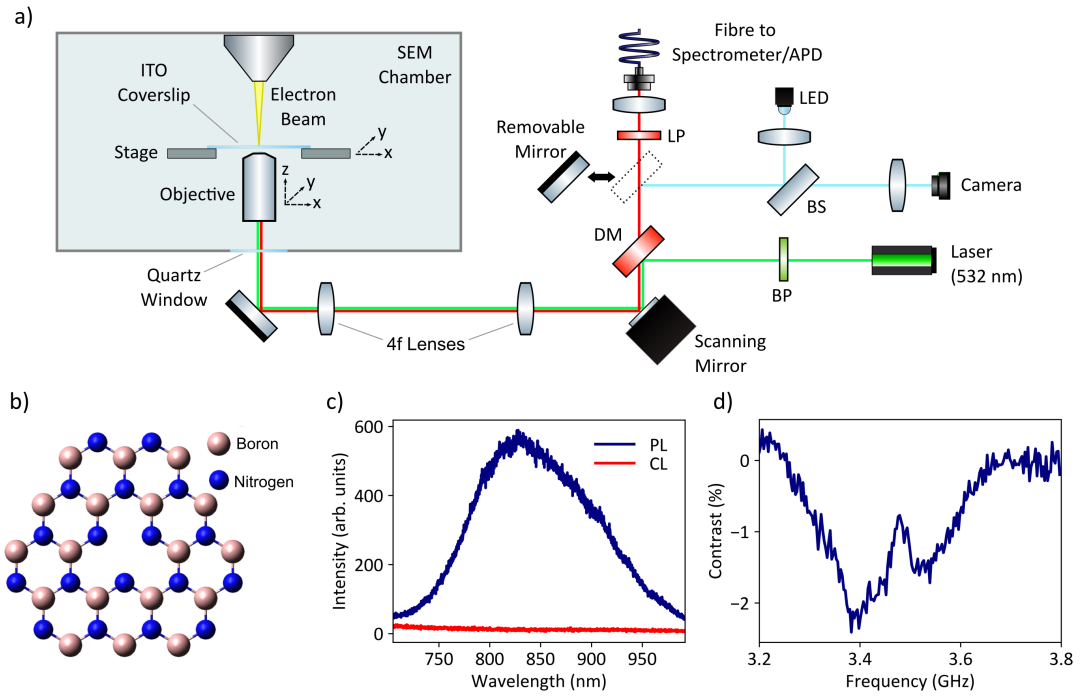

Figure 5.1: *Overview of the experimental setup and V_B defects in hBN. (a) Schematic illustration of the experimental setup. A 5 keV electron beam (yellow) irradiates hBN supported by a coverslip coated with indium tin oxide (ITO). An objective delivers a laser (green) that is coincident with the electron beam, and collects light (red) emitted by hBN. BP = Band Pass Filter, BS = Beam Splitter, DM = Dichroic Mirror, LP = Long Pass Filter, APD = Avalanche Photodiode. (b) Ball and stick model of the V_B defect in a monolayer of hBN. (c) Representative PL spectrum (blue) from an ensemble of V_B^- defects excited by a 532 nm laser in the absence of the electron beam. Also shown is a CL spectrum (red) acquired from the same region in the absence of laser excitation (electron beam energy = 5 keV, electron flux = 2.9×10^{16} $e^-/cm^2/s$). (d) Representative ODMR spectrum from an ensemble of V_B^- defects collected ex-situ, outside the electron microscope.*

The effect of the PL excitation laser power on the PL quenching caused by the electron beam was also studied. Figure 5.2(c) shows a plot of the V_B^- PL intensity as a function of laser power (red). In this measurement, the sample was irradiated by a 5 keV electron beam (flux=7.3×10^{15} $e^-/cm^2/s$), and the plotted PL intensity is normalised to that measured at each laser power in the absence of the electron beam. The quenching caused by the electron beam is inhibited by

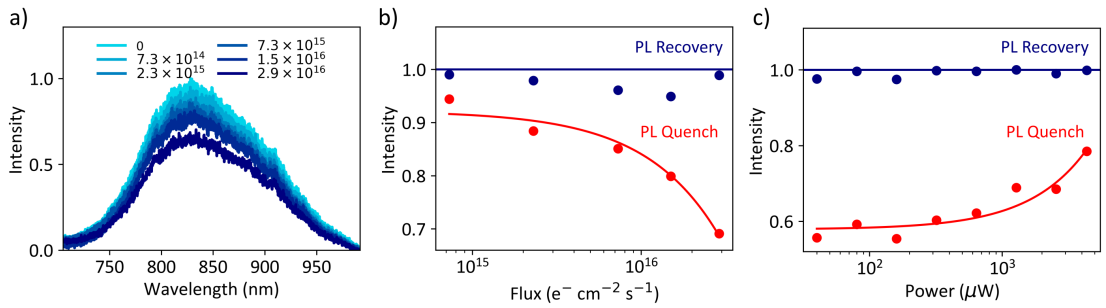

Figure 5.2: *Charge state manipulation of V_B defects by electron beam and laser irradiation. (a) PL spectra of a V_B^- ensemble acquired as a function of electron beam flux (the fluxes used are shown in the legend in units of $e^-/cm^2/s$). The spectra are normalised to the spectrum measured at zero flux (i.e., in the absence of the electron beam). They demonstrate quenching of the V_B^- PL emission by a 5 keV electron beam. (b) normalised V_B^- PL intensity plotted as a function of electron flux (red; laser power = 400 μW). The PL intensity is normalised to that at zero flux. Also shown is the ratio of PL intensity measured before and after electron irradiation at each electron flux (blue), demonstrating that the PL intensity recovers when the electron beam is turned off – i.e., the PL quenching caused by the electron beam is reversible. (c) normalised V_B^- PL intensity plotted as a function of laser power (red). In this measurement, the sample was co-irradiated by an electron beam with a flux of* 7.3×10^{15} $e^-/cm^2/s$. *The PL intensity at each laser power is normalised to that measured at zero flux. Also shown is the ratio of PL intensity measured before and after electron irradiation at each laser power (blue), demonstrating that the PL quenching caused by the electrons is reversible. The circles and lines in (b) and (c) are experimental data and guides to the eye, respectively.*

the laser – for example, at a relatively low laser power of $\sim 10^2$ μW, the electron beam reduced the PL intensity by $\sim 40\%$, whilst at a higher laser power of $\sim 4 \times 10^3$ μW the same electron beam reduced the PL intensity by $\sim 20\%$. For completeness, Figure 5.2(c) shows a plot of the ratio of PL intensity measured at each laser power before and after electron irradiation. The plot confirms that the PL quenching caused by electrons is reversible at all laser powers employed in these experiments.

To summarize, the electron beam causes quenching of V_B^- PL intensity by an amount that scales with electron flux (Fig. 5.2(b)) and reciprocal power of the PL excitation laser (Fig. 5.2(c)). The quenching is reversible (i.e., the PL intensity is equal before and after electron beam exposure) at all laser powers and electron fluxes investigated in this work. The electron and laser beams therefore drive two competing, rate-limited processes that quench and recover the V_B^- PL emission, respectively. The PL quenching rate scales with electron flux, the PL recovery rate with laser power, and the steady state PL intensity is determined by these two parameters. The quenching and recovery is attributed to ionization of V_B^- centers and electron back transfer to V_B^0 defects, as is discussed below. It is also noted that the quenching magnitude was observed to vary between different flakes of hBN. The flakes vary in their thickness, and also likely in the densities of both V_B defects and charge traps in the surrounding environment. The observed variations in quenching are therefore expected and consistent, qualitatively, with a charge transfer mechanism.

A layered heterostructure device shown schematically in Figure 5.3(a) was used to inject carriers into hBN and investigate their effects on the PL quenching effect. The device consists of gold contacts and a pair of few-layer graphene (FLG) electrodes that encapsulate an 80 nm flake of hBN. An optical image is shown in Figure 5.3(b) with coloured lines indicating the positions of the hBN and FLG layers. The top FLG electrode was grounded, and a bias voltage was applied to the bottom electrode. The device was loaded into the SEM and irradiated from the top by a 5 keV electron beam and from the bottom by a 532 nm PL excitation laser. The 5 keV electrons penetrate through the FLG/hBN/FLG device, into the substrate, as is shown in Figure 5.3(c) by a plot of $\frac{\partial E}{\partial z}$ versus depth (z). $\frac{\partial E}{\partial z}$ was simulated using the Monte Carlo package CASINO.[250] It is the mean energy lost by each electron per unit distance travelled through the sample. The area under the curve (E) is the total energy deposited into the sample per electron, and it falls34 off to zero at a depth of $\sim$350 nm, the maximum penetration range of the electron beam. For the flake thicknesses in this work the energy was sufficient to penetrate fully through the hBN. The area irradiated by the laser was fully surrounded by a region of electron flux through the use of a defocused electron beam.

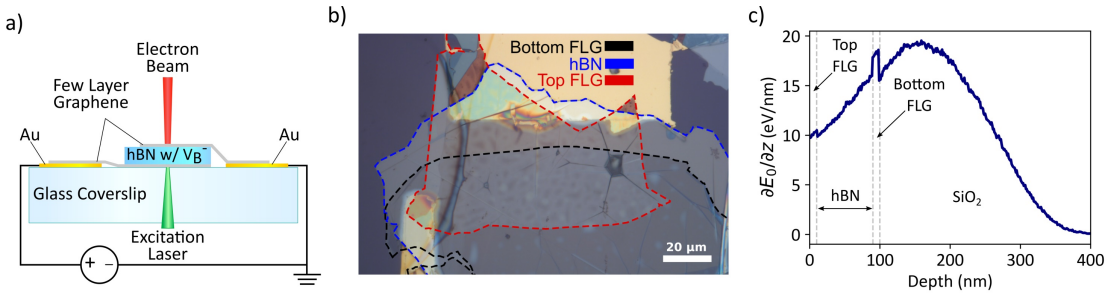

Figure 5.3: *Device overview and simulated depth distribution of the 5 keV electron beam. (a) Cross-sectional schematic of a device comprised of an 80 nm flake of hBN encapsulated by 10 nm FLG electrodes. The device is supported by a glass coverslip substrate. The hBN is excited by a 532 nm laser from the bottom, and irradiated by a 5 keV electron beam from the top. (b) Optical micrograph of the device. Coloured dashed lines outline the positions of the hBN and FLG layers. (c) Simulated depth distribution of the energy loss rate $(\partial E/\partial z)$ of a 5 keV electron incident on the device. At each depth z, $\partial E/\partial z$ is proportional to the generation rate of electron-hole pairs by a 5 keV electron. The range of 5 keV electrons is ∼350 nm. The vertical lines show FLG interfaces. The top FLG electrode is at the surface, and the bottom electrode is at a depth of 90 nm.*

The device bias modulates the magnitude of the V_B^- PL quenching caused by the electron beam. Specifically, as is shown by the red curve in Figure 5.4(a), application of a positive or a negative bias to the bottom FLG electrode enhances or inhibits the quenching, respectively. In this measurement, the laser power and electron beam flux were both fixed, and only the bias applied to the bottom FLG electrode was varied – for example, at a bias of -6 V, the electron beam reduced the V_B^- PL intensity by $\sim 30\%$, whilst at +6 V, it reduced the PL intensity by $\sim 57\%$. Conversely, in the absence of electron irradiation, the device bias has no effect on the V_B^- PL intensity. This is demonstrated by the blue plot in Figure 5.4(a), which shows that the PL intensity does not change with bias, when measured in the absence of the electron beam. Similarly in Figure 5.4(b) only intensity is affected under electron irradiation with no spectral shift apparent under bias.

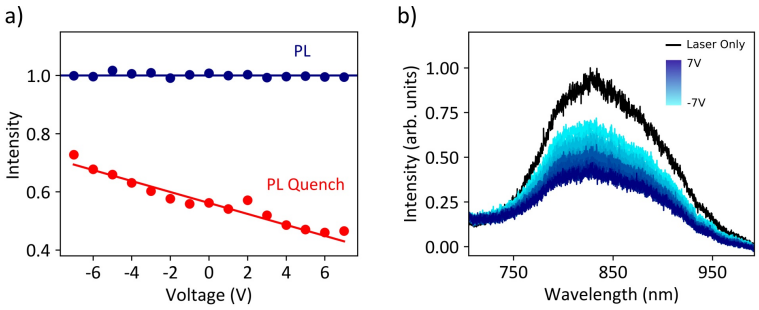

Figure 5.4: *Electrical modulation of the V_B charge state during co-irradiation by a 5 keV electron beam and a laser. (a) Normalised V_B^- PL emission intensity plotted versus bias (red). The PL intensity was measured during irradiation by electrons. The device bias modulates the magnitude of PL quenching caused by the electron beam. Also shown is the PL intensity measured at each bias in the absence of the electron beam (blue), showing that the device bias has no effect on PL intensity in the absence of electron irradiation. The circles and lines are experimental data and guides to the eye, respectively. (b) PL spectra of the V_B^- ensemble acquired versus bias (blue-cyan) applied to the bottom FLG electrode during irradiation by the electron beam. The spectra are normalized to the maximum intensity of a reference spectrum acquired at 0 V in the absence of the electron beam (black).*

At this point, the mechanisms behind the V_B^- emission quenching effect must be discussed. Three potential explanations are that the electron beam: (i) restructures the atomic configuration of V_B defects or generates new lattice defects through "electron-beam-damage" mechanisms analogous to those reported in other dielectrics[251], (ii) promotes relaxation of excited V_B^- centers through a nonradiative pathway such as the intersystem crossing[142] responsible for V_B^- ODMR contrast, or (iii) changes the charge state of V_B^- centers. Of the possibilities, these results are consistent only with the latter – specifically, the PL quenching is due to ionization (i.e., $V_B^- \longrightarrow V_B^0$) caused by the electron beam, and the PL recovery is due to a photo-activated electron back-transfer process (i.e., $V_B^0 \longrightarrow V_B^-$) driven by the 532 nm laser. To substantiate this claim, the operation of the device used in Figure 5.3 is considered in detail.

Figure 5.5(a) is a simplified flat band electron energy diagram of the FLG/hBN/FLG heterostructure under zero bias. E_F is the Fermi level; W is the work function of FLG[252]; E_G, E_C and E_V are the hBN bandgap[117], conduction band minimum and valence band maximum;

E_e and E_h are the energy difference between E_F and the hBN conduction and valence band, respectively; and z is distance below the top surface of the hBN layer (i.e., 'depth' in Figure 5.3(c)). Application of a positive or a negative bias voltage to the bottom FLG electrode generates applied electric fields, as is illustrated in Figure 5.5(b).

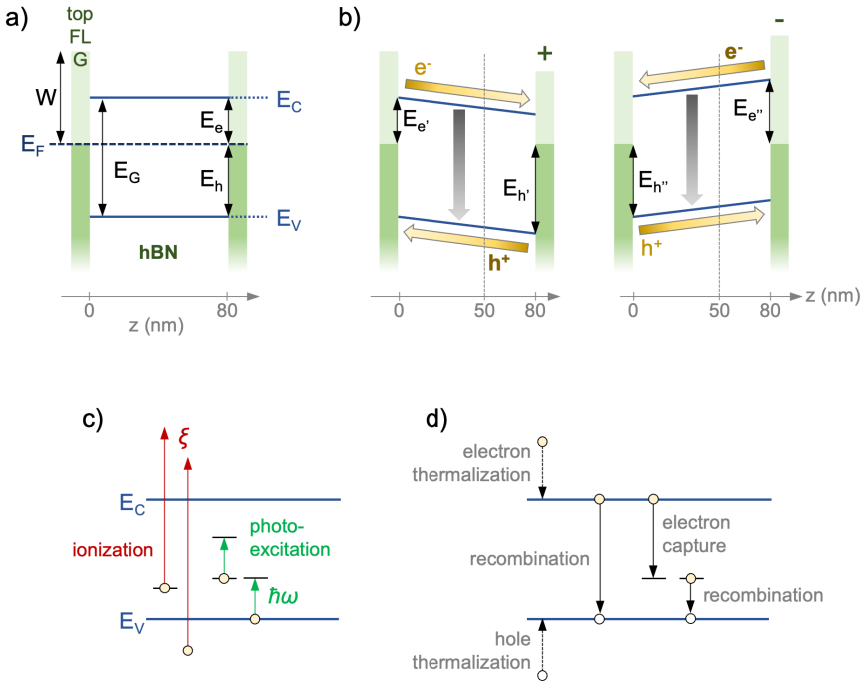

Figure 5.5: *Simplified electron energy diagrams. (a) The device in Figure 5.3 with both electrodes grounded. (b) The device with positive (left) and negative (right) bias applied to the bottom FLG electrode. The yellow arrows indicate the flow directions of carriers in hBN. The gray arrows represent electron-hole recombination occurring throughout the hBN layer (Eqn. 5.2), and z is distance below the top FLG electrode. The concentration of V_B defects has a minimum at* $z \approx 0$ *and a maximum at* $z \approx 50$ nm. *(c) Electron-induced ionization (red) of a defect, ionization of an electron in the valence band (red), and photo-excitation (green) of a defect and an electron in the valence band. (d) Examples of transitions that involve free carriers in hBN: thermalization of hot carriers to band edges, recombination of carriers across the bandgap, capture of a thermalized electron at a trap state, recombination of a trapped electron with a hole in the valence band. In c) and d) yellow and white circles represent electrons and holes, respectively.*

It is of note that the bias (of up to ±8 V) had no effect on the V_B^- PL emission in the absence of electron irradiation. The device bias does, however, modulate the V_B^- emission intensity during electron irradiation (Fig. 5.4). The 5 keV electrons act primarily as ionizing radiation. They penetrate the entire FLG/hBN/FLG stack (Fig. 5.3(c)) and excite carriers throughout the heterostructure:

$$\frac{\partial n_{e,h}}{\partial t} = \frac{1}{E_p}\frac{\partial E}{\partial z} f. \tag{5.1}$$

Here, $\frac{\partial n_{e,h}}{\partial t}$ is the generation rate per unit volume of hot carriers (both electrons e and holes h) at depth z in the heterostructure[253], E_p is the mean energy that must be lost by the electron beam to excite one electron-hole pair[254], $\frac{\partial E}{\partial z}$ is the mean energy lost at coordinate z by a beam electron per unit distance travelled through the heterostructure (plotted for the device in Figure 5.3(c)), and f is the electron beam flux.

Throughout the hBN layer, hot electrons and holes $(n_{e,h})$ are excited into the conduction and valence band, respectively, at a rate that is proportional to $\frac{\partial E}{\partial z}$. These carriers cascade and thermalize to the band edges[255] and drift towards the FLG electrodes, as shown by the yellow arrows in Figure 5.5(b) for the case of positive (left) and negative (right) bias applied to the bottom FLG electrode. Ultimately, the carriers either flow to the FLG electrodes, or recombine in the hBN layer. Recombination[255] can be expressed as:

$$\frac{\partial n}{\partial t} = v n_e \sigma n_h, \tag{5.2}$$

where $\frac{\partial n}{\partial t}$ is the carrier rate of change of concentration due to recombination (indicated by gray vertical arrows in Figure 5.5 (b)) at coordinate z in the hBN layer, v is the minority carrier thermal velocity, and σ is the recombination cross-section.

The carriers excited by the electron beam are excited not only in the hBN layer, but also in the FLG electrodes (as per Eqn. 5.1, and the curve of $\frac{\partial E}{\partial z}$ versus z which is plotted in Figure 5.3(c)). These carriers either cascade, thermalize and recombine in FLG, or are injected into hBN over the barriers $E_{e'}$, $E_{h'}$, $E_{e''}$ and $E_{h''}$ shown in Figure 5.5(b). In hBN, the injected carriers thermalize

to the band edges and contribute to the drift and recombination currents, as is indicated by the yellow and gray arrows in Figure 5.5(b). However, critically, these electrons and holes are injected from opposite sides of the hBN layer (at $z = 0$ and 80 nm), and recombine as they flow through the hBN. Consequently, the carrier concentrations vary across the hBN – when the bottom FLG electrode is biased positive (negative), there is a net excess of holes (electrons) at the bottom (top) of the hBN layer. This asymmetry is important because the depth distribution of V_B defects is not uniform, and a net excess of either electrons or holes is therefore supplied to the defects under different bias configurations, as is detailed below.

The depth distribution of V_B defects in hBN is determined by the fabrication method. Here, the defects were generated by 30 keV nitrogen ions. Their concentration has a minimum at the top surface (i.e., at $z = 0$ in Figure 5.5) and a maximum at $z \sim 50$ nm based on Monte Carlo simulations undertaken using the SRIM software package seen in Figure 5.6. Therefore it is clear that the V_B defects are concentrated preferentially near the bottom FLG electrode. Now, when a positive bias is applied to the bottom electrode, holes are injected into hBN from the bottom electrode, and electrons from the top electrode, as is indicated by the yellow arrows in Figure 5.5(b). These carriers recombine as they flow through the hBN layer, yielding a net excess of holes in the V_B-rich region near the bottom FLG electrode. Conversely, a negative bias gives rise to the opposite scenario – electrons are injected into the hBN layer from the bottom electrode and holes from the top electrode. Hence, a net of excess holes (electrons) is supplied to V_B defects when a positive (negative) bias is applied to the bottom FLG electrode, which correlates with the enhancement (inhibition) of PL quenching caused by the electron beam seen in Figure 5.4.

Furthermore, the excess of one carrier type (electrons or holes) near the bottom electrode is exacerbated by the fact that more carriers are exited by 5 keV electrons in the bottom electrode ($80 < z < 90$ nm) than in the top electrode ($-10 < z < 0$ nm), because $\frac{\partial E}{\partial z}$ is greater in the bottom electrode, as is seen in Figure 5.3(c). Specifically, $\frac{\partial E}{\partial z} \sim 10$ eV/nm and ~ 18 eV/nm in the top and bottom FLG electrodes, respectively.

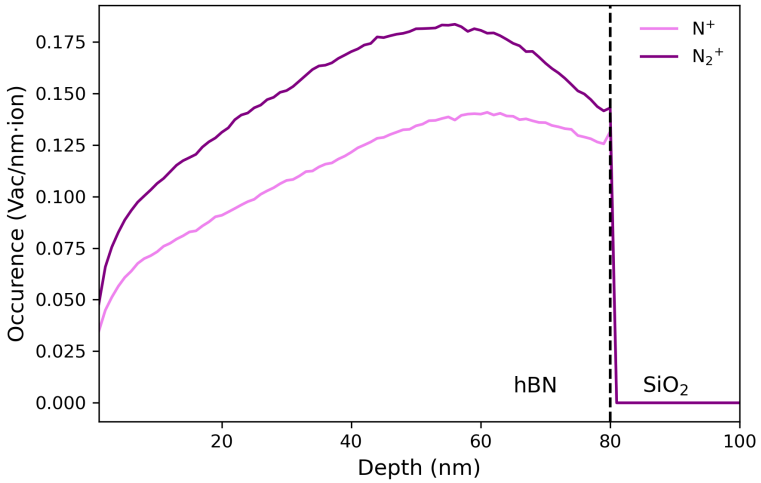

Figure 5.6: *Simulated depth distributions of the boron vacancy generation rates in an 80 nm flake of hBN on an SiO_2 substrate bombarded by 30 keV N^+ and $N_2{}^+$ ions. The distributions show that the V_B concentration has a minimum near the top surface, and a maximum at a depth of* $\sim$ 50 nm.

Based on the above, application of a positive (negative) bias to the bottom electrode results in a net supply of excess holes (electrons) to V_B defects. This correlates with enhancement of the $V_B{}^-$ emission quenching (recovery) driven by the electron (laser) beam. In the presence of excess holes, the quenching is enhanced, consistent with it being caused by ionization ($V_B^- \longrightarrow V_B^0 + e^-$). Conversely, in the presence of excess electrons, the quenching is inhibited, consistent with it being caused by electron back-transfer ($V_B^0 + e^- \longrightarrow V_B^-$).

A consequence and a prediction of the above model is that the modulation caused by the device bias should invert if the bias configuration is reversed. That is, application of a positive (negative) bias to the top FLG electrode should inhibit (enhance) the quenching, respectively. This is the opposite of the behavior seen in Figure 5.4(a), and is indeed what is observed experimentally, as is shown by the positive slope of the guide line in Figure 5.7(a).

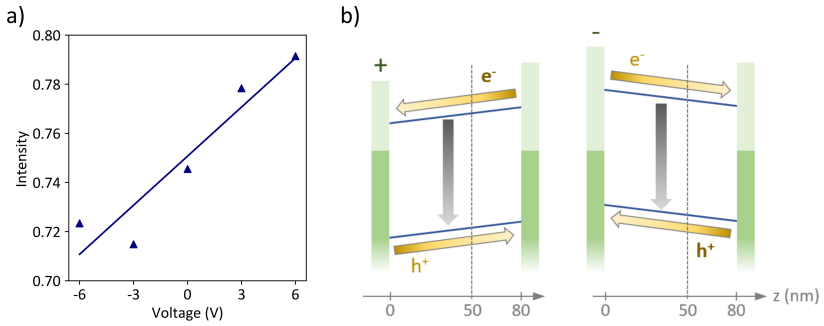

Figure 5.7: *Electrical modulation of the V_B charge state during co-irradiation by an electron beam and a 532 nm laser, performed by applying a bias voltage to the top FLG electrode (the bottom electrode was grounded), reversed from the regular bias. (a) normalised V_B^- PL emission intensity plotted versus bias (triangles; the line is a guide to the eye). (b) Simplified electron energy diagrams of the device with positive (left) and negative (right) bias applied to the top FLG electrode (the bottom electrode is grounded). The yellow arrows indicate the flow directions of carriers in hBN. The gray arrows represent electron-hole recombination occurring throughout the hBN layer, and z is distance below the top FLG electrode.*

These results do not reveal the exact transitions responsible for the charge state switching. However, some discussion is presented here on the various possibilities, including speculation on the most likely pathways. Thus, with reference to Figure 5.5(c) and (d), the following is presented:

$$\mathrm{V_B^-} \rightleftharpoons [\hbar\omega]\xi\mathrm{V_B^0} + \mathrm{e^-}. \tag{5.3}$$

The energy needed to ionize $\mathrm{V_B}^-$ centers (ξ) is provided by 5 keV electrons which can drive all allowed transitions between occupied and unoccupied states in hBN. That is, 5 keV electrons can ionize $\mathrm{V_B}^-$ centers as well as all electron traps and electrons in the valence band of hBN. Excitations that promote electrons into the conduction band dominate (over those that promote electrons into trap states in the bandgap) since the transition probability scales with the density of unoccupied (final) states.[256] Hence, the most likely $\mathrm{V_B}^-$ ionization pathways promote electrons into the conduction band. The electrons thus liberated via the forward reaction in Equation 5.3 then cascade and thermalize to the conduction band minimum and are most likely trapped at

defect states in the bandgap.

The 532 nm laser ($\hbar\omega$) can excite transitions between electronic states separated by up to 2.33 eV. Two examples are shown in green in Figure 5.5(c). Such transitions are likely responsible for the photo-activation that leads to the formation of V_B^- via the reverse reaction in Eqn. 5.3.

Carriers that are excited by the electron beam in the FLG electrodes and injected into hBN cascade and thermalize to the band edges and recombine through pathways such as those shown in Figure 5.5(d). Excess electrons promote V_B^- formation, likely through two mechanisms. The first is capture of thermalized electrons in the conduction band by V_B^0 defects. The second is enhancement of the the laser-driven V_B^- recovery process, by populating electron traps in the vicinity of V_B^0 defects (i.e., by supplying trapped electrons for the laser-driven photo-excitation process in Eqn. 5.3). Similarly, excess holes likely promote V_B^0 formation, via capture of holes in the valence band by V_B^- centers, and via depopulation of electron traps in the vicinity of V_B defects.

Finally, the observation that the device bias (of up to ± 8 V) had no effect on the V_B^- emission in the absence of electron irradiation (blue curve in Figure 5.4(a)) is considered – that is, injection of photo-excited carriers from FLG into hBN appears to not play a role in the observed V_B^- PL emission modulation. This is not surprising since the PL excitation laser promotes V_B^- formation, and whilst electron injection from FLG to hBN is possible, the barriers for hole injection ($E_{h'}$ and $E_{h''}$, shown in Figure 5.5(b)) are greater than the laser energy ($\hbar\omega$), under all bias configurations used in this work. The observation that the electron beam did not generate any detectable V_B^- CL (red spectrum in Figure 5.1(c)) in the absence of laser excitation is also notable. This is not surprising for two reasons: (i) the electrons ionize V_B^- centers, and promote the formation of V_B^0 defects, and (ii) CL excitation proceeds primarily via the conduction band, the recombination process is competitive and the most efficient pathways dominate[257] (as a result, hBN CL spectra are dominated by emissions in the ultraviolet and blue parts of the spectrum.[153,3])

Further insights into the underlying mechanisms can be obtained by measurements of PL quenching and recovery versus the energy of the excitation laser, and time-resolved pump-probe experiments performed using pulsed electron and laser beams. Given the charge dynamics seen for other defects in materials such as diamond, it is likely that these involve millisecond timescales.[104] Such studies may shed light on the charge transfer rate kinetics, charge trap energies, and the roles of one and two photon absorption in the PL recovery process.

5.4.1 Conclusion

In conclusion, these results demonstrate reversible manipulation of the charge state of V_B defects in hBN. V_B^- centres are ionized by 5 keV electrons, and the charge state is recovered by photoexcitation at 532 nm. The two process rates can be modulated by injecting excess electrons or holes into hBN using a layered heterostructure device which can be used to stabilize the -1 state of the defects. The electrical device provides a simple means to maintain V_B defects in the negative charge state, and to improve the robustness of optical applications of V_B^- centers.

6

Conclusion and Outlook

6.1 Conclusion

The chapters in this thesis outline three works focused on the creation, characterisation and manipulation of solid state defects using charged particle microscopy. New methods and systems were developed that led to the creation of solid state defects as well as better understanding the behaviour for a number of defect systems.

In Chapter 3 a method was developed to deterministically create NV^- colour centres in diamond using recoil implantation with gas-phase precursors. The method successfully engineered the colour centres using three nitrogen containing precursors, N_2, NF_3 and NH_3 using a commercially available dual-beam SEM/FIB system. Accurate spatial placement as well as a controlled emission intensity was demonstrated by varying the ion beam position and fluence

respectively. Spectra and ODMR methods were used to characterise and confirm the creation of NV^- emitters. The method removed the requirement for solid-state precursor deposition and wet chemical etching simplifying and expanding the range of possible dopants.

The next chapters focused on single emitters in hBN. In Chapter 4 a novel class of hBN emitter activated by electron beam irradiation in an SEM was characterised using CL and PL. A correlation was uncovered between the ability to activate emitters and the presence of the 4.1 eV emitters using CL spectroscopy. Modification of the existing emitter's structural configuration was proposed as a possible mechanism for the activation process. A 1000 °C annealing step increased the efficiency of emitter activation and allowed for emitters to be created in wider range of hBN including those from commercial sources. Near deterministic creation was demonstrated including spatial and spectral selectivity and an array of single photon emitters were created with a 33 % yield of isolated single emitters.

Finally in Chapter 5 a modified SEM system capable of in-situ PL was utilised to investigate charge state switching of the V_B defect in hBN under simultaneous electron and laser excitation. Reversible switching of the V_B -1 and 0 charge stages was demonstrated with equilibrium states controlled by electron and photon fluxes. A graphene - hBN - graphene heterostructure device was used to control excess charge carriers injected into the hBN, enabling a stabilisation method to maintain the -1 charge state and maintain the addressable spin properties of the defect.

6.2 Outlook

In this section I will outline some possible future direction based on both the work in this thesis and general outlook based on the direction of current literature.

Some progress has been seen for recoil implantation methods since the publication of the work in Chapter 3, with thin dielectric films used to implant quantum emitters into diamond.[258] In this instance a Ga^+ FIB was utilised, further demonstrating the versatility of this method. A possible direction would be to move beyond diamond and look at other host materials and quantum emitter systems. hBN is one possible candidate with several aspects that lend itself

to this technique. The shallow implantation depth would be suitable given the nanometre scale thickness of hBN often used in applications. As carbon is readily available and not a typical ion species found on FIB systems it may also be a suitable dopant given that many hBN defects are proposed to be carbon related.[81,221,222,157,158]

For solid state emitters in hBN there are still many areas yet to explore. The recent discovery of blue emitters in hBN has paved the way toward device integration. The work in Chapter 4 has been especially rewarding and has opened up many avenues of research that were previously difficult or even inaccessible when working with emitters in hBN. Recent work has probed the cryogenic properties of the emitter and experimentally demonstrated a narrow distribution of the ZPL emissions as well as a measurement of Rabi oscillations, an indicator that the defect can support coherent superposition.[5] Further to this a clear demonstration of two-photon interference was seen using these emitters, a first for defects in hBN.[259] The deterministic nature of these emitters has also allowed for consistent coupling of emitters to cavity devices. Previous attempts at coupling hBN emitters to traditional photonic crystal cavity structures posed difficulties in matching cavity mode resonances with the emitter ZPL as well as localisation of the emitters to maximise Purcell enhancement. These efforts either achieved no coupling, used hybrid structures or relied on a combination of many structures and narrow spectral filtering.[260,261,262] The ability to both match a cavity design to the ZPL emission of blue emitters, as well as an ability to activate at the exact position, is something that has greatly increased the efficiency of coupling emitters to photonic crystal cavity structures. Using the methods uncovered in Chapter 4 a blue emitter in hBN was coupled to a monolithic 1D photonic crystal cavity fabricated from hBN.[9] Future works may also look toward alternative strategies for cavity coupled systems including tunable plano-concave microcavities[263] or fibre-based cavities.[264]

Finally for the charge switching of the V_B defect undertaken in Chapter 5. Integration of time-resolved capabilities into the SEM/PL system is a clear next step for this work. This would require a fast beam blanker synced to the time-correlation unit. As the system already has the capability to measure $g^{(2)}(\tau)$ (See Appendix A.4) this should be within reach. Beyond this, studying the effects of the electron beam on different hBN emitters is also a viable pathway

given that little is known about the charge state of these defects.

There is still much to be studied and understood about the creation methods used to engineer quantum emitters in diamond and hBN, so that they can be successfully integrated into future photonic quantum technologies. Charged particle microscopy has already shown it's suitability as a tool to create and modify defects, but there are many remaining avenues to explore that may increase efficiency and determinism of the utilised techniques. Fortunately, availability of new dual-beam systems, as well as the ever increasing number of solid state defects uncovered and studied give plenty of opportunity to continue research on these topics. The outlook is bright when looking at the future of charged particle microscopy and their use on solid state defects for photonic quantum technologies.

A

Appendix A

A.1 Spectrometer Comparison

Three different spectrometers have been used for the experimental work presented across all chapters of this thesis. They are the built-in CL spectrometer (Andor Kymera 193i), main PL spectrometer (Princeton Instrument) and spectrometer utilised for work at cryogenic temperatures (SR303I, Andor), labelled A-C respectively in Figure A.1. For correction, the same diode laser source (peak centre at 532.3 nm) was used as a reference. The measured laser peak profiles on each spectrometer are fitted with Voigt function. The major peak component (either gaussian or Lorenzian peak) is determined as the laser peak. As shown above, the variance is within 3 nm. This spectra calibration data and all spectra in this thesis are collected with 300 l/mm grating. The calibration of spectrometers (wavelength vs camera pixels) may not be a

linear relationship, but on the same grating is comparable. For the work in Chapter 4 all three spectrometers were utilised with the CL spectrometer is selected as the standard. Data taken from other spectrometers has been shifted towards it accordingly. Specifically, the wavelength values are manually adjusted, +0.89 nm for the main PL spectrometer and -2.2 nm for cryogenic temperature spectrometer.

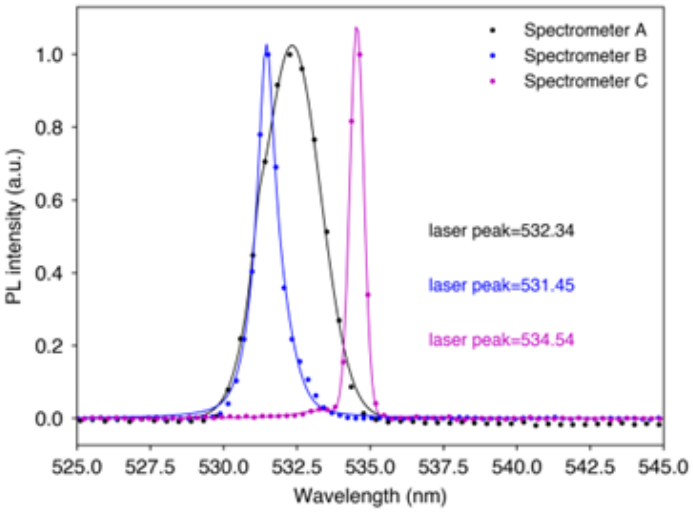

Figure A.1: *Three different spectrometers were utilised for the figures in this work named A-C. The position of the fitted peaks has been written in the colour corresponding to each curve.*

A.2 Individual correlation functions from the array in Chapter 4

Correlation functions from the array in Chapter 4, Figure 4.5 can be seen in Figure A.2. The experimental data has been fit with a three-level model:

$$g^{(2)}(\tau) = 1 - (1+a)e^{\frac{-t}{\tau_1}} + ae^{\frac{-t}{\tau_2}} \tag{A.1}$$

Where a is the amplitude parameter, τ_1 and τ_2 are lifetime values of the excited and metastables states respectively. No background correction has been undertaken here and it is clear that each correlation plot all sites show non-classical $g^{(2)}(0)$ values ranging from 0.2-0.8.

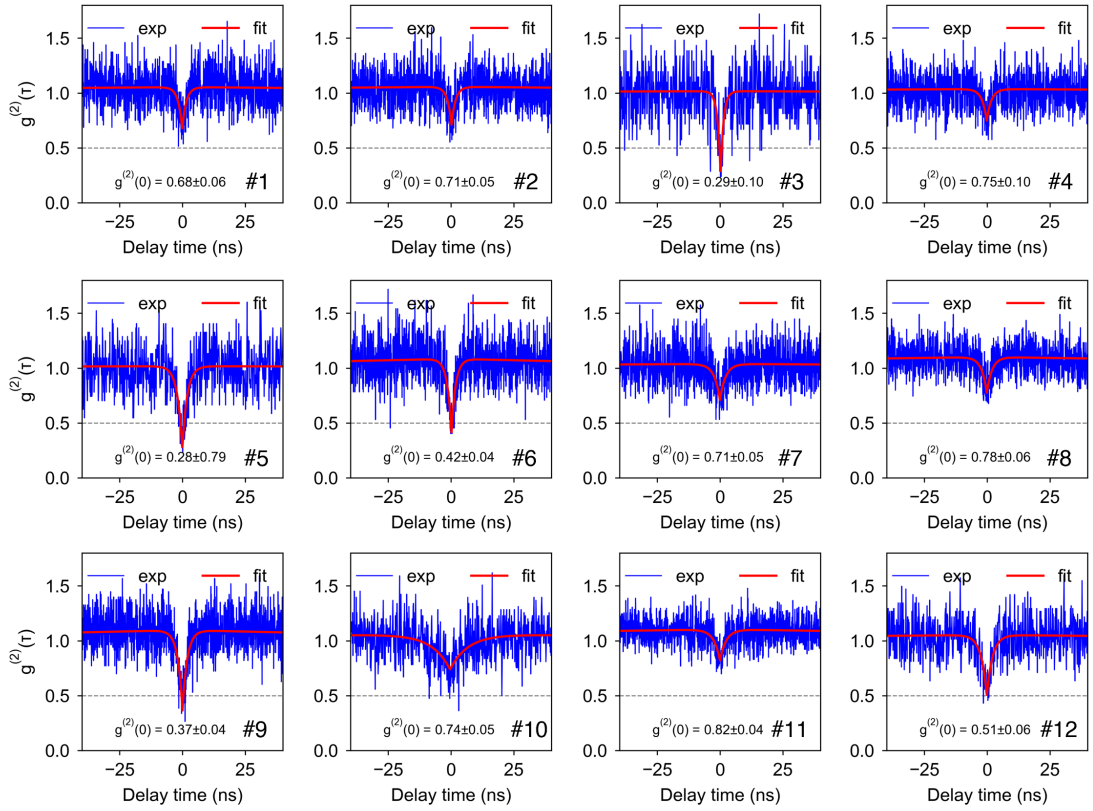

Figure A.2: *Individual correlation functions for blue emitters in the array from Chapter 4. The plots are numbered 1-12 corresponding to the sites in 4.5 and have been fitted with a three-level model in red. The $g^{(2)}(0)$ values are given at the bottom of each plot.*

A.3 CL Mapping of Hexagonal Boron Nitride

One benefit of the CL system used in Chapter 4 is the ability to take hyper-spectral maps, or more specifically, take individual spectra at each pixel to increase the data dimensionality over a standard panchromatic mapping. A 3×4 array was patterned with a focused electron beam onto a Type Ia (non annealed) flake to produced ensembles of blue emitters (dose increasing left to right, top to bottom). To demonstrate the spatial dependence on the spectral features of interest a hyper-spectral CL map was taken of the area (10 keV, 1 nA, 130 ms integration, 200 nm pixel spacing). The SEM micrograph shows high contrast areas at the irradiated spots without a regular contrast visible across the remaining regions of the hBN flake. The dark spot is

likely due to some contamination during exfoliation. Hyper-spectral CL maps uncover a wealth of information about the spatial location of important spectral features. The CL maps in Figure A.3 show the intensity of the spectral features listed. These correspond to approximately the band-edge emission of hBN (215±12.5 nm), UV defect induced emissions from grain boundaries and possible strained regions (245±12.5 nm), the 4.1 eV emission (315±25 nm) and the blue SPE emission (455±25 nm). A CL spectra with these regions shaded have been taken at the location of a blue emitter showing the typical emissions. It is notable that the peak at ∼430 nm is due to the second-order band-edge emission and not the blue emitters.

Focusing firstly on the two highest energy filtered maps shows a relatively homogeneous band-edge emission on most of the region. The irradiated spots are notably lower intensity, possibly indicating a reduced crystalline lattice due to electron induced modification or possibly competitive recombination pathways with the blue emitters formed at these regions.[116] The next highest energy map shows brighter regions not visible in the SEM image. These are likely from grain boundaries or dislocations resulting in trapped excitons at defect sites along these regions.[180,265] The inverse can be seen in the band-edge emission map with faint dark lines corresponding to the bright regions in aforementioned map. Next looking at the two lower energy regions, approximately corresponding to the 4.1 eV emission and blue emitter regions. The map of the 4.1 eV emission shows a patchy but relatively consistent emission across the flake. There is an increase in intensity toward the upper edge of the flake possibly indicating a higher concentration of the particular defect sites in this region. CL studies of these defects have shown such inhomogeneity in individual flakes based on the location of carbon rich domains.[155] Similar to the higher energy maps, dark spots are seen at the irradiation sites, indicative of a competitive recombination pathway, or speculatively, based on the work in Chapter 4, a modification of the defect to the blue emitter configuration.[3] Given sufficient resolution of the map, it is possible that individual 4.1 eV emitters could be isolated.[153,116]

Focusing finally on the map filtered for blue emission, distinct bright regions are present at irradiated sites as expected from focused electron irradiations.[3,161] It is clear that additional irradiations from SEM imaging and the CL mapping have also activated such emitters across

the flake with point-like bright regions distributed across the flake itself.

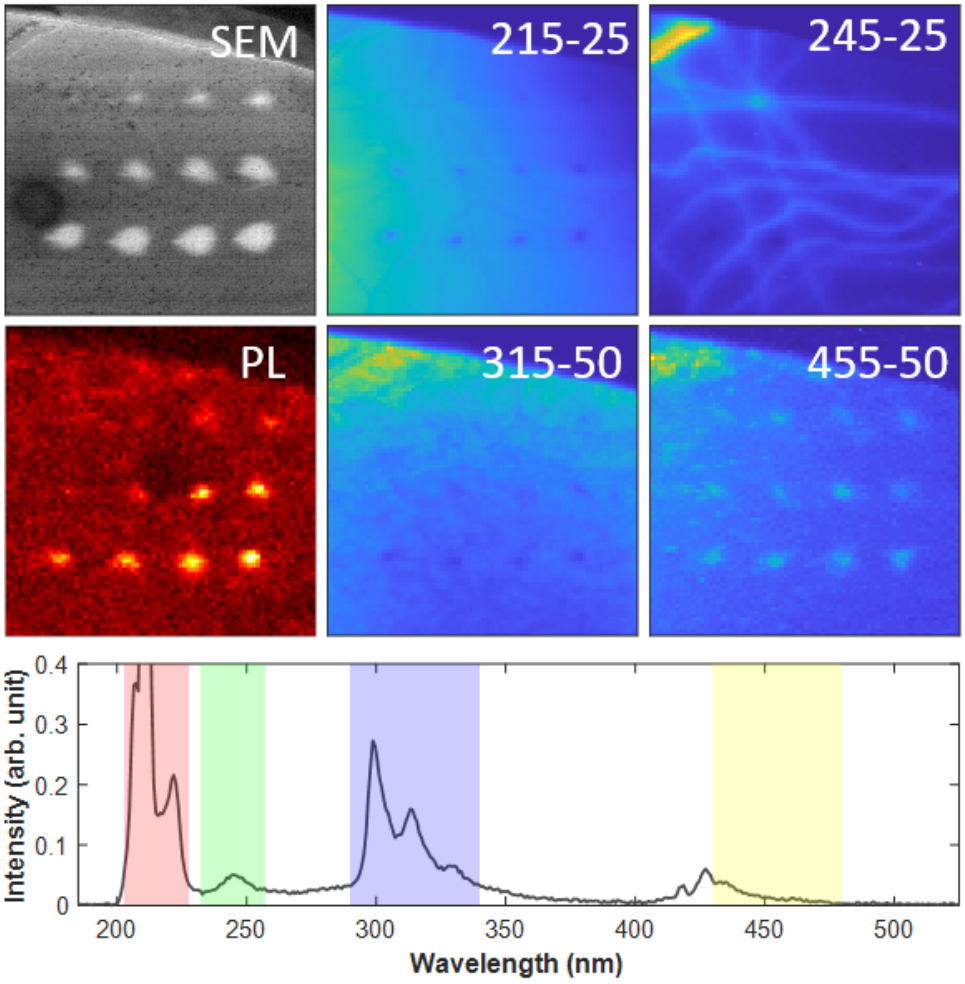

Figure A.3: *An SEM micrograph, PL confocal map and Hyper-spectral CL maps filtered with the centre wavelength, x and bandwidth, y in the format $x - y$ nm of a Type I hBN flake with 3×4 array patterned with focused electron irradiation. (bottom panel) Selected CL spectra from an irradiated region with the filtered spectral regions highlighted.*

A.4 Characterisation of the Integrated Confocal Microscope on SEM

A.4.1 Confocality

As the optical system used in Chapter 5 was scratch-built to suit the experimental needs, some optical characterisation is necessary to properly understand the limits of the system. To first characterise the theoretical lateral resolution of the system the Rayleigh criterion can be applied (Eq. A.2). This equation gives the smallest distance in which two point like emitters can be resolved.

$$R = \frac{1.22\lambda}{NA_{obj} + NA_{cond}} \tag{A.2}$$

With R the resolution limit, λ, wavelength of excitation laser, and NA_{obj} and NA_{cond} the numerical aperture (NA) of the objective and condenser lens respectively. Calculating for this setup with a 1.4 NA oil immersion objective and 0.4 NA condenser lens to the collection fibre give a theoretical resolution limit of 360 nm with 532 nm excitation.

For a confocal microscope setup, a pinhole is required to remove signals from out of focus regions. Rather than a traditional pinhole, the setup uses the core diameter of the collection fibre to achieve this confocality. Generally confocality is achieved when the core size is approximately equal to the diameter of 1 Airy Unit (AU), or more specifically the diameter of the central intensity maximum to the first diffraction minimum known as the Airy Disk, when taking into account the magnification of the system. The radius of the Airy Disk (r_{airy}) can be calculated using Equation A.3 below. It is similar to the Rayleigh criterion however only relies on the wavelength and NA of the objective. In order to account for the magnification of the system, the back-projected pinhole radius (r_{BPP}) can be calculated using Equation A.4.

$$r_{airy} = \frac{0.61\lambda}{NA_{obj}} \tag{A.3}$$

$$r_{BPP} = \frac{r_{pinhole}}{M_{system}} \tag{A.4}$$

With $r_{pinhole}$ the true pinhole radius and M_{system} the magnification of the entire system taking into account objective and fibre coupling lens. For this system r_{airy} is calculated to be 232 nm. For true confocality to be met the back-projected pinhole radius (r_{BPP}) should be approximately equal to r_{airy}. For this system the current r_{BPP} is 3470 nm. In terms of airy units this corresponds to a value of $\sim$15 AU. In order to achieve confocality either the focal length of the fibre coupling lens could be increased or the pinhole radius reduced. Increased confocality would bring other benefits to the system, including an ability to pinpoint laser excitations to a specific depth, esepecially important when dealing with non-uniformity of SPEs in solid state samples.

A.4.2 Additional Testing

Also included here are some maps and spectra taken from early testing of the same setup. Bulk MoS_2 was exfoliated onto an ITO coverslip. Monolayer regions were identified and subsequent PL map and spectra were taken as seen in Figure A.4. The bright and dim regions on the confocal map (Fig. A.4 (a) correspond to mono and bi-layers respectively. Monolayers of TMDCs have shown strong luminescence due to their direct band nature at the monolayer limit with spectra taken from monolayer regions (Fig. A.4 (b)) showing typical PL emission at $\sim$690 nm.[266] The setup also shows negligible background from the substrate. Spectra from a single emitter in hBN was also recorded as seen in Figure A.4(c). The corresponding $g^{(2)}(\tau)$ measurement can be seen in Figure A.4(d), with $g^{(2)}(0) > 0.5$

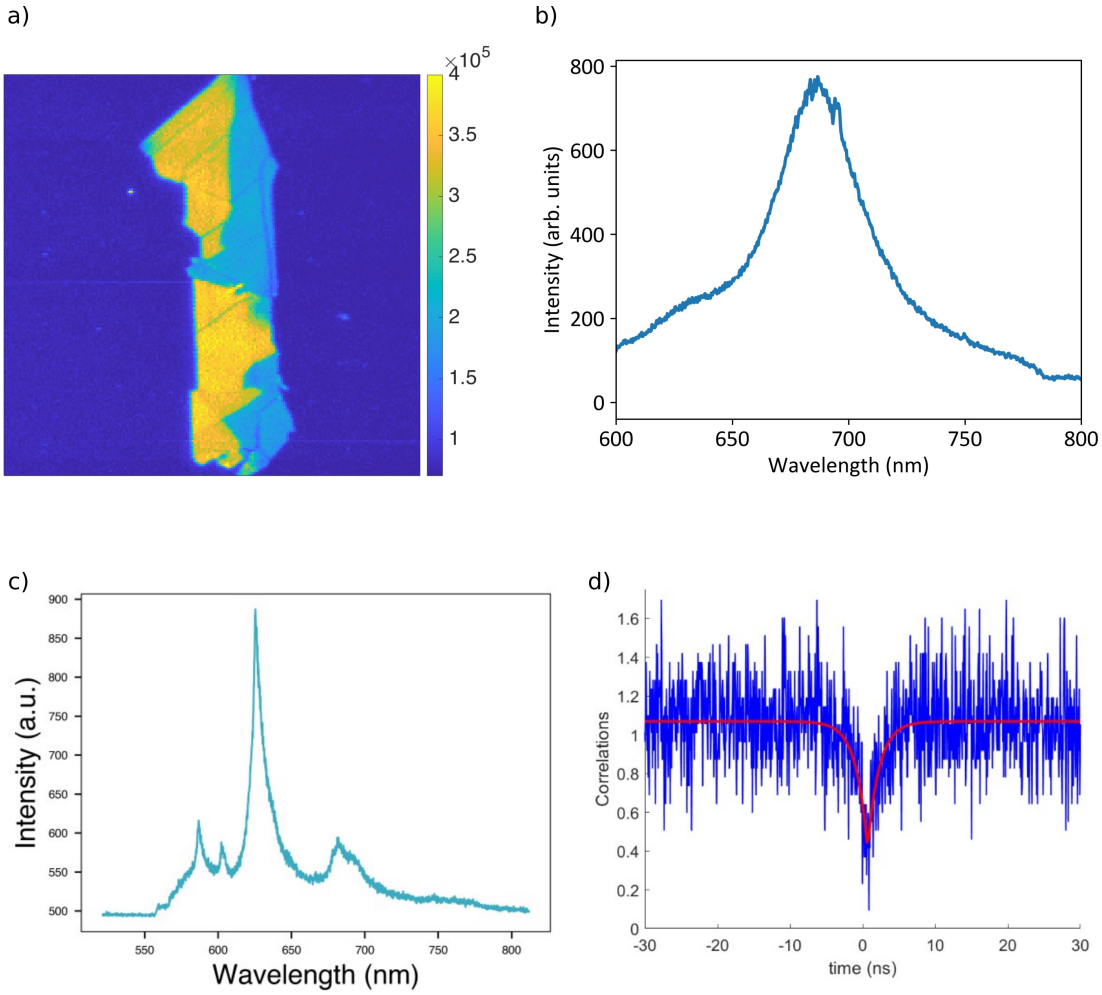

Figure A.4: *a) A confocal PL map of an exfoliated MoS_2 flake taken using the integrated CL/PL setup in 5. The bright regions correspond with atomically thin monolayer portions of the flake. b) Spectra taken from the bright monolayer regions in a). c) Spectra of a single emitter in hBN. d) Corresponding $g^{(2)}(\tau)$ measurement from the emitter in c).*

A.4.3 Setup Image

As a final addition to this Appendix, I thought it would be fitting to include an image of the setup that I am particularly fond of. Whilst not adding much to the overall story of this work (except maybe to highlight the compact nature of the optical pathway). It took many hours of work to get the system up and running, and at times it appeared that it would never see the light of day. I am proud of what was done and the results that were collected by this setup, so if nothing else this is for me.

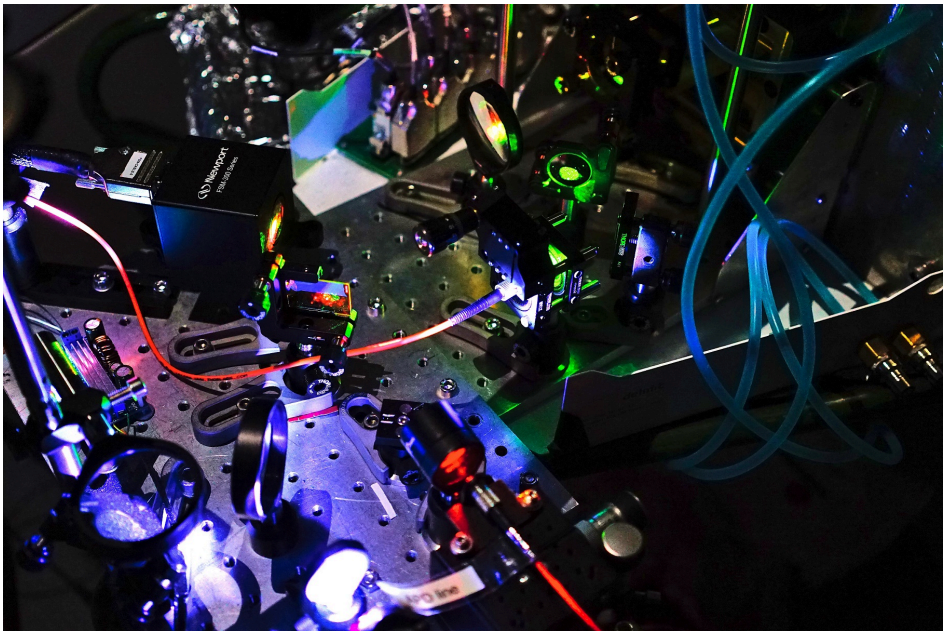

Figure A.5: *Image of the optical setup on the SEM, illuminated by green and red lasers as well as the white imaging LED.*

References

[1] J. E. Fröch, A. Bahm, M. Kianinia, Z. Mu, V. Bhatia, S. Kim, J. M. Cairney, W. Gao, C. Bradac, I. Aharonovich, and M. Toth, "Versatile direct-writing of dopants in a solid state host through recoil implantation," *Nature Communications*, vol. 11, no. 1, p. 5039, 2020.

[2] A. Gale, J. E. Fröch, M. Kianinia, J. Bishop, I. Aharonovich, and M. Toth, "Recoil implantation using gas-phase precursor molecules," *Nanoscale*, vol. 13, no. 20, pp. 9322–9327, 2021.

[3] A. Gale, C. Li, Y. Chen, K. Watanabe, T. Taniguchi, I. Aharonovich, and M. Toth, "Site-specific fabrication of blue quantum emitters in hexagonal boron nitride," *ACS Photonics*, vol. 9, no. 6, pp. 2170–2177, 2022.

[4] A. Gale, D. Scognamiglio, I. Zhigulin, B. Whitefield, M. Kianinia, I. Aharonovich, and M. Toth, "Manipulating the charge state of spin defects in hexagonal boron nitride," *Nano Letters*, vol. 23, no. 13, pp. 6141–6147, 2023.

[5] J. Horder, S. J. U. White, A. Gale, C. Li, K. Watanabe, T. Taniguchi, M. Kianinia, I. Aharonovich, and M. Toth, "Coherence properties of electron-beam-activated emitters in hexagonal boron nitride under resonant excitation," *Physical Review Applied*, vol. 18, no. 6, p. 064021, 2022.

[6] I. Zhigulin, J. Horder, V. Ivády, S. J. U. White, A. Gale, C. Li, C. J. Lobo, M. Toth, I. Aharonovich, and M. Kianinia, "Stark effect of blue quantum emitters in hexagonal boron nitride," *Physical Review Applied*, vol. 19, no. 4, p. 044011, 2023.

[7] Y. Chen, A. Gale, K. Yamamura, J. Horder, A. Condos, K. Watanabe, T. Taniguchi, M. Toth, and I. Aharonovich, "Annealing of blue quantum emitters in carbon-doped hexagonal boron nitride," *Applied Physics Letters*, vol. 123, no. 4, 2023.

[8] I. Zhigulin, K. Yamamura, V. Ivády, A. Gale, J. Horder, C. J. Lobo, M. Kianinia, M. Toth, and I. Aharonovich, "Photophysics of blue quantum emitters in hexagonal boron nitride," *Materials for Quantum Technology*, vol. 3, no. 1, p. 015002, 2023.

[9] M. Nonahal, J. Horder, A. Gale, L. Ding, C. Li, M. Hennessey, S. T. Ha, M. Toth, and I. Aharonovich, "Deterministic fabrication of a coupled cavity–emitter system in hexagonal boron nitride," *Nano Letters*, 2023.

[10] T. N. Tran, A. Gale, B. Whitefield, V. Dyakonov, M. Toth, I. Aharonovich, and M. Kianinia, "Coupling spin defects in hexagonal boron nitride to a microwave cavity," *Applied Physics Letters*, vol. 123, no. 3, 2023.

[11] L. Sortino, A. Gale, L. Kühner, C. Li, J. Biechteler, F. J. Wendisch, M. Kianinia, H. Ren, M. Toth, S. A. Maier, I. Aharonovich, and A. Tittl, "Optically addressable spin defects coupled to bound states in the continuum metasurfaces," *Nature Communications*, vol. 15, no. 1, p. 2008, 2024.

[12] T. N. Theis and H.-S. P. Wong, "The end of moore's law: A new beginning for information technology," *Computing in Science & Engineering*, vol. 19, no. 2, pp. 41–50, 2017.

[13] S. Castelletto and A. Boretti, "Perspective on solid-state single-photon sources in the infrared for quantum technology," *Advanced Quantum Technologies*, vol. 6, no. 10, p. 2300145, 2023.

[14] J. L. O'Brien, A. Furusawa, and J. Vučković, "Photonic quantum technologies," *Nature Photonics*, vol. 3, no. 12, pp. 687–695, 2009.

[15] J. Wang, F. Sciarrino, A. Laing, and M. G. Thompson, "Integrated photonic quantum technologies," *Nature Photonics*, vol. 14, no. 5, pp. 273–284, 2020.

[16] M. Planck, "Ueber das gesetz der energieverteilung im normalspectrum," *Annalen der Physik*, vol. 309, no. 3, pp. 553–563, 1901.

[17] A. Einstein, "Über einen die erzeugung und verwandlung des lichtes betreffenden heuristischen gesichtspunkt," *Annalen der Physik*, vol. 322, no. 6, pp. 132–148, 1905.

[18] V. Scarani, H. Bechmann-Pasquinucci, N. J. Cerf, M. Dušek, N. Lütkenhaus, and M. Peev, "The security of practical quantum key distribution," *Rev. Mod. Phys.*, vol. 81, pp. 1301–1350, 2009.

[19] H.-K. Lo, M. Curty, and K. Tamaki, "Secure quantum key distribution," *Nature Photonics*, vol. 8, no. 8, pp. 595–604, 2014.

[20] H. Singh, D. L. Gupta, and A. K. Singh, "Quantum key distribution protocols: a review," *Journal of Computer Engineering*, vol. 16, no. 2, pp. 1–9, 2014.

[21] C. H. Bennett and G. Brassard, "Quantum cryptography: Public key distribution and coin tossing," in *Proceedings of the IEEE International Conference on Computers, Systems and Signal Processing*, pp. 175–179, IEEE New York, 1984.

[22] A. I. Nurhadi and N. R. Syambas, "Quantum key distribution (qkd) protocols: A survey," in *2018 4th International Conference on Wireless and Telematics (ICWT)*, pp. 1–5, 2018.

[23] Z.-S. Yuan, X.-H. Bao, C.-Y. Lu, J. Zhang, C.-Z. Peng, and J.-W. Pan, "Entangled photons and quantum communication," *Physics Reports*, vol. 497, no. 1, pp. 1–40, 2010.

[24] Y. Liu, W.-J. Zhang, C. Jiang, J.-P. Chen, C. Zhang, W.-X. Pan, D. Ma, H. Dong, J.-M. Xiong, C.-J. Zhang, H. Li, R.-C. Wang, J. Wu, T.-Y. Chen, L. You, X.-B. Wang, Q. Zhang, and J.-W. Pan, "Experimental twin-field quantum key distribution over 1000 km fiber distance," *Phys. Rev. Lett.*, vol. 130, p. 210801, 2023.

[25] D. Deutsch, "Quantum theory, the church–turing principle and the universal quantum computer," *Proceedings of the Royal Society of London. A. Mathematical and Physical Sciences*, vol. 400, no. 1818, pp. 97–117, 1985.

[26] M. Brooks, "Quantum computers: what are they good for?," *Nature*, vol. 617, no. 7962, pp. S1–S3, 2023.

[27] J. R. Weber, W. F. Koehl, J. B. Varley, A. Janotti, B. B. Buckley, C. G. Van de Walle, and D. D. Awschalom, "Quantum computing with defects," *Proceedings of the National Academy of Sciences*, vol. 107, no. 19, pp. 8513–8518, 2010.

[28] G. Wolfowicz, F. J. Heremans, C. P. Anderson, S. Kanai, H. Seo, A. Gali, G. Galli, and D. D. Awschalom, "Quantum guidelines for solid-state spin defects," *Nature Reviews Materials*, vol. 6, no. 10, pp. 906–925, 2021.

[29] C. L. Degen, F. Reinhard, and P. Cappellaro, "Quantum sensing," *Rev. Mod. Phys.*, vol. 89, p. 035002, 2017.

[30] X. Liu and M. C. Hersam, "2d materials for quantum information science," *Nature Reviews Materials*, vol. 4, no. 10, pp. 669–684, 2019.

[31] S. Slussarenko and G. J. Pryde, "Photonic quantum information processing: A concise review," *Applied Physics Reviews*, vol. 6, no. 4, 2019.

[32] D. McMullan, "Scanning electron microscopy 1928–1965," *Scanning*, vol. 17, no. 3, pp. 175–185, 1995.

[33] K. Kanaya and S. Okayama, "Penetration and energy-loss theory of electrons in solid targets," *Journal of Physics D: Applied Physics*, vol. 5, no. 1, p. 43, 1972.

[34] A. P. Conlan, E. Tillotson, A. Rakowski, D. Cooper, and S. J. Haigh, "Direct measurement of TEM lamella thickness in FIB-SEM," *Journal of Microscopy*, vol. 279, no. 3, pp. 168–176, 2020.

[35] J. I. Goldstein, D. E. Newbury, J. R. Michael, N. W. Ritchie, J. H. J. Scott, and D. C. Joy, *Scanning electron microscopy and X-ray microanalysis*. Springer, 2017.

[36] B. W. Caplins, J. D. Holm, R. M. White, and R. R. Keller, "Orientation mapping of graphene using 4d stem-in-sem," *Ultramicroscopy*, vol. 219, p. 113137, 2020.

[37] L. Reimer, *Scanning Electron Microscopy: Physics of Image Formation and Microanalysis*, vol. 45 of *Springer*. Springer Berlin, Heidelberg, 1st ed., 1985.

[38] D. E. Newbury and N. W. M. Ritchie, "Performing elemental microanalysis with high accuracy and high precision by scanning electron microscopy/silicon drift detector energy-dispersive x-ray spectrometry (SEM/SDD-EDS)," *Journal of Materials Science*, vol. 50, no. 2, pp. 493–518, 2015.

[39] J. Kotakoski, C. H. Jin, O. Lehtinen, K. Suenaga, and A. V. Krasheninnikov, "Electron knock-on damage in hexagonal boron nitride monolayers," *Physical Review B*, vol. 82, no. 11, p. 113404, 2010.

[40] H.-P. Komsa, J. Kotakoski, S. Kurasch, O. Lehtinen, U. Kaiser, and A. V. Krasheninnikov, "Two-dimensional transition metal dichalcogenides under electron irradiation: Defect production and doping," *Physical Review Letters*, vol. 109, no. 3, p. 035503, 2012.

[41] R. F. Egerton, P. Li, and M. Malac, "Radiation damage in the TEM and SEM," *Micron*, vol. 35, no. 6, pp. 399–409, 2004.

[42] J. Cazaux, "Some considerations on the electric field induced in insulators by electron bombardment," *Journal of Applied Physics*, vol. 59, no. 5, pp. 1418–1430, 1986.

[43] D. T. Grubb, "Radiation damage and electron microscopy of organic polymers," *Journal of Materials Science*, vol. 9, no. 10, pp. 1715–1736, 1974.

[44] D. G. Howitt and G. Thomas, "Electron damage in organic crystals," *Radiation Effects*, vol. 34, no. 4, pp. 209–215, 1977.

[45] W. Zhou and Z. L. Wang, *Scanning microscopy for nanotechnology: techniques and applications*. Springer science & business media, 2007.

[46] I. Utke, S. Moshkalev, and P. Russell, *Nanofabrication Using Focused Ion and Electron Beams: Principles and Applications*. Oxford University Press, USA, 2012.

[47] P. Li, S. Chen, H. Dai, Z. Yang, Z. Chen, Y. Wang, Y. Chen, W. Peng, W. Shan, and H. Duan, "Recent advances in focused ion beam nanofabrication for nanostructures and devices: fundamentals and applications," *Nanoscale*, vol. 13, no. 3, pp. 1529–1565, 2021.

[48] G. Hlawacek, V. Veligura, R. van Gastel, and B. Poelsema, "Helium ion microscopy," *Journal of Vacuum Science & Technology B*, vol. 32, no. 2, p. 020801, 2014.

[49] L. A. Giannuzzi and F. A. Stevie, *Introduction to focused ion beams: instrumentation, theory, techniques and practice*. Springer Science & Business Media, 2004.

[50] C. A. Volkert and A. M. Minor, "Focused ion beam microscopy and micromachining," *MRS Bulletin*, vol. 32, no. 5, pp. 389–399, 2007.

[51] N. Bassim, K. Scott, and L. A. Giannuzzi, "Recent advances in focused ion beam technology and applications," *MRS Bulletin*, vol. 39, no. 4, pp. 317–325, 2014.

[52] T. L. Burnett, R. Kelley, B. Winiarski, L. Contreras, M. Daly, A. Gholinia, M. G. Burke, and P. J. Withers, "Large volume serial section tomography by xenon plasma FIB dual beam microscopy," *Ultramicroscopy*, vol. 161, pp. 119–129, 2016.

[53] T. Ishitani, H. Koike, T. Yaguchi, and T. Kamino, "Implanted gallium-ion concentrations of focused-ion-beam prepared cross sections," *Journal of Vacuum Science & Technology B: Microelectronics and Nanometer Structures Processing, Measurement, and Phenomena*, vol. 16, no. 4, pp. 1907–1913, 1998.

[54] J. M. Cairney, P. R. Munroe, and R. D. Smith, "Transmission electron microscope specimen preparation of metal matrix composites using the focused ion beam miller," *Microscopy and Microanalysis*, vol. 6, no. 5, pp. 452–462, 2000.

[55] J. R. Michael, L. A. Giannuzzi, M. G. Burke, and X. L. Zhong, "Mechanism of FIB-induced phase transformation in austenitic steel," *Microscopy and Microanalysis*, vol. 28, no. 1, pp. 70–82, 2022.

[56] R. P. Babu, S. Irukuvarghula, A. Harte, and M. Preuss, "Nature of gallium focused ion beam induced phase transformation in 316l austenitic stainless steel," *Acta Materialia*, vol. 120, pp. 391–402, 2016.

[57] A. V. Krasheninnikov and K. Nordlund, "Ion and electron irradiation-induced effects in nanostructured materials," *Journal of Applied Physics*, vol. 107, no. 7, p. 071301, 2010.

[58] M. T. Postek, "An approach to the reduction of hydrocarbon contamination in the scanning electron microscope," *Scanning*, vol. 18, no. 4, pp. 269–274, 1996.

[59] I. Utke, P. Hoffmann, and J. Melngailis, "Gas-assisted focused electron beam and ion beam processing and fabrication," *Journal of Vacuum Science & Technology B: Microelectronics and Nanometer Structures Processing, Measurement, and Phenomena*, vol. 26, no. 4, pp. 1197–1276, 2008.

[60] S. J. Randolph, J. D. Fowlkes, and P. D. Rack, "Focused, nanoscale electron-beam-induced deposition and etching," *Critical Reviews in Solid State and Materials Sciences*, vol. 31, no. 3, pp. 55–89, 2006.

[61] L. G. Christophorou and J. K. Olthoff, *Fundamental electron interactions with plasma processing gases*. Springer Science & Business Media, 2012.

[62] H. Fujioka, K. Nakamae, M. Hirota, K. Ura, N. Tamura, and T. Takagi, "Measurements of the energy dependence of electron beam assisted etching of, and deposition on, silica," *Journal of Physics D: Applied Physics*, vol. 23, no. 2, pp. 266–268, 1990.

[63] W. F. van Dorp and C. W. Hagen, "A critical literature review of focused electron beam induced deposition," *Journal of Applied Physics*, vol. 104, no. 8, p. 081301, 2008.

[64] M. Toth, "Advances in gas-mediated electron beam-induced etching and related material processing techniques," *Applied Physics A*, vol. 117, no. 4, pp. 1623–1629, 2014.

[65] C. Thiele, A. Felten, T. J. Echtermeyer, A. C. Ferrari, C. Casiraghi, H. v. Löhneysen, and R. Krupke, "Electron-beam-induced direct etching of graphene," *Carbon*, vol. 64, pp. 84–91, 2013.

[66] A. A. Martin, G. McCredie, and M. Toth, "Electron beam induced etching of carbon," *Applied Physics Letters*, vol. 107, no. 4, p. 041603, 2015.

[67] J. W. Coburn and H. F. Winters, "Ion-and electron-assisted gas-surface chemistry—an important effect in plasma etching," *Journal of Applied physics*, vol. 50, no. 5, pp. 3189–3196, 1979.

[68] M. D. Eisaman, J. Fan, A. Migdall, and S. V. Polyakov, "Invited review article: Single-photon sources and detectors," *Review of Scientific Instruments*, vol. 82, no. 7, 2011.

[69] M. Hennrich, T. Legero, A. Kuhn, and G. Rempe, "Photon statistics of a non-stationary periodically driven single-photon source," *New Journal of Physics*, vol. 6, no. 1, p. 86, 2004.

[70] M. Hijlkema, B. Weber, H. P. Specht, S. C. Webster, A. Kuhn, and G. Rempe, "A single-photon server with just one atom," *Nature Physics*, vol. 3, no. 4, pp. 253–255, 2007.

[71] C. Maurer, C. Becher, C. Russo, J. Eschner, and R. Blatt, "A single-photon source based on a single Ca+ ion," *New Journal of Physics*, vol. 6, no. 1, p. 94, 2004.

[72] M. Keller, B. Lange, K. Hayasaka, W. Lange, and H. Walther, "Continuous generation of single photons with controlled waveform in an ion-trap cavity system," *Nature*, vol. 431, no. 7012, pp. 1075–1078, 2004.

[73] P. Michler, A. Kiraz, C. Becher, W. V. Schoenfeld, P. M. Petroff, L. Zhang, E. Hu, and A. Imamoglu, "A quantum dot single-photon turnstile device," *Science*, vol. 290, no. 5500, pp. 2282–2285, 2000.

[74] C. Santori, M. Pelton, G. Solomon, Y. Dale, and Y. Yamamoto, "Triggered single photons from a quantum dot," *Physical Review Letters*, vol. 86, no. 8, pp. 1502–1505, 2001.

[75] C. Marand and P. D. Townsend, "Quantum key distribution over distances as long as 30 km," *Optics Letters*, vol. 20, no. 16, pp. 1695–1697, 1995.

[76] W. T. Buttler, R. J. Hughes, S. K. Lamoreaux, G. L. Morgan, J. E. Nordholt, and C. G. Peterson, "Daylight quantum key distribution over 1.6 km," *Physical Review Letters*, vol. 84, no. 24, pp. 5652–5655, 2000.

[77] S. Fasel, O. Alibart, S. Tanzilli, P. Baldi, A. Beveratos, N. Gisin, and H. Zbinden, "High-quality asynchronous heralded single-photon source at telecom wavelength," *New Journal of Physics*, vol. 6, no. 1, p. 163, 2004.

[78] I. Aharonovich, D. Englund, and M. Toth, "Solid-state single-photon emitters," *Nature Photonics*, vol. 10, no. 10, pp. 631–641, 2016.

[79] C. Bradac, W. Gao, J. Forneris, M. E. Trusheim, and I. Aharonovich, "Quantum nanophotonics with group iv defects in diamond," *Nature Communications*, vol. 10, no. 1, p. 5625, 2019.

[80] A. Lohrmann, B. C. Johnson, J. C. McCallum, and S. Castelletto, "A review on single photon sources in silicon carbide," *Reports on Progress in Physics*, vol. 80, no. 3, p. 034502, 2017.

[81] N. Mendelson, D. Chugh, J. R. Reimers, T. S. Cheng, A. Gottscholl, H. Long, C. J. Mellor, A. Zettl, V. Dyakonov, P. H. Beton, S. V. Novikov, C. Jagadish, H. H. Tan, M. J. Ford, M. Toth, C. Bradac, and I. Aharonovich, "Identifying carbon as the source of visible single-photon emission from hexagonal boron nitride," *Nature Materials*, vol. 20, no. 3, pp. 321–328, 2021.

[82] P. Siyushev, K. Xia, R. Reuter, M. Jamali, N. Zhao, N. Yang, C. Duan, N. Kukharchyk, A. D. Wieck, R. Kolesov, and J. Wrachtrup, "Coherent properties of single rare-earth spin qubits," *Nature Communications*, vol. 5, no. 1, p. 3895, 2014.

[83] J. Klein, M. Lorke, M. Florian, F. Sigger, L. Sigl, S. Rey, J. Wierzbowski, J. Cerne, K. Müller, E. Mitterreiter, P. Zimmermann, T. Taniguchi, K. Watanabe, U. Wurstbauer, M. Kaniber, M. Knap, R. Schmidt, J. J. Finley, and A. W. Holleitner, "Site-selectively generated photon emitters in monolayer MoS_2 via local helium ion irradiation," *Nature Communications*, vol. 10, no. 1, p. 2755, 2019.

[84] A. J. Morfa, B. C. Gibson, M. Karg, T. J. Karle, A. D. Greentree, P. Mulvaney, and S. Tomljenovic-Hanic, "Single-photon emission and quantum characterization of zinc oxide defects," *Nano Letters*, vol. 12, no. 2, pp. 949–954, 2012.

[85] N. Somaschi, V. Giesz, L. De Santis, J. C. Loredo, M. P. Almeida, G. Hornecker, S. L. Portalupi, T. Grange, C. Antón, J. Demory, C. Gómez, I. Sagnes, N. D. Lanzillotti-Kimura, A. Lemaítre, A. Auffeves, A. G. White, L. Lanco, and P. Senellart, "Near-optimal single-photon sources in the solid state," *Nature Photonics*, vol. 10, no. 5, pp. 340–345, 2016.

[86] C. Santori, D. Fattal, J. Vučković, G. S. Solomon, and Y. Yamamoto, "Indistinguishable photons from a single-photon device," *Nature*, vol. 419, no. 6907, pp. 594–597, 2002.

[87] A. Isichenko, N. Chauhan, D. Bose, J. Wang, P. D. Kunz, and D. J. Blumenthal, "Photonic integrated beam delivery for a rubidium 3d magneto-optical trap," *Nature Communications*, vol. 14, no. 1, p. 3080, 2023.

[88] G. Zhang, Y. Cheng, J.-P. Chou, and A. Gali, "Material platforms for defect qubits and single-photon emitters," *Applied Physics Reviews*, vol. 7, no. 3, p. 031308, 2020.

[89] T. T. Tran, K. Bray, M. J. Ford, M. Toth, and I. Aharonovich, "Quantum emission from hexagonal boron nitride monolayers," *Nature Nanotechnology*, vol. 11, no. 1, pp. 37–41, 2016.

[90] E. Neu, D. Steinmetz, J. Riedrich-Möller, S. Gsell, M. Fischer, M. Schreck, and C. Becher, "Single photon emission from silicon-vacancy colour centres in chemical vapour deposition nano-diamonds on iridium," *New Journal of Physics*, vol. 13, no. 2, p. 025012, 2011.

[91] A. M. Fox, *Quantum optics: an introduction*, vol. 15. Oxford University Press, USA, 2006.

[92] V. Zwiller and G. Björk, "Improved light extraction from emitters in high refractive index materials using solid immersion lenses," *Journal of Applied Physics*, vol. 92, no. 2, pp. 660–665, 2002.

[93] A. M. Berhane, C. Bradac, and I. Aharonovich, "Photoinduced blinking in a solid-state quantum system," *Phys. Rev. B*, vol. 96, p. 041203, 2017.

[94] J. Robertson and M. J. Rutter, "Band diagram of diamond and diamond-like carbon surfaces," *Diamond and Related Materials*, vol. 7, no. 2, pp. 620–625, 1998.

[95] I. Aharonovich and E. Neu, "Diamond nanophotonics," *Advanced Optical Materials*, vol. 2, no. 10, pp. 911–928, 2014.

[96] C. Kurtsiefer, S. Mayer, P. Zarda, and H. Weinfurter, "Stable solid-state source of single photons," *Phys. Rev. Lett.*, vol. 85, pp. 290–293, 2000.

[97] N. Bar-Gill, L. M. Pham, A. Jarmola, D. Budker, and R. L. Walsworth, "Solid-state electronic spin coherence time approaching one second," *Nature Communications*, vol. 4, no. 1, p. 1743, 2013.

[98] H. Bernien, L. Childress, L. Robledo, M. Markham, D. Twitchen, and R. Hanson, "Two-photon quantum interference from separate nitrogen vacancy centers in diamond," *Phys. Rev. Lett.*, vol. 108, p. 043604, 2012.

[99] A. Sipahigil, M. L. Goldman, E. Togan, Y. Chu, M. Markham, D. J. Twitchen, A. S. Zibrov, A. Kubanek, and M. D. Lukin, "Quantum interference of single photons from remote nitrogen-vacancy centers in diamond," *Phys. Rev. Lett.*, vol. 108, p. 143601, 2012.

[100] G. D. Fuchs, G. Burkard, P. V. Klimov, and D. D. Awschalom, "A quantum memory intrinsic to single nitrogen–vacancy centres in diamond," *Nature Physics*, vol. 7, no. 10, pp. 789–793, 2011.

[101] H. J. Mamin, M. Kim, M. H. Sherwood, C. T. Rettner, K. Ohno, D. D. Awschalom, and D. Rugar, "Nanoscale nuclear magnetic resonance with a nitrogen-vacancy spin sensor," *Science*, vol. 339, no. 6119, pp. 557–560, 2013.

[102] T. Staudacher, F. Shi, S. Pezzagna, J. Meijer, J. Du, C. A. Meriles, F. Reinhard, and J. Wrachtrup, "Nuclear magnetic resonance spectroscopy on a (5-nanometer)^3 sample volume," *Science*, vol. 339, no. 6119, pp. 561–563, 2013.

[103] R. Hanson, V. V. Dobrovitski, A. E. Feiguin, O. Gywat, and D. D. Awschalom, "Coherent dynamics of a single spin interacting with an adjustable spin bath," *Science*, vol. 320, no. 5874, pp. 352–355, 2008.

[104] M. Solà-Garcia, S. Meuret, T. Coenen, and A. Polman, "Electron-induced state conversion in diamond nv centers measured with pump–probe cathodoluminescence spectroscopy," *ACS Photonics*, vol. 7, no. 1, pp. 232–240, 2020.

[105] P. Siyushev, H. Pinto, M. Vörös, A. Gali, F. Jelezko, and J. Wrachtrup, "Optically controlled switching of the charge state of a single nitrogen-vacancy center in diamond at cryogenic temperatures," *Phys. Rev. Lett.*, vol. 110, p. 167402, 2013.

[106] C. Schreyvogel, V. Polyakov, S. Burk, H. Fedder, A. Denisenko, F. F. de Oliveira, R. Wunderlich, J. Meijer, V. Zuerbig, J. Wrachtrup, and C. E. Nebel, "Active and fast charge-state switching of single nv centres in diamond by in-plane al-schottky junctions," *Beilstein Journal of Nanotechnology*, vol. 7, pp. 1727–1735, 2016.

[107] I. Bayn, E. H. Chen, M. E. Trusheim, L. Li, T. Schröder, O. Gaathon, M. Lu, A. Stein, M. Liu, K. Kisslinger, H. Clevenson, and D. Englund, "Generation of ensembles of individually resolvable nitrogen vacancies using nanometer-scale apertures in ultrahigh-aspect ratio planar implantation masks," *Nano Letters*, vol. 15, no. 3, pp. 1751–1758, 2015.

[108] S. Pezzagna, B. Naydenov, F. Jelezko, J. Wrachtrup, and J. Meijer, "Creation efficiency of nitrogen-vacancy centres in diamond," *New Journal of Physics*, vol. 12, no. 6, p. 065017, 2010.

[109] M. Lesik, P. Spinicelli, S. Pezzagna, P. Happel, V. Jacques, O. Salord, B. Rasser, A. Delobbe, P. Sudraud, A. Tallaire, J. Meijer, and J.-F. Roch, "Maskless and targeted creation of arrays of colour centres in diamond using focused ion beam technology," *physica status solidi (a)*, vol. 210, no. 10, pp. 2055–2059, 2013.

[110] S. Becker, N. Raatz, S. Jankuhn, R. John, and J. Meijer, "Nitrogen implantation with a scanning electron microscope," *Scientific Reports*, vol. 8, no. 1, p. 32, 2018.

[111] C. A. McLellan, B. A. Myers, S. Kraemer, K. Ohno, D. D. Awschalom, and A. C. Bleszynski Jayich, "Patterned formation of highly coherent nitrogen-vacancy centers using a focused electron irradiation technique," *Nano Letters*, vol. 16, no. 4, pp. 2450–2454, 2016.

[112] T. R. Eichhorn, C. A. McLellan, and A. C. Bleszynski Jayich, "Optimizing the formation of depth-confined nitrogen vacancy center spin ensembles in diamond for quantum sensing," *Physical Review Materials*, vol. 3, no. 11, p. 113802, 2019.

[113] B. C. Rose, C. D. Weis, A. M. Tyryshkin, T. Schenkel, and S. A. Lyon, "Spin coherence and 14n eseem effects of nitrogen-vacancy centers in diamond with x-band pulsed esr," *Diamond and Related Materials*, vol. 72, pp. 32–40, 2017.

[114] A. Faraon, C. Santori, Z. Huang, V. M. Acosta, and R. G. Beausoleil, "Coupling of nitrogen-vacancy centers to photonic crystal cavities in monocrystalline diamond," *Phys. Rev. Lett.*, vol. 109, p. 033604, 2012.

[115] K. Watanabe, T. Taniguchi, and H. Kanda, "Direct-bandgap properties and evidence for ultraviolet lasing of hexagonal boron nitride single crystal," *Nature materials*, vol. 3, no. 6, pp. 404–409, 2004.

[116] L. Schué, I. Stenger, F. Fossard, A. Loiseau, and J. Barjon, "Characterization methods dedicated to nanometer-thick hBN layers," *2D Materials*, vol. 4, no. 1, p. 015028, 2016.

[117] G. Cassabois, P. Valvin, and B. Gil, "Hexagonal boron nitride is an indirect bandgap semiconductor," *Nature Photonics*, vol. 10, no. 4, pp. 262–266, 2016.

[118] K. S. Novoselov, A. K. Geim, S. V. Morozov, D. Jiang, Y. Zhang, S. V. Dubonos, I. V. Grigorieva, and A. A. Firsov, "Electric field effect in atomically thin carbon films," *Science*, vol. 306, no. 5696, p. 666, 2004.

[119] K. S. Novoselov, D. Jiang, F. Schedin, T. J. Booth, V. V. Khotkevich, S. V. Morozov, and A. K. Geim, "Two-dimensional atomic crystals," *Proceedings of the National Academy of Sciences of the United States of America*, vol. 102, no. 30, p. 10451, 2005.

[120] A. Splendiani, L. Sun, Y. Zhang, T. Li, J. Kim, C.-Y. Chim, G. Galli, and F. Wang, "Emerging photoluminescence in monolayer MoS_2," *Nano Letters*, vol. 10, no. 4, pp. 1271–1275, 2010.

[121] M. Chhowalla, H. S. Shin, G. Eda, L.-J. Li, K. P. Loh, and H. Zhang, "The chemistry of two-dimensional layered transition metal dichalcogenide nanosheets," *Nature Chemistry*, vol. 5, no. 4, pp. 263–275, 2013.

[122] R. V. Gorbachev, I. Riaz, R. R. Nair, R. Jalil, L. Britnell, B. D. Belle, E. W. Hill, K. S. Novoselov, K. Watanabe, T. Taniguchi, A. K. Geim, and P. Blake, "Hunting for monolayer boron nitride: Optical and raman signatures," *Small*, vol. 7, no. 4, pp. 465–468, 2011.

[123] F. Pizzocchero, L. Gammelgaard, B. S. Jessen, J. M. Caridad, L. Wang, J. Hone, P. Bøggild, and T. J. Booth, "The hot pick-up technique for batch assembly of van der waals heterostructures," *Nature Communications*, vol. 7, no. 1, p. 11894, 2016.

[124] D. G. Purdie, N. M. Pugno, T. Taniguchi, K. Watanabe, A. C. Ferrari, and A. Lombardo, "Cleaning interfaces in layered materials heterostructures," *Nature Communications*, vol. 9, no. 1, p. 5387, 2018.

[125] M. Kianinia, Z.-Q. Xu, M. Toth, and I. Aharonovich, "Quantum emitters in 2d materials: Emitter engineering, photophysics, and integration in photonic nanostructures," *Applied Physics Reviews*, vol. 9, no. 1, 2022.

[126] T. T. Tran, C. Elbadawi, D. Totonjian, C. J. Lobo, G. Grosso, H. Moon, D. R. Englund, M. J. Ford, I. Aharonovich, and M. Toth, "Robust multicolor single photon emission from point defects in hexagonal boron nitride," *ACS Nano*, vol. 10, no. 8, pp. 7331–7338, 2016.

[127] M. Kianinia, B. Regan, S. A. Tawfik, T. T. Tran, M. J. Ford, I. Aharonovich, and M. Toth, "Robust solid-state quantum system operating at 800 k," *ACS Photonics*, vol. 4, no. 4, pp. 768–773, 2017.

[128] W. Liu, Y.-T. Wang, Z.-P. Li, S. Yu, Z.-J. Ke, Y. Meng, J.-S. Tang, C.-F. Li, and G.-C. Guo, "An ultrastable and robust single-photon emitter in hexagonal boron nitride," *Physica E: Low-dimensional Systems and Nanostructures*, vol. 124, p. 114251, 2020.

[129] A. Dietrich, M. Bürk, E. S. Steiger, L. Antoniuk, T. T. Tran, M. Nguyen, I. Aharonovich, F. Jelezko, and A. Kubanek, "Observation of fourier transform limited lines in hexagonal boron nitride," *Physical Review B*, vol. 98, no. 8, p. 081414, 2018.

[130] H. L. Stern, Q. Gu, J. Jarman, S. Eizagirre Barker, N. Mendelson, D. Chugh, S. Schott, H. H. Tan, H. Sirringhaus, I. Aharonovich, and M. Atatüre, "Room-temperature optically detected magnetic resonance of single defects in hexagonal boron nitride," *Nature Communications*, vol. 13, no. 1, p. 618, 2022.

[131] F. Hayee, L. Yu, J. L. Zhang, C. J. Ciccarino, M. Nguyen, A. F. Marshall, I. Aharonovich, J. Vučković, P. Narang, T. F. Heinz, and J. A. Dionne, "Revealing multiple classes of stable quantum emitters in hexagonal boron nitride with correlated optical and electron microscopy," *Nature Materials*, vol. 19, no. 5, pp. 534–539, 2020.

[132] A. Kumar, C. Cholsuk, A. Zand, M. N. Mishuk, T. Matthes, F. Eilenberger, S. Suwanna, and T. Vogl, "Localized creation of yellow single photon emitting carbon complexes in hexagonal boron nitride," *APL Materials*, vol. 11, no. 7, p. 071108, 2023.

[133] A. Kumar, C. Cholsuk, M. N. Mishuk, M. Hazra, C. Pillot, T. Matthes, T. A. Shaik, A. Çakan, V. Deckert, S. Suwanna, and T. Vogl, "Comparative study of quantum emitter fabrication in wide bandgap materials using localized electron irradiation," *ACS Applied Optical Materials*, vol. 2, no. 2, pp. 323–332, 2024.

[134] A. Kumar, C. Samaner, C. Cholsuk, T. Matthes, S. Paçal, Y. Oyun, A. Zand, R. J. Chapman, G. Saerens, R. Grange, S. Suwanna, S. Ateş, and T. Vogl, "Polarization dynamics of solid-state quantum emitters," *ACS Nano*, vol. 18, no. 7, pp. 5270–5281, 2024.

[135] D. Chugh, J. Wong-Leung, L. Li, M. Lysevych, H. H. Tan, and C. Jagadish, "Flow modulation epitaxy of hexagonal boron nitride," *2D Materials*, vol. 5, no. 4, p. 045018, 2018.

[136] C. Li, Z.-Q. Xu, N. Mendelson, M. Kianinia, M. Toth, and I. Aharonovich, "Purification of single-photon emission from hBN using post-processing treatments," *Nanophotonics*, vol. 8, no. 11, pp. 2049–2055, 2019.

[137] Y. Chen, C. Li, S. White, M. Nonahal, Z.-Q. Xu, K. Watanabe, T. Taniguchi, M. Toth, T. T. Tran, and I. Aharonovich, "Generation of high-density quantum emitters in high-quality, exfoliated hexagonal boron nitride," *ACS Applied Materials & Interfaces*, vol. 13, no. 39, pp. 47283–47292, 2021.

[138] H. Ngoc My Duong, M. A. P. Nguyen, M. Kianinia, T. Ohshima, H. Abe, K. Watanabe, T. Taniguchi, J. H. Edgar, I. Aharonovich, and M. Toth, "Effects of high-energy electron irradiation on quantum emitters in hexagonal boron nitride," *ACS Applied Materials & Interfaces*, vol. 10, no. 29, pp. 24886–24891, 2018.

[139] R. Gu, L. Wang, H. Zhu, S. Han, Y. Bai, X. Zhang, B. Li, C. Qin, J. Liu, G. Guo, X. Shan, G. Xiong, J. Gao, C. He, Z. Han, X. Liu, and F. Zhao, "Engineering and microscopic mechanism of quantum emitters induced by heavy ions in hbn," *ACS Photonics*, vol. 8, no. 10, pp. 2912–2922, 2021.

[140] G.-L. Liu, X.-Y. Wu, P.-T. Jing, Z. Cheng, D. Zhan, Y. Bao, J.-X. Yan, H. Xu, L.-G. Zhang, B.-H. Li, K.-W. Liu, L. Liu, and D.-Z. Shen, "Single photon emitters in hexagonal boron nitride fabricated by focused helium ion beam," *Advanced Optical Materials*, p. 2302083, 2023.

[141] X. Xu, Z. O. Martin, D. Sychev, A. S. Lagutchev, Y. P. Chen, T. Taniguchi, K. Watanabe, V. M. Shalaev, and A. Boltasseva, "Creating quantum emitters in hexagonal boron nitride deterministically on chip-compatible substrates," *Nano Letters*, vol. 21, no. 19, pp. 8182–8189, 2021.

[142] A. Gottscholl, M. Kianinia, V. Soltamov, S. Orlinskii, G. Mamin, C. Bradac, C. Kasper, K. Krambrock, A. Sperlich, M. Toth, I. Aharonovich, and V. Dyakonov, "Initialization and read-out of intrinsic spin defects in a van der waals crystal at room temperature," *Nature Materials*, vol. 19, no. 5, pp. 540–545, 2020.

[143] M. Kianinia, S. White, J. E. Fröch, C. Bradac, and I. Aharonovich, "Generation of spin defects in hexagonal boron nitride," *ACS Photonics*, vol. 7, no. 8, pp. 2147–2152, 2020.

[144] X. Gao, B. Jiang, A. E. Llacsahuanga Allcca, K. Shen, M. A. Sadi, A. B. Solanki, P. Ju, Z. Xu, P. Upadhyaya, Y. P. Chen, S. A. Bhave, and T. Li, "High-contrast plasmonic-enhanced shallow spin defects in hexagonal boron nitride for quantum sensing," *Nano Letters*, vol. 21, no. 18, pp. 7708–7714, 2021.

[145] X. Gao, S. Pandey, M. Kianinia, J. Ahn, P. Ju, I. Aharonovich, N. Shivaram, and T. Li, "Femtosecond laser writing of spin defects in hexagonal boron nitride," *ACS Photonics*, vol. 8, no. 4, pp. 994–1000, 2021.

[146] F. F. Murzakhanov, B. V. Yavkin, G. V. Mamin, S. B. Orlinskii, I. E. Mumdzhi, I. N. Gracheva, B. F. Gabbasov, A. N. Smirnov, V. Y. Davydov, and V. A. Soltamov, "Creation of negatively charged boron vacancies in hexagonal boron nitride crystal by electron irradiation and mechanism of inhomogeneous broadening of boron vacancy-related spin resonance lines," *Nanomaterials*, vol. 11, no. 6, 2021.

[147] N. Mendelson, R. Ritika, M. Kianinia, J. Scott, S. Kim, J. E. Fröch, C. Gazzana, M. Westerhausen, L. Xiao, S. S. Mohajerani, S. Strauf, M. Toth, I. Aharonovich, and Z.-Q. Xu, "Coupling spin defects in a layered material to nanoscale plasmonic cavities," *Advanced Materials*, vol. 34, no. 1, p. 2106046, 2022.

[148] C. Qian, V. Villafañe, M. Schalk, G. V. Astakhov, U. Kentsch, M. Helm, P. Soubelet, N. P. Wilson, R. Rizzato, S. Mohr, A. W. Holleitner, D. B. Bucher, A. V. Stier, and J. J. Finley, "Unveiling the zero-phonon line of the boron vacancy center by cavity-enhanced emission," *Nano Letters*, vol. 22, no. 13, pp. 5137–5142, 2022.

[149] M. Huang, J. Zhou, D. Chen, H. Lu, N. J. McLaughlin, S. Li, M. Alghamdi, D. Djugba, J. Shi, H. Wang, and C. R. Du, "Wide field imaging of van der waals ferromagnet Fe_3GeTe_2 by spin defects in hexagonal boron nitride," *Nature Communications*, vol. 13, no. 1, p. 5369, 2022.

[150] A. J. Healey, S. C. Scholten, T. Yang, J. A. Scott, G. J. Abrahams, I. O. Robertson, X. F. Hou, Y. F. Guo, S. Rahman, Y. Lu, M. Kianinia, I. Aharonovich, and J. P. Tetienne, "Quantum microscopy with van der waals heterostructures," *Nature Physics*, vol. 19, no. 1, pp. 87–91, 2023.

[151] B. Whitefield, M. Toth, I. Aharonovich, J.-P. Tetienne, and M. Kianinia, "Magnetic field sensitivity optimization of negatively charged boron vacancy defects in hbn," *Advanced Quantum Technologies*, p. 2300118, 2023.

[152] G. Grosso, H. Moon, B. Lienhard, S. Ali, D. K. Efetov, M. M. Furchi, P. Jarillo-Herrero, M. J. Ford, I. Aharonovich, and D. Englund, "Tunable and high-purity room temperature single-photon emission from atomic defects in hexagonal boron nitride," *Nature Communications*, vol. 8, no. 1, p. 705, 2017.

[153] R. Bourrellier, S. Meuret, A. Tararan, O. Stéphan, M. Kociak, L. H. Tizei, and A. Zobelli, "Bright uv single photon emission at point defects in h-bn," *Nano letters*, vol. 16, no. 7, pp. 4317–4321, 2016.

[154] T. Taniguchi and K. Watanabe, "Synthesis of high-purity boron nitride single crystals under high pressure by using ba–bn solvent," *Journal of Crystal Growth*, vol. 303, no. 2, pp. 525–529, 2007.

[155] M. Onodera, K. Watanabe, M. Isayama, M. Arai, S. Masubuchi, R. Moriya, T. Taniguchi, and T. Machida, "Carbon-rich domain in hexagonal boron nitride: Carrier mobility degradation and anomalous bending of the landau fan diagram in adjacent graphene," *Nano Letters*, vol. 19, no. 10, pp. 7282–7286, 2019.

[156] M. Onodera, M. Isayama, T. Taniguchi, K. Watanabe, S. Masubuchi, R. Moriya, T. Haga, Y. Fujimoto, S. Saito, and T. Machida, "Carbon annealed hpht-hexagonal boron nitride: Exploring defect levels using 2d materials combined through van der waals interface," *Carbon*, vol. 167, pp. 785–791, 2020.

[157] M. Mackoit-Sinkevičienė, M. Maciaszek, C. G. Van de Walle, and A. Alkauskas, "Carbon dimer defect as a source of the 4.1 ev luminescence in hexagonal boron nitride," *Applied Physics Letters*, vol. 115, no. 21, p. 212101, 2019.

[158] C. Jara, T. Rauch, S. Botti, M. A. L. Marques, A. Norambuena, R. Coto, J. E. Castellanos-Águila, J. R. Maze, and F. Munoz, "First-principles identification of single photon emitters based on carbon clusters in hexagonal boron nitride," *The Journal of Physical Chemistry A*, vol. 125, no. 6, pp. 1325–1335, 2021.

[159] S. Li, A. Pershin, G. Thiering, P. Udvarhelyi, and A. Gali, "Ultraviolet quantum emitters in hexagonal boron nitride from carbon clusters," *The Journal of Physical Chemistry Letters*, vol. 13, no. 14, pp. 3150–3157, 2022.

[160] B. Shevitski, S. M. Gilbert, C. T. Chen, C. Kastl, E. S. Barnard, E. Wong, D. F. Ogletree, K. Watanabe, T. Taniguchi, A. Zettl, and S. Aloni, "Blue-light-emitting color centers in high-quality hexagonal boron nitride," *Physical Review B*, vol. 100, no. 15, p. 155419, 2019.

[161] C. Fournier, A. Plaud, S. Roux, A. Pierret, M. Rosticher, K. Watanabe, T. Taniguchi, S. Buil, X. Quélin, J. Barjon, J.-P. Hermier, and A. Delteil, "Position-controlled quantum emitters with reproducible emission wavelength in hexagonal boron nitride," *Nature Communications*, vol. 12, no. 1, p. 3779, 2021.

[162] N. Mendelson, Z.-Q. Xu, T. T. Tran, M. Kianinia, J. Scott, C. Bradac, I. Aharonovich, and M. Toth, "Engineering and tuning of quantum emitters in few-layer hexagonal boron nitride," *ACS Nano*, vol. 13, no. 3, pp. 3132–3140, 2019.

[163] M. T. Westerhausen, A. T. Trycz, C. Stewart, M. Nonahal, B. Regan, M. Kianinia, and I. Aharonovich, "Controlled doping of gev and snv color centers in diamond using chemical vapor deposition," *ACS Applied Materials & Interfaces*, vol. 12, no. 26, pp. 29700–29705, 2020.

[164] Y. Zhou, Z. Mu, G. Adamo, S. Bauerdick, A. Rudzinski, I. Aharonovich, and W.-b. Gao, "Direct writing of single germanium vacancy center arrays in diamond," *New Journal of Physics*, vol. 20, no. 12, p. 125004, 2018.

[165] K. Barthelmi, J. Klein, A. Hötger, L. Sigl, F. Sigger, E. Mitterreiter, S. Rey, S. Gyger, M. Lorke, M. Florian, F. Jahnke, T. Taniguchi, K. Watanabe, V. Zwiller, K. D. Jöns, U. Wurstbauer, C. Kastl, A. Weber-Bargioni, J. J. Finley, K. Müller, and A. W. Holleitner, "Atomistic defects as single-photon emitters in atomically thin MoS_2," *Applied Physics Letters*, vol. 117, no. 7, p. 070501, 2020.

[166] E. Losero, V. Goblot, Y. Zhu, H. Babashah, V. Boureau, F. Burkart, and C. Galland, "Creation of nv centers in diamond under 155 mev electron irradiation," *arXiv 2305.15009*, 2023.

[167] L. Gan, D. Zhang, R. Zhang, Q. Zhang, H. Sun, Y. Li, and C.-Z. Ning, "Large-scale, high-yield laser fabrication of bright and pure single-photon emitters at room temperature in hexagonal boron nitride," *ACS Nano*, vol. 16, no. 9, pp. 14254–14261, 2022.

[168] Z.-Q. Xu, C. Elbadawi, T. T. Tran, M. Kianinia, X. Li, D. Liu, T. B. Hoffman, M. Nguyen, S. Kim, J. H. Edgar, X. Wu, L. Song, S. Ali, M. Ford, M. Toth, and I. Aharonovich, "Single photon emission from plasma treated 2d hexagonal boron nitride," *Nanoscale*, vol. 10, no. 17, pp. 7957–7965, 2018.

[169] S. Choi, B. C. Johnson, S. Castelletto, C. Ton-That, M. R. Phillips, and I. Aharonovich, "Single photon emission from zno nanoparticles," *Applied Physics Letters*, vol. 104, no. 26, p. 261101, 2014.

[170] D. B. Hovis and A. H. Heuer, "The use of laser scanning confocal microscopy (lscm) in materials science," *Journal of Microscopy*, vol. 240, no. 3, pp. 173–180, 2010.

[171] J. Pawley, *Handbook of biological confocal microscopy*, vol. 236. Springer Science & Business Media, 2006.

[172] D. Wigger, R. Schmidt, O. Del Pozo-Zamudio, J. A. Preuß, P. Tonndorf, R. Schneider, P. Steeger, J. Kern, Y. Khodaei, J. Sperling, S. M. de Vasconcellos, R. Bratschitsch, and T. Kuhn, "Phonon-assisted emission and absorption of individual color centers in hexagonal boron nitride," *2D Materials*, vol. 6, no. 3, p. 035006, 2019.

[173] F. Jelezko and J. Wrachtrup, "Single defect centres in diamond: A review," *physica status solidi (a)*, vol. 203, no. 13, pp. 3207–3225, 2006.

[174] Y.-F. Gao, J.-M. Lai, Y.-J. Sun, X.-L. Liu, C.-N. Lin, P.-H. Tan, C.-X. Shan, and J. Zhang, "Charge state manipulation of nv centers in diamond under phonon-assisted anti-stokes excitation of nv0," *ACS Photonics*, vol. 9, no. 5, pp. 1605–1613, 2022.

[175] J. Zhang, D. Li, R. Chen, and Q. Xiong, "Laser cooling of a semiconductor by 40 kelvin," *Nature*, vol. 493, no. 7433, pp. 504–508, 2013.

[176] T. T. Tran, C. Bradac, A. S. Solntsev, M. Toth, and I. Aharonovich, "Suppression of spectral diffusion by anti-stokes excitation of quantum emitters in hexagonal boron nitride," *Applied Physics Letters*, vol. 115, no. 7, p. 071102, 2019.

[177] R. H. Brown, R. Q. Twiss, A. C. B. Lovell, and g. surName, "Interferometry of the intensity fluctuations in light - i. basic theory: the correlation between photons in coherent beams of radiation," *Proceedings of the Royal Society of London. Series A. Mathematical and Physical Sciences*, vol. 242, no. 1230, pp. 300–324, 1957.

[178] A. Gruber, A. Dräbenstedt, C. Tietz, L. Fleury, J. Wrachtrup, and C. v. Borczyskowski, "Scanning confocal optical microscopy and magnetic resonance on single defect centers," *Science*, vol. 276, no. 5321, pp. 2012–2014, 1997.

[179] M. A. S. Kalceff and M. R. Phillips, "Cathodoluminescence microcharacterization of the defect structure of quartz," *Physical Review B*, vol. 52, no. 5, pp. 3122–3134, 1995.

[180] P. Jaffrennou, J. Barjon, J. S. Lauret, B. Attal-Trétout, F. Ducastelle, and A. Loiseau, "Origin of the excitonic recombinations in hexagonal boron nitride by spatially resolved cathodoluminescence spectroscopy," *Journal of Applied Physics*, vol. 102, no. 11, p. 116102, 2007.

[181] N. Yamamoto, H. Itoh, V. Grillo, S. Chichibu, S. Keller, J. Speck, S. DenBaars, U. Mishra, S. Nakamura, and G. Salviati, "Cathodoluminescence characterization of dislocations in gallium nitride using a transmission electron microscope," *Journal of applied physics*, vol. 94, no. 7, pp. 4315–4319, 2003.

[182] S. Zu, T. Han, M. Jiang, F. Lin, X. Zhu, and Z. Fang, "Deep-subwavelength resolving and manipulating of hidden chirality in achiral nanostructures," *ACS Nano*, vol. 12, no. 4, pp. 3908–3916, 2018.

[183] T. Coenen and N. M. Haegel, "Cathodoluminescence for the 21st century: Learning more from light," *Applied Physics Reviews*, vol. 4, no. 3, p. 031103, 2017.

[184] M. Kociak and L. F. Zagonel, "Cathodoluminescence in the scanning transmission electron microscope," *Ultramicroscopy*, vol. 176, pp. 112–131, 2017.

[185] J. Götze, H.-P. Schertl, R. D. Neuser, U. Kempe, and J. M. Hanchar, "Optical microscope-cathodoluminescence (om–cl) imaging as a powerful tool to reveal internal textures of minerals," *Mineralogy and Petrology*, vol. 107, no. 3, pp. 373–392, 2013.

[186] Y. V. Petrov, O. F. Vyvenko, O. A. Gogina, K. Bolotin, S. Kovalchuk, K. Watanabe, and T. Taniguchi, "Cathodoluminescence of carbon-related defects in hexagonal boron nitride," *Journal of Physics: Conference Series*, vol. 2103, no. 1, p. 012065, 2021.

[187] D. Curie, J. T. Krogel, L. Cavar, A. Solanki, P. Upadhyaya, T. Li, Y.-Y. Pai, M. Chilcote, V. Iyer, A. Puretzky, I. Ivanov, M.-H. Du, F. Reboredo, and B. Lawrie, "Correlative nanoscale imaging of strained hbn spin defects," *ACS Applied Materials & Interfaces*, vol. 14, no. 36, pp. 41361–41368, 2022.

[188] S. Fiedler, S. Morozov, D. Komisar, E. A. Ekimov, L. F. Kulikova, V. A. Davydov, V. N. Agafonov, S. Kumar, C. Wolff, S. I. Bozhevolnyi, and N. A. Mortensen, "Sub-to-super-poissonian photon statistics in cathodoluminescence of color center ensembles in isolated diamond crystals," *Nanophotonics*, vol. 12, no. 12, pp. 2231–2237, 2023.

[189] S. Meuret, L. H. G. Tizei, T. Cazimajou, R. Bourrellier, H. C. Chang, F. Treussart, and M. Kociak, "Photon bunching in cathodoluminescence," *Physical Review Letters*, vol. 114, no. 19, p. 197401, 2015.

[190] M. A. Feldman, E. F. Dumitrescu, D. Bridges, M. F. Chisholm, R. B. Davidson, P. G. Evans, J. A. Hachtel, A. Hu, R. C. Pooser, R. F. Haglund, and B. J. Lawrie, "Colossal photon bunching in quasiparticle-mediated nanodiamond cathodoluminescence," *Physical Review B*, vol. 97, no. 8, p. 081404, 2018.

[191] S. Yanagimoto, N. Yamamoto, T. Sannomiya, and K. Akiba, "Purcell effect of nitrogen-vacancy centers in nanodiamond coupled to propagating and localized surface plasmons revealed by photon-correlation cathodoluminescence," *Physical Review B*, vol. 103, no. 20, p. 205418, 2021.

[192] K. Tsukamoto, T. Kuroi, and Y. Kawasaki, "Evolution of ion implantation technology and its contribution to semiconductor industry," *AIP Conference Proceedings*, vol. 1321, no. 1, pp. 9–16, 2011.

[193] M. Atatüre, D. Englund, N. Vamivakas, S.-Y. Lee, and J. Wrachtrup, "Material platforms for spin-based photonic quantum technologies," *Nature Reviews Materials*, vol. 3, no. 5, pp. 38–51, 2018.

[194] M. M. M. Bilek, "Biofunctionalization of surfaces by energetic ion implantation: Review of progress on applications in implantable biomedical devices and antibody microarrays," *Applied Surface Science*, vol. 310, pp. 3–10, 2014.

[195] D. Scarabelli, M. Trusheim, O. Gaathon, D. Englund, and S. J. Wind, "Nanoscale engineering of closely-spaced electronic spins in diamond," *Nano Letters*, vol. 16, no. 8, pp. 4982–4990, 2016.

[196] T. Schröder, M. E. Trusheim, M. Walsh, L. Li, J. Zheng, M. Schukraft, A. Sipahigil, R. E. Evans, D. D. Sukachev, C. T. Nguyen, J. L. Pacheco, R. M. Camacho, E. S. Bielejec, M. D. Lukin, and D. Englund, "Scalable focused ion beam creation of nearly lifetime-limited single quantum emitters in diamond nanostructures," *Nature Communications*, vol. 8, no. 1, p. 15376, 2017.

[197] J. Wang, Y. Zhou, X. Zhang, F. Liu, Y. Li, K. Li, Z. Liu, G. Wang, and W. Gao, "Efficient generation of an array of single silicon-vacancy defects in silicon carbide," *Physical Review Applied*, vol. 7, no. 6, p. 064021, 2017.

[198] K. Groot-Berning, T. Kornher, G. Jacob, F. Stopp, S. T. Dawkins, R. Kolesov, J. Wrachtrup, K. Singer, and F. Schmidt-Kaler, "Deterministic single-ion implantation of rare-earth ions for nanometer-resolution color-center generation," *Physical Review Letters*, vol. 123, no. 10, p. 106802, 2019.

[199] K. Groot-Berning, G. Jacob, C. Osterkamp, F. Jelezko, and F. Schmidt-Kaler, "Fabrication of 15nv− centers in diamond using a deterministic single ion implanter," *New Journal of Physics*, vol. 23, no. 6, p. 063067, 2021.

[200] S. Pezzagna, D. Wildanger, P. Mazarov, A. D. Wieck, Y. Sarov, I. Rangelow, B. Naydenov, F. Jelezko, S. W. Hell, and J. Meijer, "Nanoscale engineering and optical addressing of single spins in diamond," *Small*, vol. 6, no. 19, pp. 2117–2121, 2010.

[201] T. Jung, J. Görlitz, B. Kambs, C. Pauly, N. Raatz, R. Nelz, E. Neu, A. M. Edmonds, M. Markham, F. Mücklich, J. Meijer, and C. Becher, "Spin measurements of nv centers coupled to a photonic crystal cavity," *APL Photonics*, vol. 4, no. 12, p. 120803, 2019.

[202] R. S. Nelson, "The theory of recoil implantation," *Radiation Effects*, vol. 2, no. 1, pp. 47–50, 1969.

[203] W. Möller and W. Eckstein, "Ion mixing and recoil implantation simulations by means of tridyn," *Nuclear Instruments and Methods in Physics Research Section B: Beam Interactions with Materials and Atoms*, vol. 7-8, pp. 645–649, 1985.

[204] P. Sigmund, "Recoil implantation and ion-beam-induced composition changes in alloys and compounds," *Journal of Applied Physics*, vol. 50, no. 11, pp. 7261–7263, 1979.

[205] M. W. Doherty, N. B. Manson, P. Delaney, F. Jelezko, J. Wrachtrup, and L. C. L. Hollenberg, "The nitrogen-vacancy colour centre in diamond," *Physics Reports*, vol. 528, no. 1, pp. 1–45, 2013.

[206] K. Wittmaack and P. Blank, *The influence of recoil implantation of absorbed oxygen on the entrapment of xenon in aluminum and silicon*, pp. 363–374. Springer, 1977.

[207] M. Toth, C. Lobo, V. Friedli, A. Szkudlarek, and I. Utke, "Continuum models of focused electron beam induced processing," *Beilstein Journal of Nanotechnology*, vol. 6, pp. 1518–1540, 2015.

[208] J. D. Fowlkes and P. D. Rack, "Fundamental electron-precursor-solid interactions derived from time-dependent electron-beam-induced deposition simulations and experiments," *ACS Nano*, vol. 4, no. 3, pp. 1619–1629, 2010.

[209] W. F. van Dorp, T. W. Hansen, J. B. Wagner, and J. T. M. De Hosson, "The role of electron-stimulated desorption in focused electron beam induced deposition," *Beilstein Journal of Nanotechnology*, vol. 4, pp. 474–480, 2013.

[210] R. Winkler, J. Fowlkes, A. Szkudlarek, I. Utke, P. D. Rack, and H. Plank, "The nanoscale implications of a molecular gas beam during electron beam induced deposition," *ACS Applied Materials & Interfaces*, vol. 6, no. 4, pp. 2987–2995, 2014.

[211] J. Schwartz, P. Michaelides, C. D. Weis, and T. Schenkel, "In situ optimization of co-implantation and substrate temperature conditions for nitrogen-vacancy center formation in single-crystal diamonds," *New Journal of Physics*, vol. 13, no. 3, p. 035022, 2011.

[212] J. Bishop, M. Fronzi, C. Elbadawi, V. Nikam, J. Pritchard, J. E. Fröch, N. M. H. Duong, M. J. Ford, I. Aharonovich, C. J. Lobo, and M. Toth, "Deterministic nanopatterning of diamond using electron beams," *ACS Nano*, vol. 12, no. 3, pp. 2873–2882, 2018.

[213] C. J. Lobo, A. Martin, M. R. Phillips, and M. Toth, "Electron beam induced chemical dry etching and imaging in gaseous NH_3 environments," *Nanotechnology*, vol. 23, no. 37, p. 375302, 2012.

[214] A. Stacey, T. J. Karle, L. P. McGuinness, B. C. Gibson, K. Ganesan, S. Tomljenovic-Hanic, A. D. Greentree, A. Hoffman, R. G. Beausoleil, and S. Prawer, "Depletion of nitrogen-vacancy color centers in diamond via hydrogen passivation," *Applied Physics Letters*, vol. 100, no. 7, p. 071902, 2012.

[215] J. Engels, J. Weippert, T. Luo, J. Kustermann, P. Quellmalz, N. Mathes, L. Lindner, C. Giese, L. Kirste, P. Knittel, J. Jeske, and V. Lebedev, "High odmr contrast and alignment of nv centers in microstructures grown on heteroepitaxial diamonds," *Applied Physics Letters*, vol. 124, no. 16, p. 164001, 2024.

[216] J. Comtet, E. Glushkov, V. Navikas, J. Feng, V. Babenko, S. Hofmann, K. Watanabe, T. Taniguchi, and A. Radenovic, "Wide-field spectral super-resolution mapping of optically active defects in hexagonal boron nitride," *Nano Letters*, vol. 19, no. 4, pp. 2516–2523, 2019.

[217] J. C. Stewart, Y. Fan, J. S. H. Danial, A. Goetz, A. S. Prasad, O. J. Burton, J. A. Alexander-Webber, S. F. Lee, S. M. Skoff, V. Babenko, and S. Hofmann, "Quantum emitter localization in layer-engineered hexagonal boron nitride," *ACS Nano*, vol. 15, no. 8, pp. 13591–13603, 2021.

[218] J. Ziegler, R. Klaiss, A. Blaikie, D. Miller, V. R. Horowitz, and B. J. Alemán, "Deterministic quantum emitter formation in hexagonal boron nitride via controlled edge creation," *Nano Letters*, vol. 19, no. 3, pp. 2121–2127, 2019.

[219] H. Liu, C. Y. You, J. Li, P. R. Galligan, J. You, Z. Liu, Y. Cai, and Z. Luo, "Synthesis of hexagonal boron nitrides by chemical vapor deposition and their use as single photon emitters," *Nano Materials Science*, vol. 3, no. 3, pp. 291–312, 2021.

[220] V. Ivady, G. Barcza, G. Thiering, S. Li, H. Hamdi, J.-P. Chou, O. Legeza, and A. Gali, "Ab initio theory of the negatively charged boron vacancy qubit in hexagonal boron nitride," *npj Computational Materials*, vol. 6, no. 1, p. 41, 2020.

[221] P. Auburger and A. Gali, "Towards ab initio identification of paramagnetic substitutional carbon defects in hexagonal boron nitride acting as quantum bits," *Physical Review B*, vol. 104, no. 7, p. 075410, 2021.

[222] M. Winter, M. H. E. Bousquet, D. Jacquemin, I. Duchemin, and X. Blase, "Photoluminescent properties of the carbon-dimer defect in hexagonal boron-nitride: A many-body finite-size cluster approach," *Physical Review Materials*, vol. 5, no. 9, p. 095201, 2021.

[223] L. Museur, E. Feldbach, and A. Kanaev, "Defect-related photoluminescence of hexagonal boron nitride," *Physical Review B*, vol. 78, no. 15, p. 155204, 2008.

[224] K. Era, F. Minami, and T. Kuzuba, "Fast luminescence from carbon-related defects of hexagonal boron nitride," *Journal of Luminescence*, vol. 24-25, pp. 71–74, 1981.

[225] T. Pelini, C. Elias, R. Page, L. Xue, S. Liu, J. Li, J. H. Edgar, A. Dréau, V. Jacques, P. Valvin, B. Gil, and G. Cassabois, "Shallow and deep levels in carbon-doped hexagonal boron nitride crystals," *Physical Review Materials*, vol. 3, no. 9, p. 094001, 2019.

[226] M. A. Feldman, C. E. Marvinney, A. A. Puretzky, and B. J. Lawrie, "Evidence of photochromism in a hexagonal boron nitride single-photon emitter," *Optica*, vol. 8, no. 1, pp. 1–5, 2021.

[227] G. Grosso, H. Moon, C. J. Ciccarino, J. Flick, N. Mendelson, L. Mennel, M. Toth, I. Aharonovich, P. Narang, and D. R. Englund, "Low-temperature electron–phonon interaction of quantum emitters in hexagonal boron nitride," *ACS Photonics*, vol. 7, no. 6, pp. 1410–1417, 2020.

[228] S. White, C. Stewart, A. S. Solntsev, C. Li, M. Toth, M. Kianinia, and I. Aharonovich, "Phonon dephasing and spectral diffusion of quantum emitters in hexagonal boron nitride," *Optica*, vol. 8, no. 9, pp. 1153–1158, 2021.

[229] M. Hoese, P. Reddy, A. Dietrich, M. K. Koch, K. G. Fehler, M. W. Doherty, and A. Kubanek, "Mechanical decoupling of quantum emitters in hexagonal boron nitride from low-energy phonon modes," *Science Advances*, vol. 6, no. 40, p. eaba6038, 2020.

[230] N. R. Jungwirth and G. D. Fuchs, "Optical absorption and emission mechanisms of single defects in hexagonal boron nitride," *Physical Review Letters*, vol. 119, no. 5, p. 057401, 2017.

[231] A. Polman, M. Kociak, and F. J. García de Abajo, "Electron-beam spectroscopy for nanophotonics," *Nature Materials*, vol. 18, no. 11, pp. 1158–1171, 2019.

[232] B. G. Yacobi and D. B. Holt, *Cathodoluminescence Microscopy of Inorganic Solids*. Springer, 1991.

[233] Y. Kubota, K. Watanabe, O. Tsuda, and T. Taniguchi, "Deep ultraviolet light-emitting hexagonal boron nitride synthesized at atmospheric pressure," *Science*, vol. 317, no. 5840, pp. 932–934, 2007.

[234] J. S. Kim, K. B. Borisenko, V. Nicolosi, and A. I. Kirkland, "Controlled radiation damage and edge structures in boron nitride membranes," *ACS Nano*, vol. 5, no. 5, pp. 3977–3986, 2011.

[235] T. W. Shanley, A. A. Martin, I. Aharonovich, and M. Toth, "Localized chemical switching of the charge state of nitrogen-vacancy luminescence centers in diamond," *Applied Physics Letters*, vol. 105, no. 6, p. 063103, 2014.

[236] C. T. Nguyen, D. D. Sukachev, M. K. Bhaskar, B. Machielse, D. S. Levonian, E. N. Knall, P. Stroganov, R. Riedinger, H. Park, M. Lončar, and M. D. Lukin, "Quantum network nodes based on diamond qubits with an efficient nanophotonic interface," *Physical Review Letters*, vol. 123, p. 183602, 2019.

[237] M. Pompili, S. L. N. Hermans, S. Baier, H. K. C. Beukers, P. C. Humphreys, R. N. Schouten, R. F. L. Vermeulen, M. J. Tiggelman, L. dos Santos Martins, B. Dirkse, S. Wehner, and R. Hanson, "Realization of a multinode quantum network of remote solid-state qubits," *Science*, vol. 372, no. 6539, pp. 259–264, 2021.

[238] C. Bradac, W. Gao, J. Forneris, M. E. Trusheim, and I. Aharonovich, "Quantum nanophotonics with group IV defects in diamond," *Nature Communications*, vol. 10, p. 5625, 2019.

[239] N. Chejanovsky, A. Mukherjee, J. Geng, Y.-C. Chen, Y. Kim, A. Denisenko, A. Finkler, T. Taniguchi, K. Watanabe, D. B. R. Dasari, P. Auburger, A. Gali, J. H. Smet, and J. Wrachtrup, "Single-spin resonance in a van der waals embedded paramagnetic defect," *Nature Materials*, vol. 20, no. 8, p. 1079, 2021.

[240] A. Ramsay, R. Hekmati, C. Patrickson, S. Baber, D. Arvidsson-Shukur, A. Bennett, and I. Luxmoore, "Coherence protection of spin qubits in hexagonal boron nitride," *Nature Communications*, vol. 14, no. 1, p. 461, 2023.

[241] X. Gao, S. Vaidya, K. Li, P. Ju, B. Jiang, Z. Xu, A. Allcca, K. Shen, T. Taniguchi, K. Watanabe, S. Bhave, Y. Chen, Y. Ping, and T. Li, "Nuclear spin polarization and control in hexagonal boron nitride," *Nature Materials*, vol. 21, no. 9, p. 1024, 2022.

[242] A. Wood, A. Lozovoi, Z.-H. Zhang, S. Sharma, G. I. López-Morales, H. Jayakumar, N. P. de Leon, and C. A. Meriles, "Room-temperature photochromism of silicon vacancy centers in CVD diamond," *Nano Letters*, vol. 23, no. 3, pp. 1017–1022, 2023.

[243] M. Berthel, O. Mollet, G. Dantelle, T. Gacoin, S. Huant, and A. Drezet, "Photophysics of single nitrogen-vacancy centers in diamond nanocrystals," *Physical Review B*, vol. 91, p. 035308, 2015.

[244] L. Weston, D. Wickramaratne, M. Mackoit, A. Alkauskas, and C. G. Van de Walle, "Native point defects and impurities in hexagonal boron nitride," *Physical Review B*, vol. 97, no. 21, p. 214104, 2018.

[245] M. V. Hauf, B. Grotz, B. Naydenov, M. Dankerl, S. Pezzagna, J. Meijer, F. Jelezko, J. Wrachtrup, M. Stutzmann, F. Reinhard, and J. A. Garrido, "Chemical control of the charge state of nitrogen-vacancy centers in diamond," *Physical Review B*, vol. 83, p. 081304, 2011.

[246] X.-D. Chen, C.-L. Zou, F.-W. Sun, and G.-C. Guo, "Optical manipulation of the charge state of nitrogen-vacancy center in diamond," *Applied Physics Letters*, vol. 103, no. 1, 2013.

[247] Y. Doi, T. Makino, H. Kato, D. Takeuchi, M. Ogura, H. Okushi, H. Morishita, T. Tashima, S. Miwa, S. Yamasaki, P. Neumann, J. Wrachtrup, Y. Suzuki, and N. Mizuochi, "Deterministic electrical charge-state initialization of single nitrogen-vacancy center in diamond," *Physical Review X*, vol. 4, no. 1, p. 011057, 2014.

[248] N. Liv, A. C. Zonnevylle, A. C. Narvaez, A. P. J. Effting, P. W. Voorneveld, M. S. Lucas, J. C. Hardwick, R. A. Wepf, P. Kruit, and J. P. Hoogenboom, "Simultaneous correlative scanning electron and high-na fluorescence microscopy," *PLOS ONE*, vol. 8, no. 2, p. e55707, 2013.

[249] A. C. Zonnevylle, R. F. C. Van Tol, N. Liv, A. C. Narvaez, A. P. J. Effting, P. Kruit, and J. P. Hoogenboom, "Integration of a high-na light microscope in a scanning electron microscope," *Journal of Microscopy*, vol. 252, no. 1, pp. 58–70, 2013.

[250] D. Drouin, A. R. Couture, D. Joly, X. Tastet, V. Aimez, and R. Gauvin, "CASINO V2.42-A fast and easy-to-use modeling tool for scanning electron microscopy and microanalysis users," *Scanning*, vol. 29, no. 3, pp. 92–101, 2007.

[251] J. Cazaux, "Mechanisms of charging in electron spectroscopy," *Journal of Electron Spectroscopy and Related Phenomena*, vol. 105, no. 2, pp. 155–185, 1999.

[252] H. Kawano, "Effective work functions of the elements: Database, most probable value, previously recommended value, polycrystalline thermionic contrast, change at critical temperature, anisotropic dependence sequence, particle size dependence," *Progress in Surface Science*, vol. 97, no. 1, p. 100583, 2022.

[253] T. E. Everhart and P. H. Hoff, "Determination of kilovolt electron energy dissipation vs penetration distance in solid materials," *Journal of Applied Physics*, vol. 42, no. 13, pp. 5837–5846, 1971.

[254] R. C. Alig and S. Bloom, "Electron-hole-pair creation energies in semiconductors," *Physical Review Letters*, vol. 35, no. 22, pp. 1522–1525, 1975.

[255] H.-J. Fitting, M. Touzin, and E. Schreiber, "Fast electron beam charge injection and switching in dielectrics," *physica status solidi c*, vol. 8, no. 4, pp. 1282–1286, 2011.

[256] M. Stobbe, A. Könies, R. Redmer, J. Henk, and W. Schattke, "Interband transition rate in GaAs," *Physical Review B*, vol. 44, no. 20, pp. 11105–11110, 1991.

[257] M. Toth, C. Zachreson, and I. Aharonovich, "Role of recombination pathway competition in spatially resolved cathodoluminescence spectroscopy," *Applied Physics Letters*, vol. 105, no. 24, 2014.

[258] Y. Han, C. Pederson, B. E. Matthews, N. S. Yama, M. F. Parsons, and K.-M. C. Fu, "Creation of color centers in diamond by recoil implantation through dielectric films," *Applied Physics Letters*, vol. 124, no. 4, p. 044007, 2024.

[259] C. Fournier, S. Roux, K. Watanabe, T. Taniguchi, S. Buil, J. Barjon, J.-P. Hermier, and A. Delteil, "Two-photon interference from a quantum emitter in hexagonal boron nitride," *Physical Review Applied*, vol. 19, no. 4, p. L041003, 2023.

[260] S. Kim, J. E. Fröch, J. Christian, M. Straw, J. Bishop, D. Totonjian, K. Watanabe, T. Taniguchi, M. Toth, and I. Aharonovich, "Photonic crystal cavities from hexagonal boron nitride," *Nature Communications*, vol. 9, no. 1, p. 2623, 2018.

[261] J. E. Fröch, S. Kim, N. Mendelson, M. Kianinia, M. Toth, and I. Aharonovich, "Coupling hexagonal boron nitride quantum emitters to photonic crystal cavities," *ACS Nano*, vol. 14, no. 6, pp. 7085–7091, 2020.

[262] J. E. Fröch, C. Li, Y. Chen, M. Toth, M. Kianinia, S. Kim, and I. Aharonovich, "Purcell enhancement of a cavity-coupled emitter in hexagonal boron nitride," *Small*, vol. 18, no. 2, p. 2104805, 2022.

[263] T. Vogl, R. Lecamwasam, B. C. Buchler, Y. Lu, and P. K. Lam, "Compact cavity-enhanced single-photon generation with hexagonal boron nitride," *ACS Photonics*, vol. 6, no. 8, pp. 1955–1962, 2019. doi: 10.1021/acsphotonics.9b00314.

[264] S. Häußler, G. Bayer, R. Waltrich, N. Mendelson, C. Li, D. Hunger, I. Aharonovich, and A. Kubanek, "Tunable fiber-cavity enhanced photon emission from defect centers in hbn," *Advanced Optical Materials*, vol. 9, no. 17, p. 2002218, 2021.

[265] A. Pierret, J. Loayza, B. Berini, A. Betz, B. Plaçais, F. Ducastelle, J. Barjon, and A. Loiseau, "Excitonic recombinations in hBN: From bulk to exfoliated layers," *Physical Review B*, vol. 89, no. 3, p. 035414, 2014.

[266] K. F. Mak, C. Lee, J. Hone, J. Shan, and T. F. Heinz, "Atomically thin MoS_2: A new direct-gap semiconductor," *Physical Review Letters*, vol. 105, no. 13, p. 136805, 2010.